University of Alberta

Damage Detection in Tires From Strain Values Calculated Using Digital Image Correlation

by

Amanda Kotchon

A thesis submitted to the Faculty of Graduate Studies and Research
in partial fulfillment of the requirements for the degree of

Master of Science

Mechanical Engineering

Spring 2013
Edmonton, Alberta

Abstract

Tire failure in mining operations can hazardous, resulting in financial and productivity losses. There are opportunities to improve tire monitoring systems by safely and remotely providing full-field measurements of tire properties. An optical fault detection system has been developed to investigate the feasibility of using digital image correlation to measure displacement and strain on a tire surface with the aim of detecting tire damage. This study defines metrics for damage visibility and examines the visibility of different damage types at multiple orientations, under various loading conditions in a laboratory setting. Internal and external damage was successfully detected from changes in surface strain. Knowledge gained from this investigation can be used to drive the future development of industrial tire monitoring solutions.

Acknowledgements

I am grateful to my instructors and supervisors for their guidance, my coworkers for their support, and the machine shop and support staff for everything else.

Abstract

Acknowledgements

Chapter 1: Introduction.....1

1.1 Background and Motivation 1

1.2 Fault Classification..... 3

1.3 Project Definition 6

1.4 Objectives..... 7

1.5 Organization..... 7

Chapter 2: Literature Review 8

2.1 Tire Failure..... 8

2.1.1 Theoretical 8

2.1.2 Experimental Studies 9

2.2 Inspection of Tires and Composite Rubber Materials 10

2.2.1 Optical Tire Inspection Techniques..... 10

2.2.2 Haulage Tire Inspection 12

2.2.3 Other Monitoring Techniques 13

2.2.4 Concluding Remarks..... 13

Chapter 3: Theory 14

3.1 Digital Image Correlation..... 14

3.1.1 Application to Mechanics and Tire Inspection 14

3.1.2 Correlation Theory..... 15

3.1.3 Calibration Theory 18

3.1.4 Two-Component, 2D Measurements 18

3.1.5 Three-Component, 3D Measurements 18
3.2 Tire Mechanics 19
3.2.1 Tire Deformation 19
3.2.2 Load Distribution 21
Chapter 4: Design and Commissioning of Experiment and Methodology 22
4.1 Design of Experiment 22
4.1.1 System Requirements 23
4.1.2 Variables of Interest 24
4.2 Equipment 25
4.2.1 Tire Testing Apparatus 26
4.2.2 Cameras 28
4.2.2.1 Lenses and Accessories 28
4.2.2.2 Calibration Target and Procedure 29
4.2.3 Tires 32
4.2.3.1 Selection of Tire Properties 32
4.2.3.2 Tire Deformation 32
4.2.3.3 Tire Geometry 34
4.2.3.4 Tire Construction 35
4.2.3.5 Tire Surface Pattern 35
4.2.4 Justification of Software Selection for Experiment 36
4.3 Preliminary Work 37
4.3.1 General Procedure 38
4.3.2 Displacement of Radial Sidewall Cut 39
4.3.3 Displacement of Tangential Cut 41

4.3.4 Improvements to System and Procedure 42

Chapter 5: Visibility of Tire Damage : Results 45

5.1 Stationary Loading of Sidewall Cuts 45

5.1.1 Creating Artificial Tire Damage 46

5.1.2 Procedure: Loading and Processing 47

5.1.3 External Cut Under Stationary Loading 48

5.1.3.1 Displacement and Strain Surrounding External Cut 48

5.1.4 Internal Damage Under Stationary Loading 52

5.1.4.1 Area of Interest 52

5.1.4.2 Displacement and Strain Surrounding Internal Damage 53

5.2 Area of Damage Visibility 58

5.2.1 Maximum and Minimum Principal Strains 58

5.2.2 Defining Damage Visibility 61

5.2.3 Procedure: Orienting Damage, Controlling Displacement, and 3D Processing 64

5.2.4 Strain in Damaged Regions by Orientation 65

5.2.4.1 Strain at External Damage by Orientation 65

5.2.4.2 Strain at Internal Cut by Orientation 67

5.2.4.3 Comparison to Undamaged Regions 69

5.2.5 Repeatability of Results 70

5.2.5.1 Multiple Loadings of Test Tire #1 71

5.2.5.2 Visibility of External Damage in Test Tire #2 72

5.2.6 Discussion and Applications 74

5.3 Damage Visibility from Rotating Trials 75

5.3.1 Preprocessing: Rotating and Aligning Tire Images 75

5.3.2 Anticipated Effects 78
5.3.3 Procedure: Preprocessing & Tire Rotation 79
5.3.4 Visibility of Damage by Orientation from Rotating Tests 80
5.3.5 Discussion and Applications 84
Chapter 6: Conclusions and Future Work 86
6.1 Conclusions 86
6.2 Future Work and Industrial Applications 88
6.2.1 Laboratory 89
6.2.2.1 Experimental Studies and FE 89
6.2.1.2 Damage Type and Severity 90
6.2.1.3 Pattern 90
6.2.2 Industrial Applications 90
6.2.2.1 Operations and Observations 91
6.2.2.2 System Description 93
6.2.2.3 Practical Considerations 93
6.2.2.4 Temperature and Pressure Monitoring 94
6.3 Summary 95
References 97
Appendix A: Load Cell Calibration 102
Appendix B: Tire Deformation 103
Appendix C: Uncertainty in Strain Values 105

List of Tables

Table 1: End Mill Specifications 23

Table 2: Variables of Interest 25

Table 3: Comparison of Camera Specifications 28

Table 4: Visibility of External Cut at Multiple Orientations Relative to Load 66

Table 5: Visibility of Internal Cut at Various Positions Relative to Loading 68

Table 6: Strain in Control Region at Various Orientations Relative to Load 70

Table 7: Repeatability of Tire Visibility Results at a Specific Orientation 71

Table 8: Visibility of External Damage to Tire #2 By Orientation 72

Table 9: Design Considerations for Optical Inspection System 94

List of Figures

Figure 1: Maintenance Personnel and Ultra-Class Haulage Tire 2

Figure 2: Percentage of Reported Haulage Tire Failures By Type (Data: Anzabi 2012) 3

Figure 3: Haulage TIre with Tread Cut and Separation 4

Figure 4: Sidewall Cut In Haulage Tire 4

Figure 5: Internal View of Belt Separation in Haulage Tire 5

Figure 6: Displacement Vector Calculation On Tire Surface 16

Figure 7: Tire Geometry Under Load 20

Figure 8: Tire Testing Apparatus, Camera, Tire 26

Figure 9: Overhead View of Camera Installation 27

Figure 10: Correction of Focal Planes Using Scheimpflug Adapter 29

Figure 11: Uncorrected Image of Camera Calibration Target 30

Figure 12: Uncorrected (A) and Rectified (B) Calibration Image 30

Figure 13: Sample Image of Haulage Tire at Surface Mining Operation 33

Figure 14: Geometric Comparison of 42 cm Laboratory Tire (A) to Industrial Haulage Tire (B) .. 34

Figure 15: High-Contrast, Randomized Speckle Pattern Applied to Tire Surface 35

Figure 16: Position and Orientation of Radial Cut 39

Figure 17: Test Tire Before (A) and After (B) Cut 40

Figure 18: Horizontal Displacement Caused by Introduction of Radial Cut in Tire 41

Figure 19: Vertical Displacement of Surface Due to Tangential Cut 42

Figure 20: 16x16 Grid, in Red, Shown on Tire at 5 px/mm Scale 43

Figure 21: Old (A) Spot Pattern Compared to New (B) Spot Pattern 44

Figure 22: External Radial Cut on Outer Tire Surface 46

Figure 23: Internal View of Internal Tire Cut 47

Figure 24: Exterior of Tire Highlighting Location of Internal Damage and Region of Interest 47

Figure 25: X (A) and Y Displacement Surrounding External Cut 48

Figure 26: Strain, Exx, of Tire With Radial External Cut 49

Figure 27: Vertical Strain Eyy at Comparable Scale to Exx 50

Figure 28: Min/Max Scaling of Eyy 51

Figure 29: Region of Interest for 3D Measurements 53

Figure 30: X-Displacement in Undamaged (A) and Damaged (B) Tire Areas 54

Figure 31: Y-Displacement in Undamaged (A) and Damaged (B) Tire Areas 54

Figure 32: Z-Displacement in Undamaged (A) and Damaged (B) Tire Area 55

Figure 33: Horizontal Strain, Exx, in Undamaged (A) and Damaged (B) Tire Region 56

Figure 34: Vertical Strain, Eyy, in Undamaged (A) and Damaged (B) Tire Regions 57

Figure 35: Maximum Tire Surface Strain With Internal Cut Rotated 30 Degrees Clockwise from Point of Loading 60

Figure 36: Minimum Tire Surface Strain With External Cut Rotated 30 Degrees Clockwise from Point of Loading 60

Figure 37: Defining a Geometric Mask on Tire Surface 62

Figure 38: Results of Geometric Mask Application to Image 62

Figure 39: Software Reconstruction of 3D Tire Surface 65

Figure 40: Average Minimum Strain and Absolute Change in Strain of External Cut 67

Figure 41: Average Maximum Strain At Internal Cut and Absolute Change in Strain 69

Figure 42: Comparison of Visibility Criteria C2 Between External Cuts on Tire #1 and Tire #2 ... 73

Figure 43: Region of Best Visibility for Internal and External Cut 74

Figure 44: Eliminating Translation and Rotation of Tire Between Frames 76

Figure 45: Example of Re-Rotation Applied to Tire Images 76

Figure 46: Tire Displacement Calculated From Rotating Image Set Without Re-Rotation 78

Figure 47: Compression and Expansion of Damage From Successive Rotating Images 79

Figure 48: Location of Damage on Test Tire, with 1 Indicating the Tangential cut, 2 Indicating the Radial cut, and 3 Indicating the Internal Damage 80

Figure 49: Co-Ordinate System for Tire Re-Rotation 81

Figure 50: Damage Visibility By Type and Position from Re-Rotated Tire Images 82

Figure 51: Sample Strain and Displacement From Re-Rotated Images, Showing Tangential Cut 84

Figure 52: Truck and Shovel at Pit 91

Figure 53: Offloading Ore At Crusher Dump 92

Figure 54: Side View of Haulage Tire At Rest Stop 92

Figure 55: Thermal Image of Truck at Rest Stop 95

Chapter 1: Introduction

1.1 Background and Motivation

Equipment used in the excavation of minerals and soils is subjected to extreme environmental conditions, as well as repeated dynamic loading changes. The tires used to support this equipment undergo a significant amount of damage due to these processes. For ultra-class haul trucks, the tires, which can measure up to 4m in diameter and weigh 5300 kilograms, support loads of up to 80 tons each. Typically, a haulage truck has six or more tires, with two in the front and four in the rear, since the rear tires support more load when the truck is unloading material. On average, tires represent one third or more of the total haulage cost in operations [1].

Haulage roads can be obstructed by loose ore and other material that falls from the trucks, causing a puncture risk to the tires. Outdoor temperatures can range from +/- 40 °C, with road temperatures even higher. Under ideal conditions, a damaged tire can be replaced in 4 hours. In adverse conditions, it can take 8-12 hours to get a truck back in operation after a tire failure [2]. When a truck fails near a bucket excavator or crusher dump, it bottlenecks the entire excavation process and can stall excavation completely, causing significant financial loss.

High demands are placed on the tires, and there is a limited supply of tires produced each year, often at a high cost [3]. After expending its annual supplier quota of tires, a company may be unable to obtain replacements or expand its fleet of equipment without significant additional expense. Consequently, tire failure is not only hazardous to equipment and personnel at excavation sites, but also a time-consuming and costly complication to address.

To prevent premature tire failure, trained maintenance personnel visually inspect the tires for damage, as shown in Figure 1, and remove the tires for repair, when possible, or replacement. The frequency of inspection is affected by the availability of personnel, which in turn affects the likelihood that damage to the tire is detected while it can still be repaired. Currently, each tire is examined for cracks or other damage on a weekly basis. Despite these measures, unaided

visual inspection cannot detect some forms of damage, such as failure due to fatigue stress or inner belt separation. As a result, other monitoring techniques are being investigated.

FIGURE 1: MAINTENANCE PERSONNEL AND ULTRA-CLASS HAULAGE TIRE

*site photographs used with permission of Syncrude Canada Ltd.

Tire pressure and temperature monitoring has been implemented in industry to address the shortcomings of scheduled visual inspection. However, some forms of tire damage do not noticeably affect the pressure or overall temperature of the tire, and consequently may not be detected from pressure and temperature monitoring [4]. Industrial usage complicates other instruments, such as sonic and ultrasonic measurements during driving, by introducing rough and unpredictable road surfaces. Lifespan data indicates that tires are being removed from service ahead of their designed or desired end-of-life [5]. For these reasons, a project was sponsored by Syncrude Canada Ltd. to gain insight into damage mechanisms in haulage tires and investigate technologies that could be used to extend tire lifespans.

1.2 Fault Classification

There is currently no standardized system for classifying tire damage between different corporations or industries for large tires. In general, damage occurs to the tire tread, sidewall, or belts. Figure 2, which uses data reported by Anzabi et al. (2012), shows five years of haulage tire failures from an industrial database, sorted according to their classification system. Noticeably, failure due to wear and "others" accounts for less than 3% of total failures.

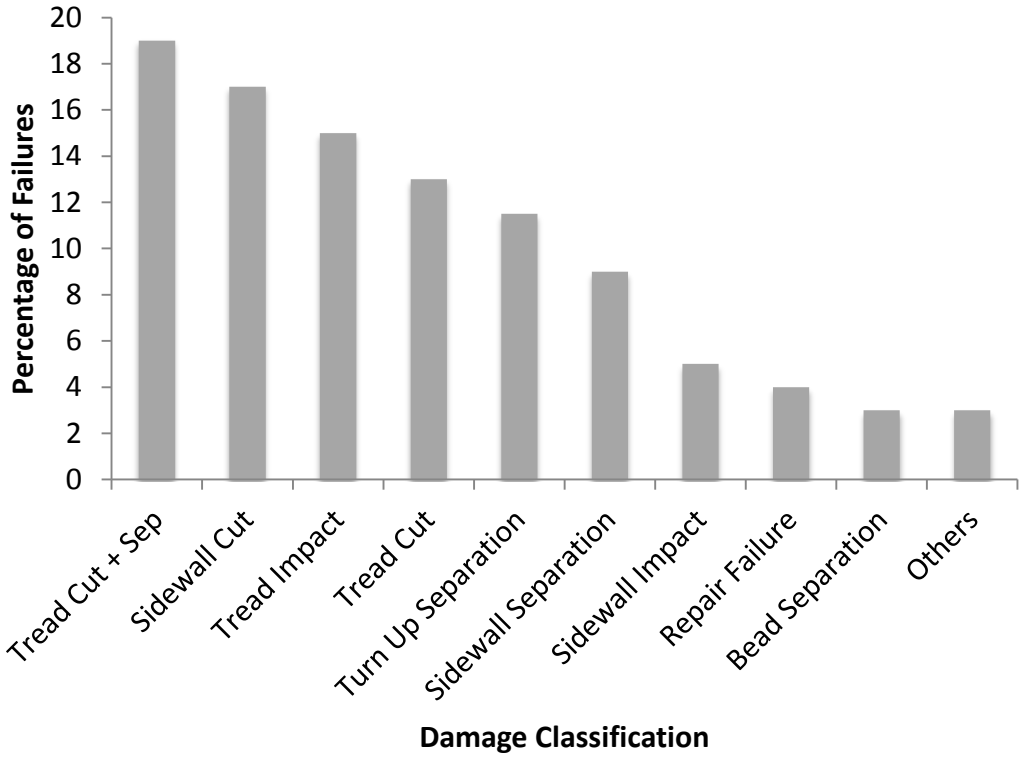

FIGURE 2: PERCENTAGE OF REPORTED HAULAGE TIRE FAILURES BY TYPE (DATA: ANZABI 2012)

Sidewall cuts, separation, and impacts, account for approximately one third of tire failures. Most sidewall damage occurs on the exterior facing tire surfaces. An optical system facing the tire sidewall could potentially detect a significant amount of damage. Tread cuts and impacts, which account for half of all failures, may not be readily visible but can cause a loss of pressure in the tire, which could be detected optically from sidewall photographs. Figures 3, 4, and 5 show examples of a tread cut with separation, external sidewall cut, and an interior separation.

The tires were irreparably damaged during the course of regular operation at a mining site and removed from service.

FIGURE 3: HAULAGE TIRE WITH TREAD CUT AND SEPARATION

FIGURE 4: SIDEWALL CUT IN HAULAGE TIRE

The damage highlighted in Figure 4, although noticeable, was not the main cause for the decommissioning of the tire. An internal view, shown in Figure 5, reveals severe internal delamination that was not externally visible. The newly separated layers can rub against each other, which could potentially cause damage.

FIGURE 5: INTERNAL VIEW OF BELT SEPARATION IN HAULAGE TIRE

Fatigue failure, although not frequently cited in the haulage study as the cause of tire decommissioning, should also be considered in the decision of where to mount cameras for inspection. This type of failure can cause violent, sudden decompression of the tire [2]. Coupled with the difficulty of detecting fatigue damage manually, this increases the importance of developing an inspection system that could potentially prevent this type of failure. Fatigue affects the area closest to the hub, including the tire bead. The external portion of this area is visible from sidewall photographs.

While fatigue failure was reported as less than 2% of tire failures at the industrial site, other sources report fatigue as the cause of up to 20% of commercial tire failures [6]. This discrepancy is part of the motivation for a re-examination of the damage classification system currently used for haulage tires.

1.3 Project Definition

To improve the lifespan of tires used in heavy excavation machinery, such as ultra-class haul trucks, there is interest in developing other monitoring techniques that can be implemented as part of an inspection and maintenance plan. There is also interest in understanding damage mechanisms in tires to design products that are more resilient in adverse conditions.

Several inspection techniques, including laser distance measurement, thermal imaging, acoustics, stereo imaging, and temperature and pressure monitoring were reviewed for application to condition monitoring and fault detection in haul truck tires [7]. Key factors included the ability to automate the inspection process, a procedure that was minimally invasive to existing operation of the tires, and providing a cost-effective solution. Digital image correlation (DIC) was chosen for further investigation based on these criteria, as it allows for remote, safe inspection of the tires, and could potentially be implemented in an automated computer system.

An optical inspection system is developed to assess the feasibility of using DIC software to measure displacement and strain from a tire surface, with the aim of detecting tire damage. It was expected that damage or changes to the condition of the tire will result in a change in the strain field at the tire surface. DIC is a well-established method for obtaining strain, displacement, and velocity measurements, especially in materials which are otherwise difficult to instrument [8][9]. The strain information obtained from this system could also contribute to other work that will further advance the understanding of how damage forms and spreads in haulage tires.

Radial ply tires are difficult to characterize due to their multi-layered composite shell structure. Consequently, most tire studies are either experimental, or work with complex computer-based models to predict tire behaviour. This particular project focuses on experimental work that establishes the feasibility of using an optical system to detect tire damage. A complementary investigation is also examining tire reliability data and studying crack formation in tires using finite element analysis (FEA) on computer models [10].

1.4 Objectives

The objective of this work is to determine the feasibility of detecting damage in tires, using an optical DIC system to obtain displacement and strain measurements. This work aims to contribute to the understanding of strain behaviour in damaged tires, and also towards the future development of a tire condition monitoring and fault detection system. To accomplish this, a laboratory-scale system is developed to test tires under multiple loading and pressure conditions. A procedure for measuring the strain at the tire surface is created, and the capabilities of commercial DIC software are explored for this particular application. The uncertainty in DIC measurements for this application are determined. Multiple tire faults, including external and internal damage, are observed under load to investigate the visibility of different features in pneumatic tires using DIC. Necessary steps for a field implementation are also discussed, such as pre-processing of tire images to remove tire rotation between frames.

1.5 Organization

Following the first chapter of this thesis, a review of relevant literature in tire failure, digital image correlation, and tire inspection is presented in Chapter 2. Fundamental theories of digital image correlation and tire mechanics are explained in Chapter 3. The equipment, software, and procedure used to study tire damage is provided in Chapter 4. Chapter 5 covers the results of the study of tire damage, measuring displacement and strain on a tire sidewall, examining internal and external damage, defining metrics for evaluating damage visibility, and determining where damage is most visible. Finally, Chapter 6 discusses future applications of this work in both laboratory and industrial settings as well as conclusions from this study.

Chapter 2: Literature Review

The literature for this investigation falls into two categories: tire mechanics and tire failure, and inspection techniques for tires or similar objects. The following section provides an overview of the literature used to approach the problem of tire monitoring and damage detection using optical strain measurement.

2.1 Tire Failure

2.1.1 Theoretical

Few analytical models exist for describing tire failure, due to the complex anisotropic composite structure of radial tires [55]. Mathematical models such as netting and meshing analyses have been used to describe tire behaviour under load (Clark, 1981). Netting methods assume that the tire pressure is carried through the cord, neglecting the bending of the rubber. Mesh-based models, typically implemented in FEA (finite element analysis) models, are used to solve particular problems, but struggle with large deformations in the tire and the large difference in stiffness between rubber and tire cords.

Finite element analysis (FEA) computer models are used to predict tire behaviour and analyze tire damage. Passenger tires, representing a much larger section of the overall tire market, are most frequently modeled. A current summary of challenges and developments in FEA modeling of tire mechanics can be found in Kaliske (2010). Developments in computer processing are allowing for increasingly accurate tire models, both in terms of mechanical properties as well as in describing tire-pavement interaction. Principles of fracture mechanics and strain energy (Braun, 1997 and Rice, 1968) are being implemented to improve tire reliability and understand crack propagation. Fuzzy analysis is being combined with FEA tire models to observe how uncertainty in inputs affect tires, with the goal of developing more robust designs (Serafinska, 2012). Opportunities exist to extend these models to include tire damage, and compare the theoretical response of the model to strain in an actual tire to improve the understanding of damage mechanisms in tires.

An accurate tire model requires detailed constitutive relationships describing the material behaviour of the belt, tread, and bead under loading. This is approached by measuring the strain of sample specimens under the desired loading conditions, such as in Sokolov (2010). Chevalier et al. (2001), and Moser et al. (2007, 2011) use DIC to measure strain in rubber test specimens and validate predictions from FEA models. These papers suggest that it could be possible to measure strain in a rubber tire using DIC, using a specially prepared sample with a high-contrast dot pattern.

Using the experimentally obtained rubber properties in a FEA tire model, Sokolov (2010) was able to determine that higher temperature decreases the fatigue life of a tire. The life cycle of multiple passenger tire brands was calculated based on a FEA analysis of $3x10^6$ loading cycles. This is a useful approach when similar testing is impractical or infeasible in an experimental or laboratory setting.

2.1.2 Experimental Studies

Experimental approaches are favoured in tire studies because of the complex construction and geometry of most tires. Historically, tire strain was measured from probes and transducers creatively mounted on internal or external tire surfaces. Conventional strain gauges are generally ineffective, due to the flexibility of the rubber, resulting in less conventional approaches to strain measurement in tires, such as liquid, clip, or cord gauges (Clark, 1981).

Tire response to externally imposed conditions has been investigated in a laboratory setting. Carrerra et al. (2003) and Castillo (2006) both describe the design and instrumentation of laboratory-based tired testing systems. Although this work focuses mainly on tire inspection, understanding tire failures and damage mechanisms is important for developing useful inspection criteria.

Forensic studies analyzing tire failure focus on drawing conclusions from samples of failed tires as opposed to replicating damage in the laboratory. Daws (2003) compares laboratory-generated damage to samples obtained from passenger tires in field service, and concludes that, for tread separations, there is high similarity between the two. In the laboratory, Daws observes that the tire pressure does not change during a tread separation event. Additionally,

Daws notes that underinflation and overloading of the tire both contribute to premature failure by increasing the rate of crack propagation.

Pressure and temperature measurement has been implemented at some mining sites. Multiple candidate technologies, such as laser distance measurement, digital image correlation, and thermal imaging were evaluated for application to haulage tire monitoring. A detailed description can be found in Anzabi et al. (2011).

Like Daws (2003), Giapponi (2008) also draws some conclusions on tire damage through forensic analysis. Of particular interest to this investigation are Giapponi's observations of the effects of tire position on tire life. For large vehicles, Giapponi notes that exterior tires fail sooner than inner ones, and also that the outwards-facing side of a tire is more likely to sustain critical damage than the inner-facing surface. For on-site tire monitoring, this suggests that a camera system focused on the outer sidewall of the tire could detect a significant percentage of failures, which is also reinforced by industrial data presented in Anzabi et al. (2011).

2.2 Inspection of Tires and Composite Rubber Materials

Optical measurement techniques offer multiple advantages over a simple strain gauge installation, such as increasing the potential for full-field measurements, removing error due to gauge separation, and eliminating the need for wiring or bulky wireless transmitters. Optical measurement methods are used to analyze tires and complex rubber samples. These techniques include, but are not limited to, digital image correlation, laser scanning, polariscopy, and reflected light [24]. Applications of these methods are discussed in the following section.

2.2.1 Optical Tire Inspection Techniques

An advantage of DIC and optical tire inspection techniques over many physical gauges and transducers is that they provide full-field strain readings over the surface visible to the camera, as opposed to single-point measurements. Similar to the testing apparatus used in this work, Chow and Woo (1981) used an Instron Universal Testing Machine to apply loading to a stationary tire while a camera was pointed at the tire sidewall. Displacement was measured using a polariscope to measure the distortion of a photoelastic coating applied to the tires.

Using this system, it was observed that a vehicle load could cause changes in the surface strain field near the point of load application, up to 90° from the center of the load. The greatest strains were measured at the upper and lower sidewall, which was attributed to the bulging of the sidewall due to load application. These are useful observations which can be compared to results obtained using digital image correlation, in Section 3.4.

Another early method of optically measuring strain on a tire sidewall was the grid method. The grid method, as the name suggests, requires a grid pattern applied to the side of the tire. If applied with a paint product, as in Barson and Gough (1962), the grid pattern can be physically transferred from the tire to another medium for recording and measurement during or after the experiment, or simply photographed. The grid method used similar principles to DIC to obtain displacement measurements, but required manual measurements instead of automated computer calculations.

Instead of examining the sidewall of the tire, Castillo et al. (2006) observed the contact patch on the tire tread as load is applied through the tire and onto a glass plate. The interference of light reflected internally through the glass plate creates darker and lighter image regions and can be related to the pressure on the glass plate. Similar to DIC, careful camera calibration is required for this system to return accurate measurements. Tests indicate that this method can highlight pressure differences on the plate due to tread damage. However, the use of a glass plate would be impractical in a field setting with 400+ ton trucks, and this method was not considered for application to the problem of haulage tire monitoring.

Chen et al. (1993) also examined the tire tread for faults using digital images. Instead of DIC, however, they developed a surface inspection algorithm that finds shapes from a template, using knowledge of the tread pattern, to detect irregularities in the tread. While this is effective in a manufacturing environment, due to the variation in tire models on-site as well as wear and environmental effects, it could be less practical in a field setting than other methods.

A developing strategy is the use of edge-detection and other image processing algorithms on low-resolution JPEG tire images to detect external cuts, such as Wiseman (2010). As with digital image correlation, this method is sensitive to changes in tire colour, surface texture, and

orientation. However, it may be quicker than 3D surface strain measurements, and could be a viable addition to a tire monitoring program using webcam data, for example.

Thermal imaging has been used to detect delamination in tires (Gros 1997). Gros (1997) studied the thermal profile of delaminated tires with an applied thermal current. It is possible that damaged off-road tires could also exhibit similar thermal changes during operation. A thermal camera could potentially be added to an optical inspection system for additional tire data and enhanced fault detection capability.

2.2.2 Haulage Tire Inspection

At the location of interest, tires are monitored through visual inspection as well as some pressure and temperature logging. Improper off-road tire inflation can result in damage from over-flexion of the tire, heat buildup, or increased wear (Zhou 2008). Various commercial products are available to monitor and analyze tire installation and operation pressure (Mining Magazine 2012, Carter 2011). As previously explained, some forms of tire damage are not detectable from pressure monitoring (Daws 2003).

Temperature and pressure monitoring has also been implemented by most major manufacturers of haulage tires (Otraco 1993, Brothen et. al. 2008). This provides a global measurement of the internal air temperature, and can be correlated with pressure changes to determine if pressure changes are due to air loss or a change in operating temperature. Tread temperature can also be recorded by inserting a probe into the tread. These measurements can be taken remotely and continuously, and are recorded approximately once per minute. Some systems also store a history of the temperature and pressure in each tire. It is possible for systems to activate an alarm when certain thresholds in either measurement are exceeded and notify appropriate personnel. (Carter 2011)

2.2.3 Other Monitoring Techniques

Acoustic monitoring is commonly used in passenger car tires (Orrell 2008). Noise introduced by the irregularity of haul roads is a concern for industrial applications in haulage tire monitoring. For manufacturing or maintenance purposes, such as inspecting re-treaded tires, acoustic and ultrasonic approaches have a high detection rate for detecting cord damage in steel-belted tires (Dos Reyes 1996).

Strut pressure is used in place of acoustic measurements to characterize truck performance on haulage roads. The suspension vibration or strut pressure changes are used to determine the road conditions (Hugo et al. 2007). Changes in the tire pressure alter the stiffness of the tire-suspension damping element, noticeably affecting the system response (Meyer 2012).

2.2.4 Concluding Remarks

Multiple methods exist for quantifying and understanding tire behaviour, from mathematical and finite element models, to experimental techniques such as strain gauging and optical measurements, to industrial practices such as temperature and pressure monitoring (TPMS). Limitations of damage detection using TPMS present the opportunity to develop monitoring solutions using other technologies. Experimental work has shown that conventional methods such as strain gauge installation are impractical for implementation in rubber tires. Optical methods, such as DIC, which will be further discussed in the following section, offer the advantage of being non-contact, and providing full-field measurements. The potential also exists for using experimentally obtained measurements from an optical system to validate FEA and other mathematical models to improve the understanding of tire behaviour and damage mechanisms.

Chapter 3: Theory

The project uses an optical inspection method, in this case, DIC, to detect damage in a loaded tire. The theory section of this thesis explains tire behaviour under loading, and describes how DIC algorithms obtain scaled measurements from digital images.

3.1 Digital Image Correlation

It is anticipated that tire damage will have an effect on the deformation of the tire, quantifiable by measurements of displacement and strain. Various methods can be used to determine the displacement of a specific shape, object, or region in an image. This section focuses on correlation algorithms which calculate displacement and derived properties such as velocity and strain, with particular emphasis on the implementation of these methods in a commercial software package. A commercial software package (DaVis 8 by LaVision Gmbh) was used for cross-correlation processing to obtain displacement and strain fields.

3.1.1 Application to Mechanics and Tire Inspection

Optical strain measurement has been successfully used in many fields where the application of a traditional strain gauge or piezoelectric strain measurement device would prove impractical. Examples include dental strain imaging [41] and examining the loading effects on a mouse tibia [42]. Some techniques take advantage of the natural texture of the object, while others apply a speckle pattern to enhance the accuracy of the correlation. Correlation algorithms and other methods are implemented to determine the displacement, and ultimately the strain on the object.

Digital image correlation is an established measurement technique in applied mechanics. A review of DIC techniques used in mechanics is presented in Orteu (2009), highlighting the wide range of applications, and the validity of this method at both small and large scales. Accuracy of 3D methods is presented as a factor of camera resolution, camera angle, calibration, and correlation strength. These metrics are used to evaluate the results obtained from the tire testing experiments.

DIC can be used to measure strains in rubber and other materials, and has been successfully applied to problems in tire measurement as well as composite material characterization. Moser et al. (2010) verify the accuracy of DIC measurements on a rectangular rubber coupon, determining it to be accurate to within +/- 0.01 strain for a normal strain level of 0.2 or below, or +/- 0.02 strain for normal strains from 0.2 to 0.284 [19]. In the same work, they compare DIC measurements to finite element (FE) models of the tires under investigation, and find an average in-plane peak-to-peak strain difference of +/- 0.024. For shear strain, the difference increases to 0.05.

A second work by Moser et al. (2007) investigates the internal strains in a tire by removing a piece of material from the tire, in effect damaging it [18]. While the intent is not to observe tire damage, it does show that strain can be measured even in a damaged or altered tire area. In this case, the average error between the FE model and DIC measurements was 6%.

Matsuzaki et al. (2010) used DIC for monitoring tire strain to improve tire performance [27]. They compare tire surfaces obtained using DIC to depth measurements from a laser scanning system, finding an average difference of 0.1 mm, or 0.3%, between the two out-of-plane measurements for both a bent aluminium beam and a 225 mm wide tire. They found that the error between DIC measurements and strain gauges, on a flat aluminium surface, to depend solely on the pattern matching error in DIC, which caused a discrepancy of approximately 0.02 strain, regardless of the absolute value of strain in the sample.

3.1.2 Correlation Theory

Cross-correlation methods use a statistic weight function to evaluate the similarity of windows between images in a sequence. Each image or area of interest is divided into *NxN* windows, where *N* refers to the size of the window, in pixels. A non-repeating speckle pattern applied to the surface provides the information for the correlation.

The correlation process, as applied to a tire surface, is illustrated in Figure 6. The correlation function uses both the light and dark regions of the image to evaluate the similarity between a given window and its neighbours within an *N*/2 radius in the following frame [44]. If a suitable

match is found, then the resulting displacement vector is returned. A detailed explanation of the theory and applications of DIC can be found in Westerweel (1993) [45].

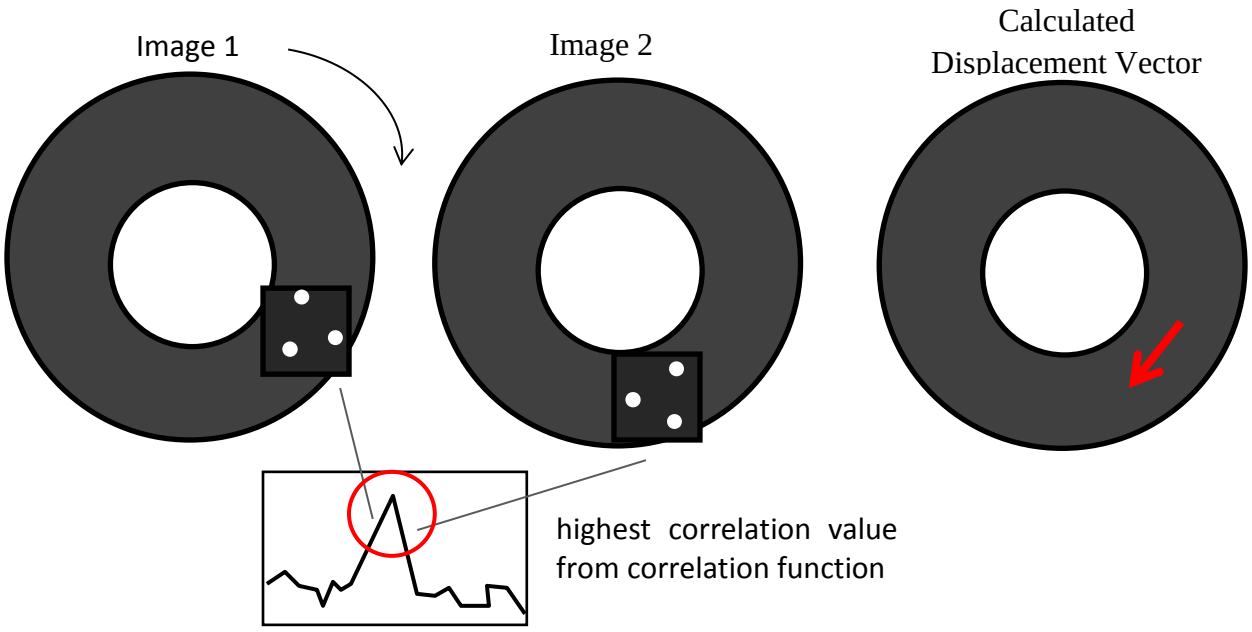

FIGURE 6: DISPLACEMENT VECTOR CALCULATION ON TIRE SURFACE

While improvements to correlation functions and associated algorithms are continually under development, the core idea remains the same. The function compares the intensities between windows to determine their similarity, and find the most likely position of a window in subsequent frames. An example of a typical correlation function is [44]:

$$C(dx,dy) = \sum_{x=0,y=0}^{x<N,y<N} I_1(x,y)I_2(x+dx,y+dy), -\frac{N}{2} < dx,dy < \frac{N}{2} \qquad [1]$$

where *C* is a two-dimensional array containing the correlation strengths for all possible integer displacements between the windows, *N* is again the size of the interrogation window, in pixels, and I_1 and I_2 are the intensities of the first and second interrogation windows, respectively. A detailed explanation of the theory behind correlation functions can be found in Keane and Adrian (1992) [46].

To speed up the correlation process, a fast fourier transform (FFT) is applied to the two frames. This method is described in Ronneburger et al. (1998) [47]. The simplest application can be written as follows:

$$\boldsymbol{R = \frac{FFT^{-1}\left(FFT^{*}(a') \cdot FFT(b')\right)}{RMS(a') \cdot RMS(b')}} \qquad [2]$$

where R is the correlation strength, a' and b' are the normalized intensity values of each window. Compared to individually comparing the intensities of every pixel in the two windows, which requires order N^2 computations, this method uses a number of operations of order $N\log N$, providing a more efficient method of evaluating the correlation between two windows.

The correlation co-efficient has a value between 0 and 1. Correlation data must be interpolated to return displacement to sub-pixel accuracy. Multiple estimation methods exist to determine the position of the correlation peak to sub-pixel accuracy by fitting a function to the correlation strengths of neighbouring windows [44]. This is particularly important in applications where the particles being tracked have a diameter of <2 pixels. Commercially available DIC software has a correlation accuracy less than 0.1 pixels [50]. Performance comparisons of multiple algorithms and products are available in publications from PIV challenge conferences [48][49][50].

When using DIC algorithms, the displacement of the window between frames should be no greater than one quarter of the length of the window to ensure that the displaced region in subsequent frames is within the search area. To calculate greater displacements, an initial offset can be applied to the search area, or an iterative process can be used to refine the window size from a larger, for example, 256 pixels, to a smaller size, such as 32 pixels. Window dimensions are limited by the size of particle or dot in the image. Each window must contain at least 5 dots/particles to guarantee a strong correlation [46]. Error can be reduced by 25%, using windows with a 50% overlap as opposed to smaller windows with no overlap [51].

3.1.3 Calibration Theory

Recording an image can be thought of as transferring an object from global co-ordinates to image co-ordinates, such as *x* and *y* pixel location. It is more complicated to perform the reverse operation and obtain global co-ordinates of an object from its image. With sufficient information obtained through camera calibration, it is possible to make accurate two, and even three-dimensional scaled measurements from an image. Calibration also corrects camera and lens effects that result in image distortion [52].

One method of obtaining calibrated images is to determine the relationship between certain points in the image, and their physical location on the focal plane of the camera. The software (DaVis) accomplishes this by studying one or more images of a calibration target, consisting of a black background with an array of regularly spaced white points. Given information about the known size and distance between points, the software can then re-project the image to correct for perspective and distortion, and determine the scale of the image. RMS error, defined as the sum of least squares difference between a point in the corrected image and its location on the ideal grid, is used to describe the accuracy of the calibration.

3.1.4 Two-Component, 2D Measurements

In-plane (*x* and *y*) measurements can be obtained from a single calibrated image from a single or multiple camera system. A single image of a flat target is sufficient to obtain scale. Cross-correlation is used to analyze a series of images and calculate the in-plane displacement and strain. Velocity can also be calculated if the time interval between frames is known. Error is introduced when the particles or dots being analyzed do not lie on the focal plane or undergo out-of-plane motion. Compared to fluid mechanics problems, loss of particles in the image due to out of plane motion is not expected to be a major concern.

3.1.5 Three-Component, 3D Measurements

Three-dimensional measurements require two or more cameras to resolve the depth of the object [52]. In a multiple-camera system, the images from each camera constrain two degrees of freedom for each pixel. Solving the over-determined system, using a combination of user-selected points and pattern-matching algorithms, obtains the depth of each pixel. Smoothing

functions and in some cases, *a priori* knowledge of the surface, integrate the pixel depths into a three-dimensional reference surface. Deformation and strain are calculated with respect to the reference surface [44]. 3D measurements have a greater computational, and consequently time, requirement than 2D measurements.

To calibrate the cameras, either a special 3D calibration target is required, or multiple images of a flat calibration plate recorded at multiple points along the camera axis. Misalignment between the target plane and object plane can result in triangulation error [53], which can be reduced by defining an offset value between the two planes in the calibration algorithm. An offset value was measured in experiments and incorporated into the calibration procedure.

3.2 Tire Mechanics

This section explains concepts in tire mechanics that are pertinent to the investigation to be undertaken, such as tire deformation under load and the distribution of load in the tire carcass. Additionally, the classification of tire damage is discussed.

3.2.1 Tire Deformation

Vehicle tires are a complex system comprised of multiple superimposed layers of steel cord and rubber matrix, interacting with the pressurized air inside the tire. Consequently, stress and strain prediction in tires is complicated and often determined experimentally or through finite element analysis. Tire deformation, however, can be predicted from tire stiffness using existing theoretical models, and is explored in this section.

Exaggerated geometry for estimating tire deformation due to loading is illustrated in Figure 7, and defined below. Measured in millimeters, R refers to the original outer radius of the tire, R' represents the outer radius of the tire after deformation, d is the displacement of the tire, and W is the section width of the tire.

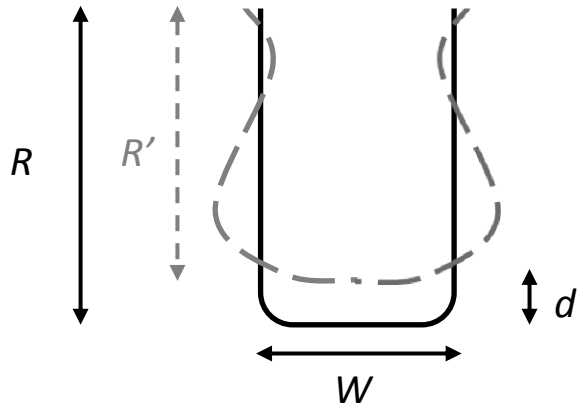

FIGURE 7: TIRE GEOMETRY UNDER LOAD

By treating the tire as a simple spring, the radial deformation due to an applied load on the tire can be expressed, using Hooke's Law, as:

$$d = - F/K \qquad [3]$$

where *F* is the radial force applied to the tire, in newtons, and *K* is the tire stiffness, in newtons per millimeter.

The tire stiffness can be predicted from Rhyne's equation [54]:

$$\boldsymbol{K = 2.68\,P * (W * D)^{0.5} + 33.1} \qquad [\mathbf{4}]$$

where *P*, in megapascals, is the inflation pressure of the tire, *D*, in millimeters, is its diameter, and *W*, also in mm, is its width.

The flexible tire sidewall can dramatically change in profile depending on the pressurization and loading of the tire. For comparison between various laboratory experiments and site conditions, it is necessary to have a metric that describes the shape of the tire. A simple measurement of tire deformation that can be used for this purpose is the change in radius of the tire, excluding the rim, divided by the original radius of the tire at the same inflation pressure, measured vertically.

3.2.2 Load Distribution

According to Clark (1981), tire stress is the sum of multiple loading effects. In an unloaded state, tension in the tire cords balances out the internal pressure of the tire [55]. During operation, the tire must transmit the load from the bottom contact patch to the wheel rim. One mechanism of transmission is through the resulting tension in the upper sidewall from loading on the bottom of the tire, which pulls the bead up against the wheel rim, transmitting the upward force from the ground through the tire to the rim. Some load is also carried directly through the structure of the tire, from the contact patch through the sidewall, again to the bead, which presses against the wheel rim. Other minor effects also affect the load transmission and stress in the tire. Essentially, stress distribution in a tire is determined both by the stiffness and form of the tire carcass as well as the internal inflation pressure, in addition the applied load to the rim and contact surface.

The theory of DIC and tire behaviour was used to develop the testing rig used to investigate the feasibility of damage detection in tires using DIC, described in Section 4.

Chapter 4: Design and Commissioning of Experiment and Methodology

This chapter describes an experimental approach to investigating the feasibility of using measurements obtained from digital images using DIC algorithms to detect damage in tires. The aim is to produce repeatable laboratory results that can be used to guide the future development of an industrial monitoring or inspection system. An experimental apparatus has been constructed to load the tires and record images. The development of this system is described in Section 4.1, Design of Experiment, which outlines the system requirements, parameters of interest, and a general procedure for conducting experiments. The tire testing system itself is described in Section 4.2, Equipment, which also describes the tires chosen for examination, their preparation, and the DIC software used to analyze images and obtain measurements. Section 4.3, Preliminary Work, describes the results of an investigation designed to explore the feasibility of collecting measurements from a tire and to determine experimental parameters such as loading and tire pattern.

4.1 Design of Experiment

Before conducting experiments, it was first necessary to determine the desired outcome of an examination of damage visibility, in terms of controlled, manipulated, and responding variables. The responding variables of interest are the displacement and strain on the tire surface under loading, and are expected to vary between undamaged and damaged tires. To achieve the desired control and response in the test apparatus, a list of requirements was drafted. The specifications of the test apparatus developed for this application are also listed.

4.1.1 System Requirements

System requirements for a tire testing apparatus were drafted. The list is as follows:

1. repeatable load application
2. measurable angular position and angular velocity of tire
3. ability to rotate tire
4. unobstructed view of tire sidewall

A horizontal end mill was retrofitted to serve these purposes, as it is able to load the tire in a controlled manner and rotate the tire, and can be equipped with indicators to measure the angular position and velocity of the tire. The operational limitations of this apparatus are provided in Table 1. The specifications were used to drive decisions in the design of the system, such as an attachment to mount tires to the mill, and also guided the selection of appropriately sized tires for the apparatus.

Table 1: End Mill Specifications

Parameter	**Limitation**	**Limiting Factor**
Load	200 kg	Mill table hydraulics
Driving torque	75 N*m	Spindle Power
Minimum tire diameter	30 cm	Vertical range of mill table
Hub shaft diameter	2.5 cm	Tool holder
Min. angular rotation	85 RPM	Mill controls and drive

4.1.2 Variables of Interest

Using the tire test apparatus, experiments were conducted to assess the feasibility of implementing an optical system for fault detection in tires. Table 2 lists how variables were examined in order to provide an understanding of the capabilities of the optical inspection system as well as the tire behaviour. Experimental variables were classified as either manipulated, responding, or controlled. A range of expected values of the variables is given, along with deciding factors that determine the values to be used in experiments. Key decision parameters, which are shaded in Table 2, are the loading on the tire, its deformation in response to the load, and the surface strain arising from the associated stress in the tire. Displacement and strain on the tire surface are expected to differ between undamaged and damaged regions.

Table 2: Variables of Interest

Variable	Type	Range	Deciding Factors
Tire Displacement	Responding	0mm-30mm	Load Pressure Safety
Surface Strain	Responding	1%-25%	Same as Above
Load	Manipulated	0-200 kg	Safety Mill Table
Tire Pressure	Manipulated Controlled	0-310 kPa	Safety Tire Specifications
Tire Angle	Manipulated Controlled	0-360°	Processing Method
Mill Table Vertical Displacement	Manipulated Controlled	0-23 mm from bottom of tire	Safety Geometric Similarity
Tire Pattern	Controlled	1-10 pixels 0.1-1.0 pixels	Spatial Resolution Application Method
Rotation Speed	Controlled	0 RPM 40-2000 RPM	Safety Shutter Speed
Camera Angle	Controlled	20°-30° (optimal)	Out-of-Plane Resolution Surface Reconstruction
Shutter Speed	Controlled	10µs-60s	Blur Signal-to-Noise Ratio
Lens Aperture	Controlled	F2.8-F22	Depth of Field Signal-to-Noise Ratio
Camera Distance from tire	Controlled	1.0-2.5 m	Spatial Resolution Lens Zoom
Lighting	Controlled	1000W	Equipment
Tire Damage	Controlled	Not applicable	Safety

4.2 Equipment

A testing apparatus meeting the system requirements was developed and is described in Section 4.2.1, Tire Testing Apparatus. The cameras and accompanying accessories used to record and calibrate digital images of the tire are discussed in Section 4.2.2. The selection criteria for choosing tires to investigate in the laboratory is described in Section 4.2.3, as well as the surface preparation required to ensure that the DIC software can obtain measurements from the tire. The justification in choice of software used to analyze the images is discussed in Section 4.2.4.

4.2.1 Tire Testing Apparatus

An apparatus, henceforth referred to as the tire testing rig, was commissioned to provide accurate, repeatable tire data. A vertical end mill, shown in Figure 8, was retrofitted with a custom-built load cell and mounting hub to which the tires are attached. Calibrated strain gauges applied to the hub sense the amount of force applied to the tire, to a maximum load of 200 kg, while a spindle dial indicates its angular position. The calibration data for the load cell is presented in Appendix A: Load Cell calibration. When required, the rotational speed of the tire can be adjusted using the mill controls and measured with a tachometer attached to the hub.

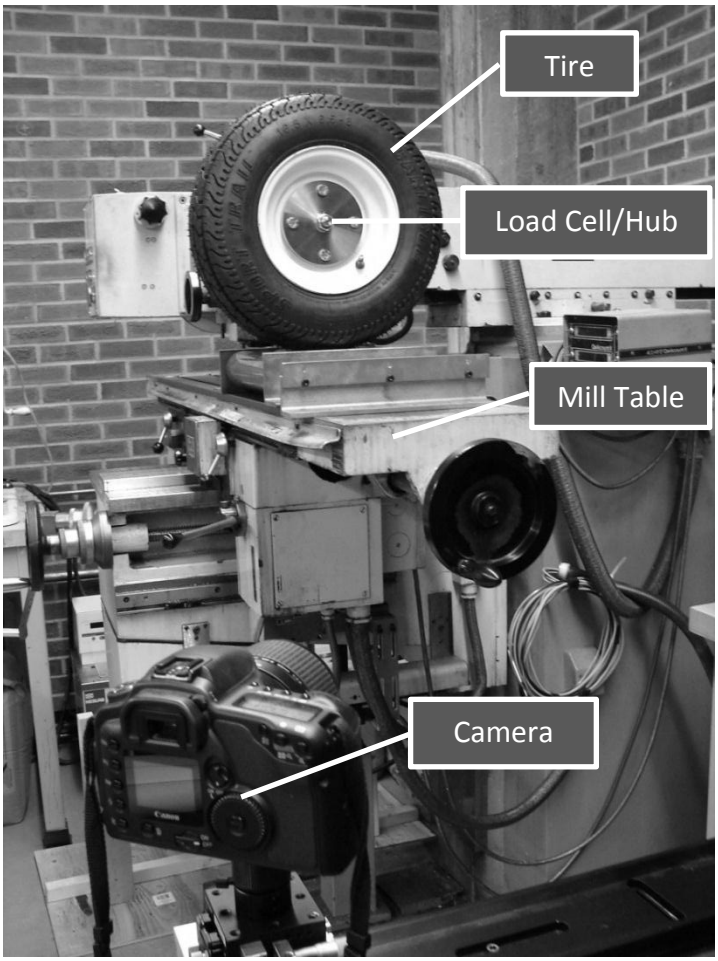

FIGURE 8: TIRE TESTING APPARATUS, CAMERA, TIRE

Cameras are focused on the exterior sidewall of the tire. Each camera is held by a mount which provides three axes of fine rotation control, which is itself mounted to a rail which controls translation of the cameras perpendicular to the tire axis. A 1000W light source is also attached to the rail to illuminate the tire surface. An overhead view of the arrangement of the cameras, light source, and tire, is shown in Figure 9, which is not to scale. The cameras were placed 1.5 meters from the tire. The angle between each camera and the centerline of the tire is represented by φ.

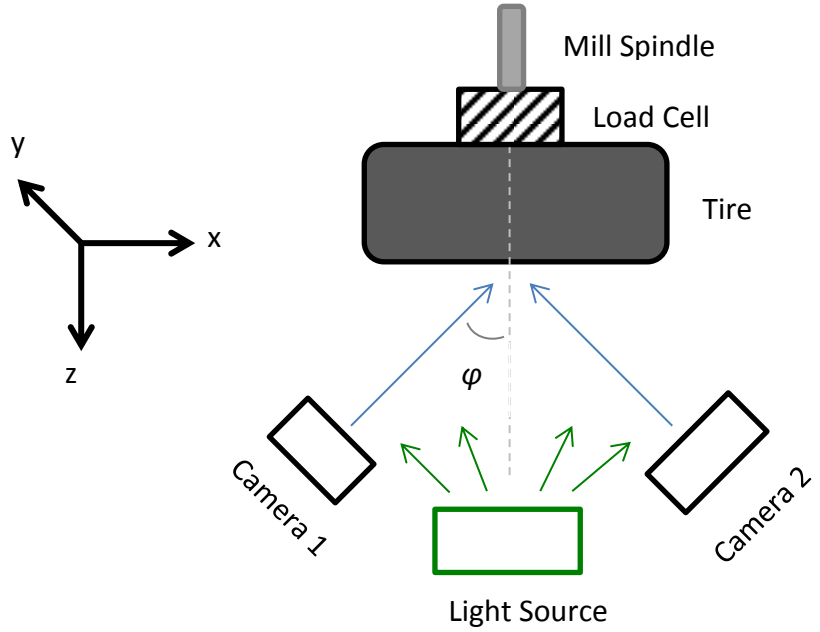

FIGURE 9: OVERHEAD VIEW OF CAMERA INSTALLATION

Typically, camera angles between 15°-30° were used for the experiments, depending on the distance between the cameras and the tire, which was adjusted to "zoom" in or out of areas of interest. A greater angle increases the accuracy of out-of-plane measurements, but decreases the portion of the tire that lies within the focal plane of the camera. Lawson and Wu (1997) present an experimental analysis of camera angles, and conclude that the optimum angle is between 20°-30° [56]. Within this range, and with an aperture greater than F16, they expect 1-2% error for in-plane displacement measurements, and 3-4% for out of plane measurements.

The depth of the focal plane can be improved by increasing the f-stop used in experiments to reduce the size of the lens aperture. The maximum available lens aperture was used for experiments, which was F22 for the Canon cameras and F16 for the AVT cameras.

4.2.2 Cameras

To resolve features in three dimensions, two or more cameras are required. Early proof of concept experiments used 8-bit images from consumer DLSR (digital single lens reflex) cameras, which were upgraded to 14-bit cameras for subsequent trials. Table 3 lists the relevant features of each camera, which can also be obtained from the manufacturer's website .

The main advantage of the AVT cameras over the consumer cameras is the ability to record 14-bit images, which reduces the signal-to-noise ratio in the images, increasing the accuracy of the digital correlation. Additionally, these cameras are capable of recording images at 17 frames per second, which will be useful in future studies where images are recorded with the tires in motion.

TABLE 3: COMPARISON OF CAMERA SPECIFICATIONS

Model	Resolution	Image Quality	Megapixels	Frame Rate
Canon Rebel XT	3456 x 2304	8-bit	8	3 fps
Canon Rebel XTi	3888 x 2592	8-bit	10.1	3 fps
AVT GX3300	3296 x 2472	14-bit	8	17 fps

4.2.2.1 Lenses and Accessories

The AVT cameras were equipped with a 50mm Nikon Nikkor lens, with an aperture range from F2 to F16. Scheimpflug adapters were installed between the lens and camera to align the focal plane of each camera with that of the tire surface by adjusting the lens angle. The arrangement of the camera, lens, and tire, viewed from above, is shown in Figure 10.

Without a Scheimpflug adapter, the un-aligned object plane is parallel to the image plane of the camera, which are both drawn in solid grey lines in the figure. The un-aligned object plane is skewed relative to the surface of the tire, which can cause the edges of the tire to be out of focus in the image. A Scheimpflug adapter is used to adjust the object plane so that it is aligned with the tire surface, shown as a dashed black line, which results in the entire tire surface being in focus. The Scheimpflug point, defined as the intersection between the aligned object plane and the image plane, is used as the origin of the line defining the lens plane, and determines the angle to which the lens must be adjusted using the adapter.

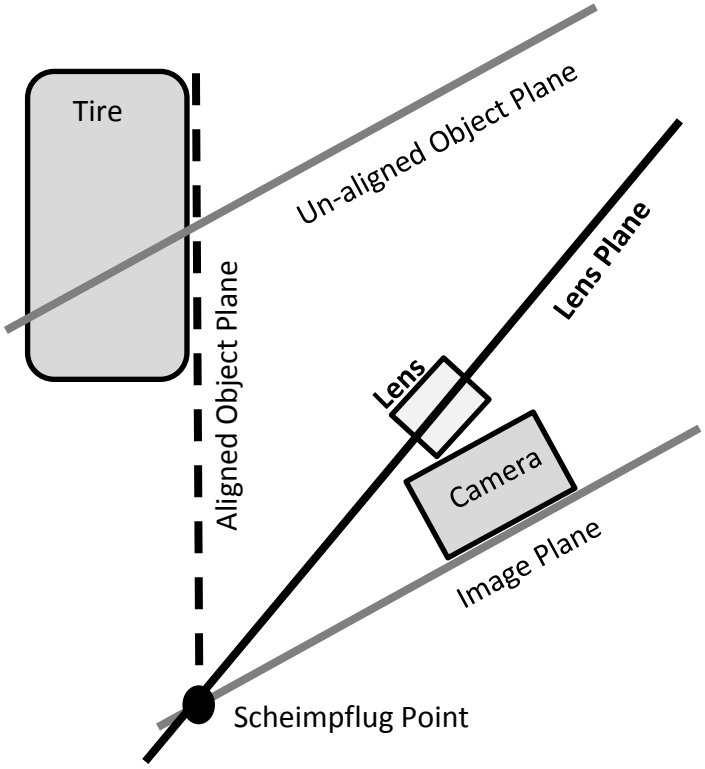

FIGURE 10: CORRECTION OF FOCAL PLANES USING SCHEIMPFLUG ADAPTER

4.2.2.2 Calibration Target and Procedure

A target, pictured in Figure 11, was used to calibrate images from the cameras. It has a 42 x 42 grid of 3 mm white dots spaced 15 mm apart over a black background. To obtain 2 component, 2D measurements, one calibration image is required. For out-of-plane measurements, two or more calibration images are required at different depths. With polynomial calibration, the target must be in the same planar alignment with equal spacing between each set of images.

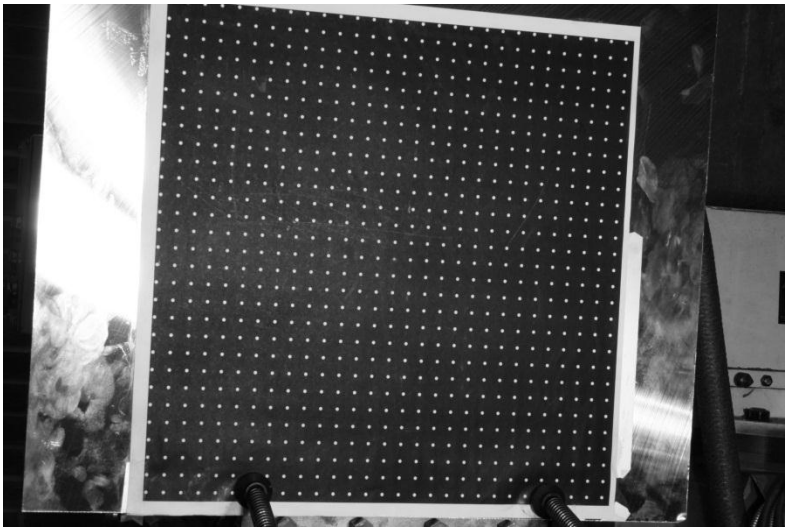

Figure 11: Uncorrected Image of Camera Calibration Target

One image per camera is sufficient to correct distortions and scale the image for two-dimensional measurements [52]. Figure 12A and 12B show an example of a highly distorted calibration image rectified back into a regular grid. In this particular case, the severe distortion of the fisheye lens results in artefacts at the edges of the corrected image.

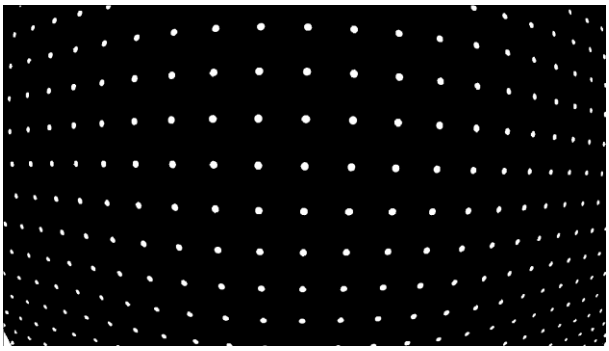

FIGURE 12A: UNCORRECTED CALIBRATION IMAGE

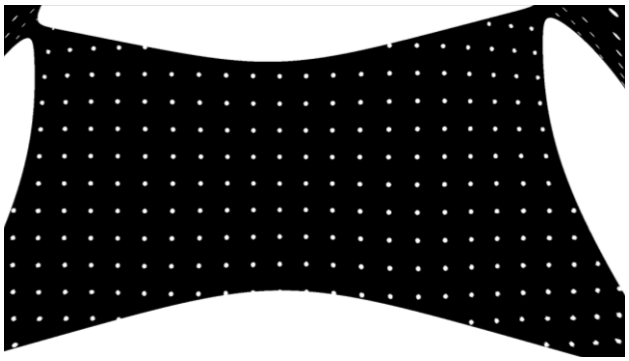

FIGURE 12B: RECTIFIED CALIBRATION IMAGE

Traditional calibration algorithms require the calibration target to be placed at the origin of the co-ordinate system, in this case, the surface of the tire. In experiments, the offset between the tire surface and calibration plate was measured with calipers and incorporated into the calibration algorithm as part of the procedure.

Additional images are required to calibrate the system at different depths for 3D measurements. After recording one image from each camera at the origin and focal plane for the experiment, the target was translated 5.08 mm using the mill controls, which was checked with a dial gage, and a second set of images recorded. This process was repeated a second time to increase the accuracy of the calibration. Using this technique, RMS errors between 0.1 and 0.3 pixels were obtained in image reconstruction, corresponding to a physical distance of 0.05 mm. The RMS error varies with camera angle, target distance, lens focus, and Scheimpflug angle. The overall resolution of potential displacement and strain measurements remains dependent on the window size used for processing, which is also tied to the diameter of spots in the speckle pattern.

Two software options are available for calibration models, a pinhole model and a polynomial fit. In the first option, the software determines camera properties from the point data, which it uses to re-map the images. The parameters of a polynomial fit do not necessarily correlate to camera properties and may not all be statistically significant. For a stereo camera system, a pinhole model uses approximately 22 parameters, while the polynomial model uses 80. Advantages of the pinhole calibration method are that it is not necessary for the calibration target to cover the entire measurement area, and it requires fewer calibration points.

Since the parameters of the pinhole model correspond to physical properties of the actual camera, measurements can be extrapolated outside the calibrated area. The accuracy of a pinhole model, however, is less than that of the polynomial fit [52][53]. When using a polynomial model, it is important to ensure that the area of interest remains within the calibration volume, as errors from extrapolation are greater than when using a pinhole model, since the parameters of the polynomial model do not necessarily correspond to any property of the camera or system. In complicated viewing situations, eg., through a sheet of curved glass, with high distortion, this gives the polynomial model an advantage over the pinhole model.

The polynomial fit was used to calibrate the camera images since it is more accurate, and the calibration target was of sufficient size, with an adequate number of points (>40) to cover the entire tire. Calibration is only valid for a specific focal length and position, so the focus and position of each camera was held constant during experiments.

4.2.3 Tires

16.5”x6.5”x8” bias ply tires were used in the experiment [57]. These were chosen because of their geometric similarity to haulage tires, and for their size, which allows them to fit easily in the testing apparatus. The tire selection process as well as key properties such as deformation, geometry, and construction is discussed.

4.2.3.1 Selection of Tire Properties

The laboratory apparatus is capable of testing a large range of tire conditions, and it is important to also ensure that the results are relevant to site conditions. Given that tire damage is the primary object of this study, selecting an appropriate specimen tire for the laboratory is essential, both for similarity to site conditions and suitability for the test set-up. In the selection of a tire, two geometric properties, the tire deformation and tire dimensions, were specifically chosen to replicate field conditions, albeit at a much smaller scale, as closely as possible. In other ways, the construction and properties of the specimen do differ from haulage tires.

4.2.3.2 Tire Deformation

One parameter that should be controlled to ensure similarity between laboratory and site conditions is the deformation, in percent, of the rubber portion of the tire, as determined by the change in radius. Measured from images obtained on-site in potential inspection locations, such as Figure 13, this deformation is approximately 15%, as calculated in Appendix B. The tire in Figure 13 is carrying the weight of an unloaded truck and was stationary while the images were recorded. To achieve similar results in the laboratory, a displacement of 11 mm needs to be applied to the tire. It is important to ensure that the proposed apparatus is capable of replicating these conditions in the laboratory before proceeding to experiments.

FIGURE 13: SAMPLE IMAGE OF HAULAGE TIRE AT SURFACE MINING OPERATION

Using Equation 4, Rhyne's formula for tire stiffness [54], the calculated loading required to create a similar deformation in the laboratory tire at 165 kPa, typical operating pressure, is 171 kg. The mill table is capable of applying a load of up to 200 kg. The displacement of the mill table required to generate a load of 170 kg is 11 mm, which also lies within the capabilities of the apparatus. If exaggerated deformation is desired to further investigate the effects of loading on the tire, the pressure in the test tire can easily be reduced.

In early tests, a load of 140 kg was applied to a tire at 165 kPa inflation pressure, resulting in a deformation of 18%. Given that the purpose of the formula was to ensure that the test tire could be deformed to 15% using the test apparatus, the estimation was sufficiently accurate.

4.2.3.3 Tire Geometry

Industrial haul truck tires typically used on site have a 2:1 or greater diameter to hub ratio, which is substantially greater than that of a passenger car tire. A smaller tire was procured that could be more readily used in lab-scale studies. A 42 cm (16.5”) radial tire with a 1.8:1 diameter to hub ratio was used for experiments. Figure 14 gives a side-by-side comparison of the laboratory tire to a haulage tire.

(A) **(B)**

FIGURE 14: GEOMETRIC COMPARISON OF 42 CM LABORATORY TIRE (A) TO INDUSTRIAL HAULAGE TIRE (B)

A second geometric consideration is the ratio of the width of the tire compared to its total diameter. In haulage tires, this is 0.36:1 for example, for a Michelin 55/80R63 tire. With this in mind, priority was given to choosing wider specimen tires for the experiment. The width to diameter ratio of the specimen tire is 0.39:1. Of available tire models of a similar diameter, the model chosen for the experiments had the closest width to diameter and hub to diameter ratios to industrial models.

At an inflation pressure of 310 kPa, the maximum load of the laboratory tire is 280 kg, 80 kg greater than the maximum load that can be applied using the mill table. Hence, an undamaged specimen can be safely used in the testing apparatus.

4.2.3.4 Tire Construction

Tire selection is limited to commercially available models, and as such, not all parameters can be controlled in the specimen tire for perfect similarity to a haulage tire. Prioritizing geometry, trailer tires were chosen over other commercial tires with smaller and less visible sidewalls.

Commercially available trailer tires, possessing similar geometry to haulage tires, were bias ply instead of radial ply. In a radial tire, the cords are oriented perpendicular to the direction of loading, and belts overlap. By comparison, a bias tire features belts which cross each other and are not perpendicular to the loading direction. Generally, radial tires exhibit more flexion in the sidewall, while bias tires exhibit greater flexion in the tread. Another difference affecting flexibility is the cord material, which is steel in haulage tires but nylon cord in the specimen tire. These differences can be minimized by controlling the tire deformation.

4.2.3.5 Tire Surface Pattern

A high-contrast surface pattern is required to perform an accurate correlation on the tire images. A randomized pattern was spray-painted in white paint on the tire surface, shown in Figure 15. Spray paint can be applied quickly, provides a randomized pattern, and could be implemented in a field setting. The diameters of the spots in Figure 15 range from 0.1 mm to 1 mm, corresponding to 1-10 pixels in the image. Larger spots exceeding these diameters can be removed manually to improve the consistency of the spot size.

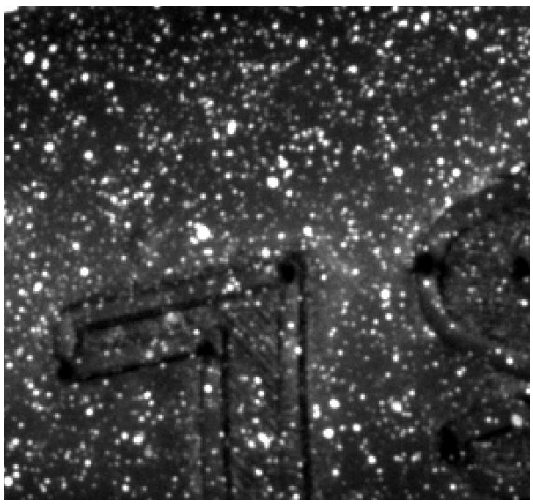

FIGURE 15: HIGH-CONTRAST, RANDOMIZED SPECKLE PATTERN APPLIED TO TIRE SURFACE

4.2.4 Justification of Software Selection for Experiment

A commercial software package (DaVis 8.0, LaVision GmbH) was used for manipulation and processing of data. A correlation process compares sets of images to return displacements, velocities, strains, or other information depending on the nature of the experiment. Both 2D and 3D displacement vectors can be calculated from image data, and transformed to strain measurements.

Pre-processing operations are available in DaVis to enhance the image contrast and quality before correlation. A non-linear sliding average filter was used to pre-process experimental data to remove background information and increase the contrast between the spots and the tire. A geometric mask was used to reduce the size of the processed area to include only regions of interest. Post-processing vector operations are also provided, for example, subtracting bulk motion from a vector field, or removing outlying vectors that exceed a threshold of variance from their neighbours.

Another advantageous feature provided by the software is the ability to perform multi-grid correlations, where displacement calculated over larger windows is used to provide an offset for smaller regions. This allows for a wider range of deformation to be quantified in an image compared to using a single window size. The correlation process can also be iterated to further refine the calculated displacements [44]. Multi-grid and iterative processing increases the spatial resolution of displacement measurements [50].

Three conferences, or PIV challenges, have taken place to assess the performance of PIV and particle tracking methods. For obtaining displacement and strain measurements, LaVision's DaVis software compares favourably to other available methods [48][49][50].

4.3 Preliminary Work

A simple study was undertaken to develop the procedure for obtaining tire displacement and strain fields for future experiments. The goal was to ensure that deformation due to simple damage applied to a loaded tire could be observed using the DIC analysis package before proceeding to more complex damage mechanisms and dynamic loading. Since outer truck tires frequently experience more damage than interior ones, due to impacts and environmental exposure [2][23], these investigations focus on monitoring the sidewall of a tire as opposed to the tread. A general procedure was developed for conducting experiments.

To begin, simple, thin cuts were made on the tire sidewall perpendicular and parallel to the direction of loading. Images were recorded before and after damaging the tire, with a 140 kg load applying stress to the tire. This loading procedure allows a focus on observing deformation cause solely by the presence of damage, without vectors due to the gross displacement of the tire. For a thin cut, the additional outward (z) displacement due to the cut was anticipated to be small compared to the x and y displacement. A single-camera can be used to perform a 2D analysis, which is a necessary precursor to making full 3D measurements.

A single camera aligned with the central tire axis was used to record images for a 2-dimensional strain and displacement analysis. The tire was kept at the recommended inflation pressure of 165 kPa to minimize sidewall bulging. Camera calibration images were recorded immediately prior to the experiment, controlling the position, shutter speed, focus, and F-stop.

4.3.1 General Procedure

The desired result of any given test is a set of images from which the displacement, and/or strain of the tire can be measured. A typical procedure for obtaining images of the tire can be described as such:

1. Install tire in mill
2. Measure tire pressure
3. Secure camera(s) facing the tire, at the desired camera angle from the central tire axis
4. Adjust lens adapter(s) to align the focal planes of camera(s)
5. Focus camera(s) and choose exposure time and aperture
6. Illuminate tire surface
7. Install calibration plate
8. Record calibration images
9. Remove calibration plate
10. Apply load to tire
11. Measure tire load at reference orientation
12. Record vertical position of mill table and load
13. Record images
14. Reposition tire and repeat as required

The procedure is designed to apply known and repeatable loading to the tire, and to obtain high-contrast, focused, and scaled images of the tire.

4.3.2 Displacement of Radial Sidewall Cut

Using a thin sharp blade, a cut measuring 15 mm long and 3 mm deep was made on the tire surface, on a line extending radially from the center of the tire to the surface of the mill table. The location and orientation of the cut are shown in Figure 16. Load was applied vertically to the tire through the mill table.

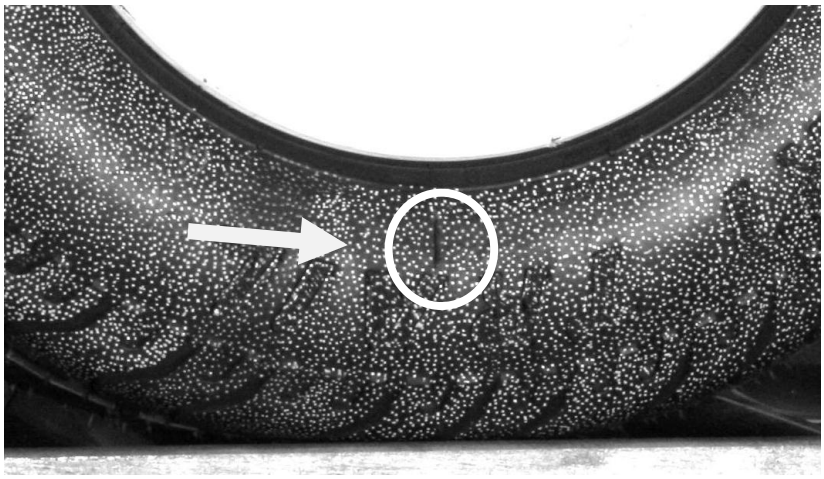

FIGURE 16: POSITION AND ORIENTATION OF RADIAL CUT

Figure 17 shows the tire surface before and after the radial cut was created, while a 140 kg load was applied to the tire. The image scale is 5 pixels/mm, and the image represents an area 45 mm wide by 40 mm tall. Visually, it was observed that the cut caused stretching of the tire in the horizontal (*x*) direction. Since the edges of the cut are no longer able to support the stress in the tire carcass, the surrounding material experiences a greater deformation.

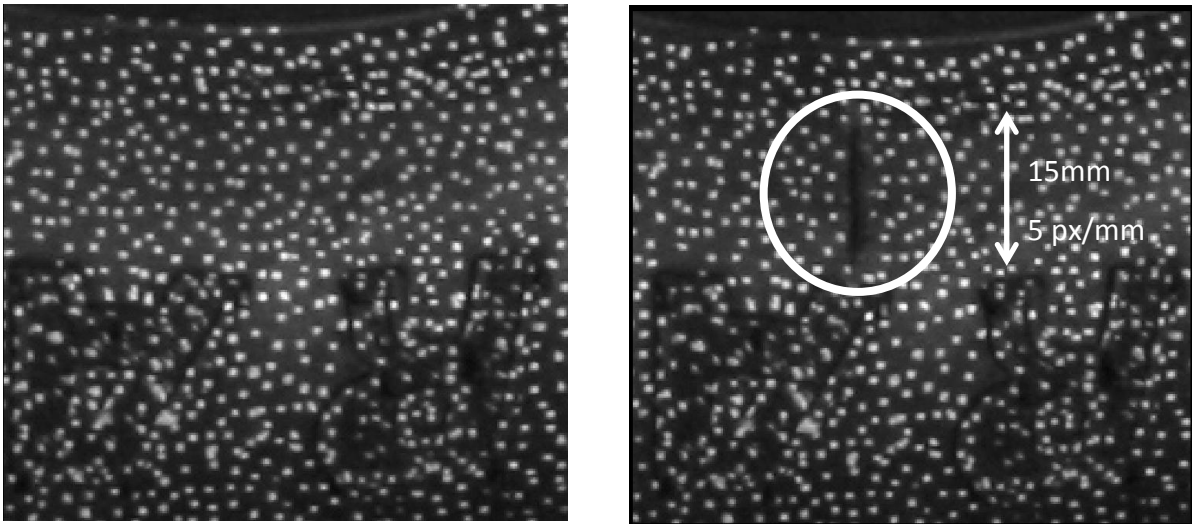

(A) **(B)**

FIGURE 17: TEST TIRE BEFORE (A) AND AFTER (B) CUT

The deformation of the cut was calculated using DIC software. First, images were corrected to provide scale and remove lens distortions and other imperfections. Then, displacement was obtained using 2D correlation with 16 by 16 pixel interrogation windows. Figure 18 shows the deformation of the tire caused by the introduction of the fault, at the same scale and over the same region as Figure 17. As expected, the areas immediately surrounding the fault are shown to stretch away from the cut in the *x*-direction under load. In this figure, red areas are displacing to the right, blue areas are displacing to the left, and green areas have zero horizontal displacement. The deformation surrounding the cut agrees with predictions and visual observations that the cut would cause horizontal stretching on the tire surface.

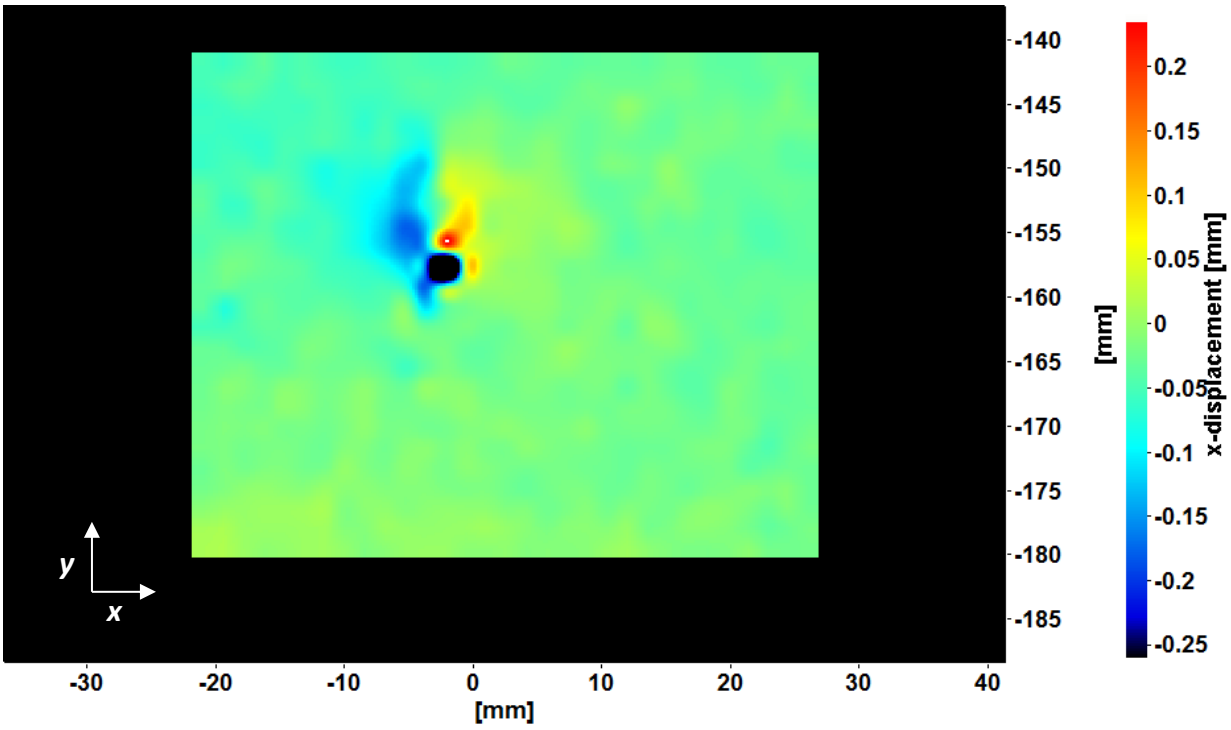

FIGURE 18: HORIZONTAL DISPLACEMENT CAUSED BY INTRODUCTION OF RADIAL CUT IN TIRE

4.3.3 Displacement of Tangential Cut

The deformation calculation process was repeated for a cut 20 mm long by 3 mm deep made perpendicular to the direction of the radial cut, on an undamaged section of the tire. This displacement is shown in Figure 19. Vector direction and magnitude, which has been magnified for clarity, is shown by the black arrows. Contrary to the radial cut, the tangential cut caused significant displacement in the vertical direction, parallel to the direction of loading. Again, the displacement field highlights stretching on the tire surface when the damage is applied, which corresponds with visual observations.

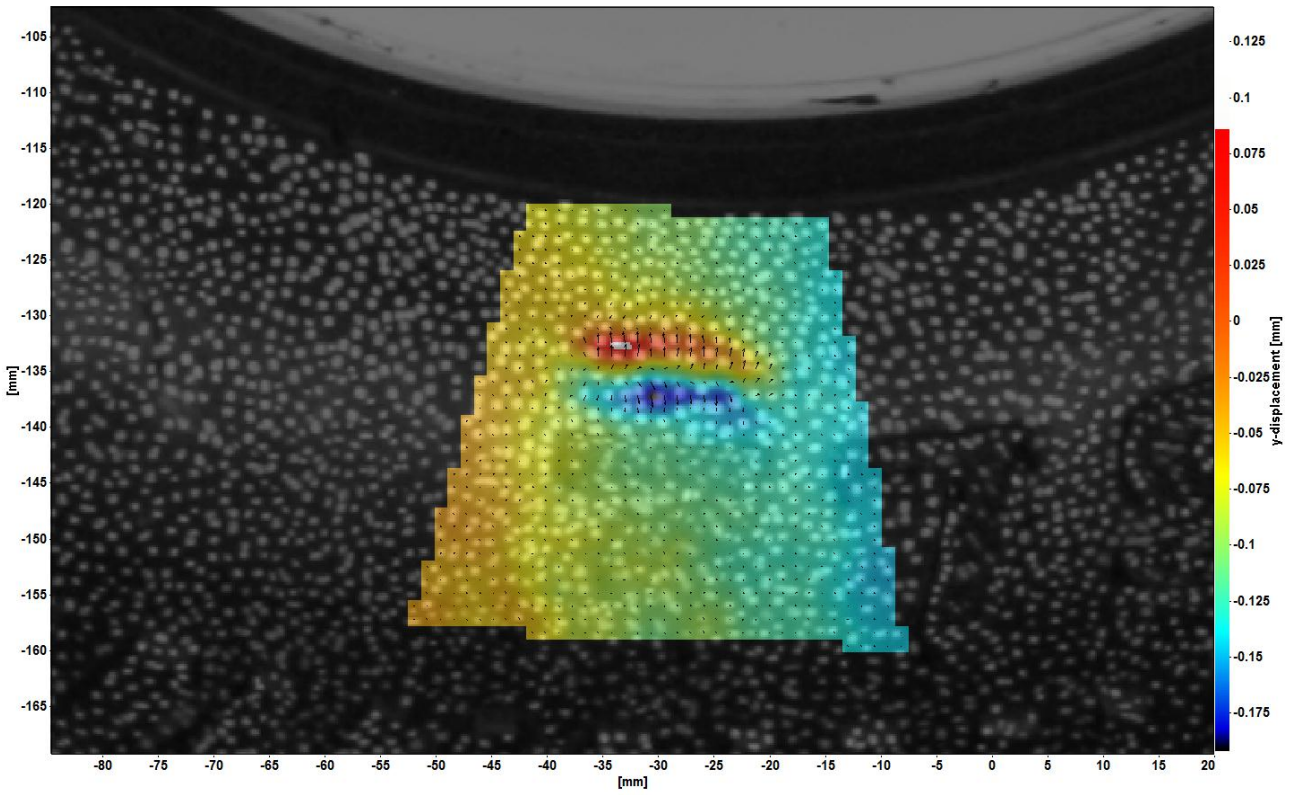

FIGURE 19: VERTICAL DISPLACEMENT OF SURFACE DUE TO TANGENTIAL CUT

4.3.4 Improvements to System and Procedure

The initial results appear promising and show that there is potential to obtain displacement measurements from the tire. There are changes that can be implemented in order to improve the data quality as well as the practicality of this technique. It can be seen in Figure 20 that the size of interrogation window used, shown in red, contained fewer than the number of dots recommended to minimize correlation error, which should be 4-5. There are two remedies for this issue, to increase the size of the cut relative to that of the dots, so that the size of window required to "find" the cut increases, and a larger interrogation window can be used, or to decrease the size of the dots in the speckle pattern. Both of these changes were implemented for subsequent experiments to improve the accuracy and resolution of the measured displacements. Additionally, the cameras were positioned closer to the tire to increase the average image scale from 5 px/mm to 8 px/mm so that smaller dots could be registered by the sensor.

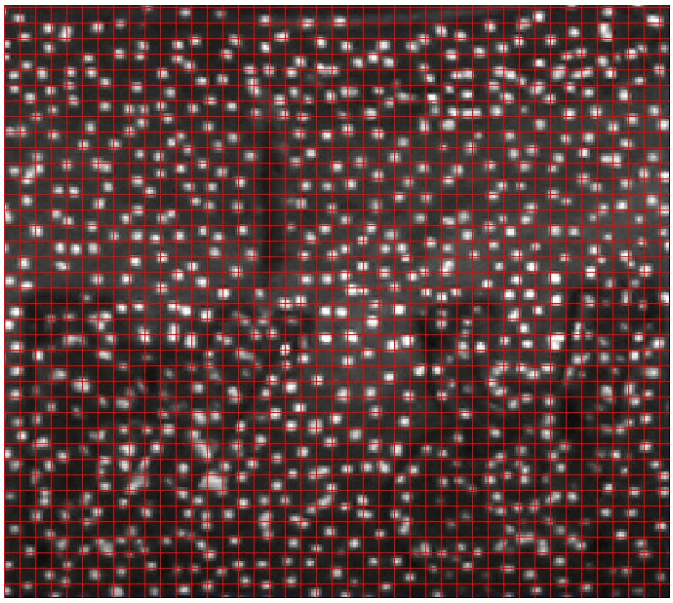

FIGURE 20: 16X16 GRID, IN RED, SHOWN ON TIRE AT 5 PX/MM SCALE

The size of the dots limits the physical resolution of the method. Resolution is a function of the distance from the camera to the tire, determining the corresponding physical diameter of an image pixel, and is also a function of the size of the dots. Ideally, a dot should have a diameter of 2 pixels in the image to maximize the resolution of the method without sacrificing the probability of detecting the point [45].

In this case, the size of the dots, which was typically 0.4 mm to 1.2 mm, corresponded to a 3-9 pixel diameter in the image. A new pattern, with dots between 0.1 and 1.0 mm, combined with a change in camera distance, results in dots from 1 to 10 pixels in diameter. The two patterns, old (A) and new (B) are compared in Figure 21 over sample 40x45 mm regions. The background has been filtered from image B to better show the finer dot pattern. At a given camera distance, smaller interrogation windows can be used, resulting in a finer resolution for measurements. If the effects of tire damage are localized, a finer resolution for measurements could improve the probability of measuring changes due to tire damage.

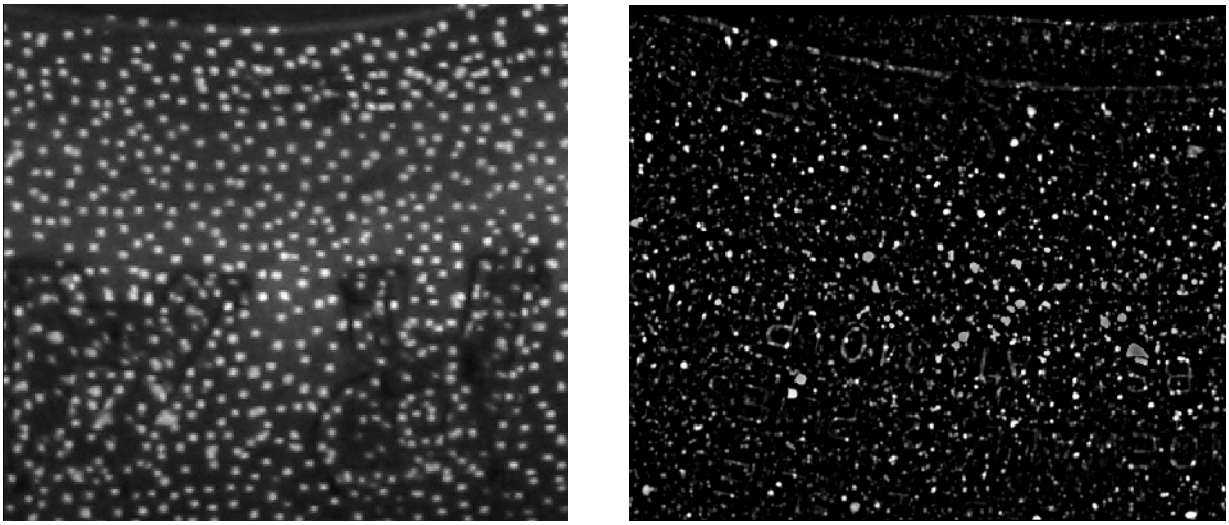

(A) **(B)**

FIGURE 21: OLD (A) SPOT PATTERN COMPARED TO NEW (B) SPOT PATTERN

A second concern with the preliminary tests was the practicality of implementing this data gathering method on site. In the laboratory, it is known when damage occurs to the tire, which is not always true on site. In lieu, a tire should be compared to itself during a very short time frame, over minutes, as it is loaded and unloaded, instead of as it is gradually damaged. In subsequent experiments, strain will be calculated from progressive loading of the tire.

Finally, the preliminary work ignores bulging of the tire, which adds an out-of-plane component to the displacement and strain fields on the tire surface. The strain analysis is expanded to include three-dimensional measurements of the tire, to determine how important out-of-plane deformation is for some fault types.

Chapter 5: Visibility of Tire Damage : Results

Equipment was developed to conduct experiments for optical detection of tire damage. The results of preliminary testing were used to improve the experimental procedure and equipment. This chapter presents the results of the investigation into damage visibility from optical displacement and strain measurements on a laboratory-scale tire. The results include damage visibility from cases with both stationary and rotating tires. A set of criteria for damage visibility are defined and used to evaluate the feasibility of using optical strain measurements for damage detection, as well as to determine considerations for an eventual field application of this work.

5.1 Stationary Loading of Sidewall Cuts

Implementing the improvements suggested by the preliminary work, such as a finer dot pattern, the behaviour of damaged tire regions under loading was investigated. For these experiments, images were recorded as the tire was loaded, and analyzed to obtain strain and displacement. The damage was held stationary with respect to the load to eliminate vectors arising due to bulk movement of the tire. Different indicators, such as horizontal, vertical, and out-of-plane displacement, as well as horizontal and vertical strain, were calculated over the tire surface to determine which measurements could be used to display and understand the behaviour of damaged regions.

5.1.1 Creating Artificial Tire Damage

To provide controlled cases for study, artificial tire damage was created on both the internal and external tire surfaces using a grinding tool. The cut was enlarged to increase the effects of the damage, reducing the resolution required to measure changes in the displacement or strain required to detect damage. Shown in Figure 22, an external radial cut measuring 35 mm long by 6.5 mm wide and up to 2.5 mm deep was made on the surface of the tire to simulate damage.

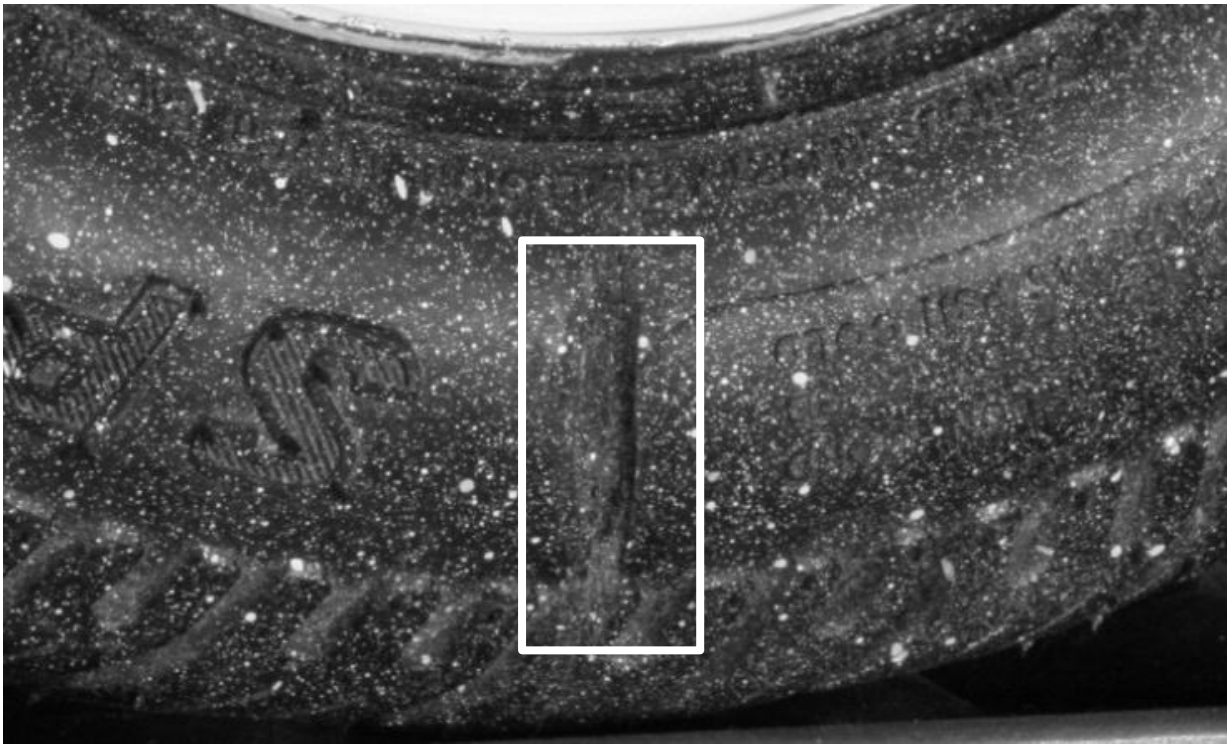

FIGURE 22: EXTERNAL RADIAL CUT ON OUTER TIRE SURFACE

Not all types of tire damage are externally visible. Internal delamination or belt separation can cause increased friction within a tire, decreasing its useful life. In many cases, there is no noticeable loss of pressure in the tire when internal damage occurs [4]. To simulate the effects of internal damage, a 2.5 cm by 7 cm strip of the inside wall of a tire was removed with a hand grinder, to a depth of approximately 2 mm. An internal view of this cut is shown in Figure 23, while its external position is indicated in Figure 24. Also shown, in blue, is the area of the tire over which the 3D displacement and strain was calculated.

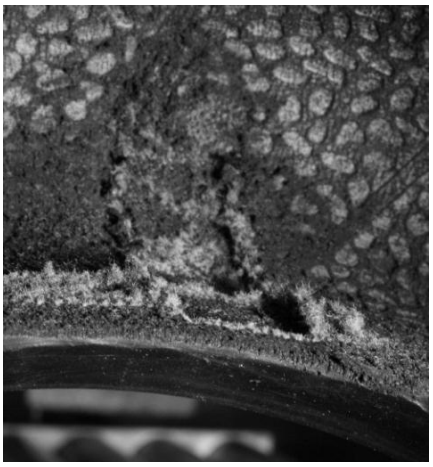

FIGURE 23: INTERNAL VIEW OF INTERNAL TIRE CUT

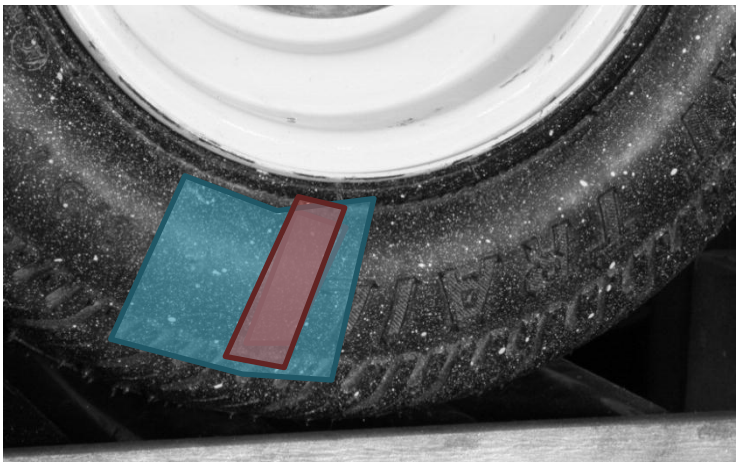

FIGURE 24: EXTERIOR OF TIRE HIGHLIGHTING LOCATION OF INTERNAL DAMAGE AND REGION OF INTEREST

5.1.2 Procedure: Loading and Processing

Images were recorded as a 90 kg load was progressively applied to a damaged tire. Due to the severity of damage to the tire, pressure was reduced to 45 kPa for safety. Pressure reduction reduces the hazard of a tire depressurization in case of total failure of the damaged regions. It also caused a greater deformation in the tire for a given load. A two-dimensional displacement and strain analysis was performed to determine whether external damage could be detected from this sequence of images. Interrogation windows measuring 32 by 32 pixels were used for correlation, with a 50% overlap between windows, which reduces correlation error [51].

For internal damage, the analysis was expanded to three dimensions, and compared to a control region to observe the resultant changes in the strain and displacement fields. In both cases, two cameras at a 20 degree camera angle were used to record the images. This camera angle was chosen experimentally to improve the 3D surface reconstruction within the image correlation software. At angles greater than 30°, complete surface reconstruction was not always possible from a set of two tire images.

5.1.3 External Cut Under Stationary Loading

The strain and deformation of the external cut was calculated from images of the tire recorded as a 90 kg load was applied. The results are presented in Section 5.1.3.1.

5.1.3.1 Displacement and Strain Surrounding External Cut

Figure 25 shows the calculated displacement of the tire surface as load was applied to the tire, with the external damage positioned directly above the point of loading. The deformation is shown superimposed on the original images of the tire over a 10 cm wide by 7.5 cm tall area. In these images, blue indicates the least displacement, while red indicates the greatest displacement. Horizontally, the tire is spreading outwards from the point of loading, and by extension, the external cut. In the *y*-direction, a discontinuity in the displacement can be seen in the yellow region surrounding the cut.

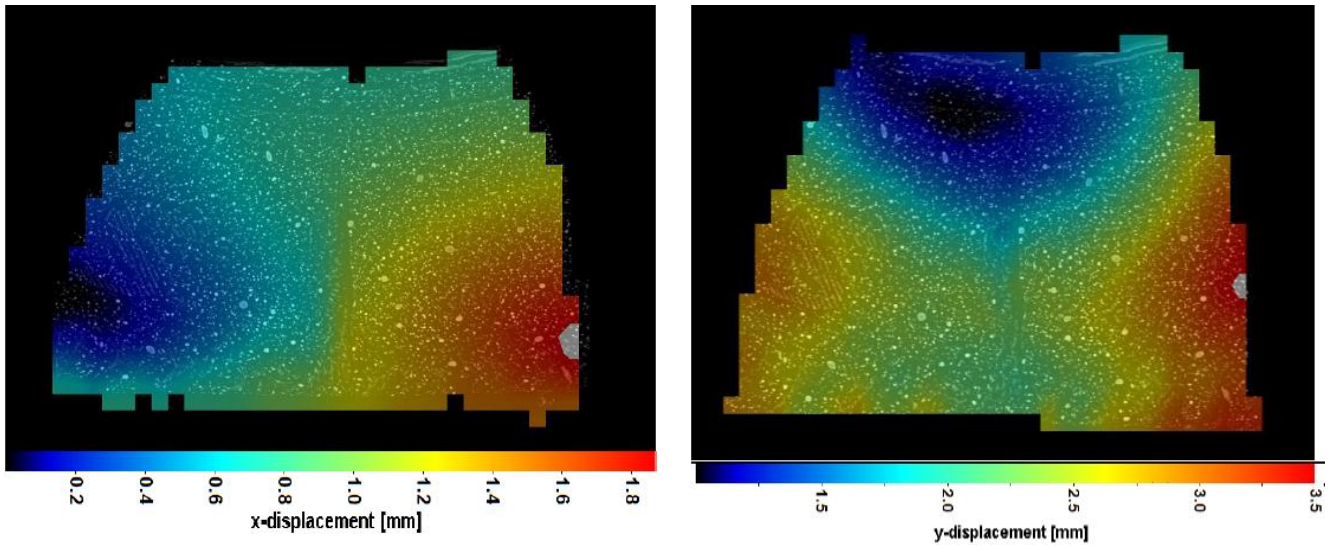

FIGURE 25: X (A) AND Y DISPLACEMENT SURROUNDING EXTERNAL CUT

The tire strain in the horizontal direction, *Exx*, was also calculated, and is presented in Figure 26. Although the effects of the cut on the horizontal displacement of the tire appear unclear, the horizontal strain has a value of 0.17 in the vicinity of the cut, compared to an average strain of -0.02 over the undamaged area. Strain values represent the change in length of a feature compared to its original length, and are as such, dimensionless.

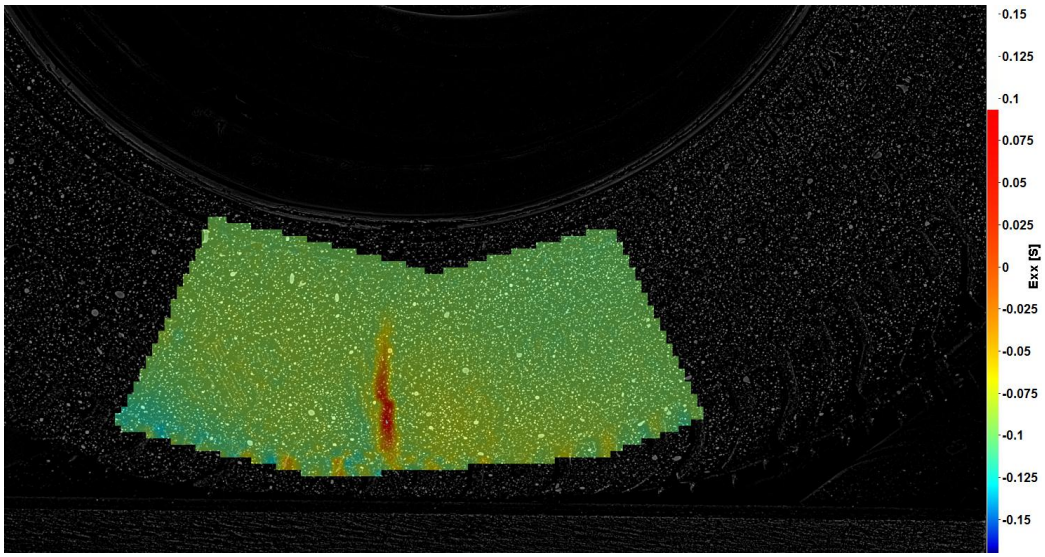

FIGURE 26: STRAIN, EXX, OF TIRE WITH RADIAL EXTERNAL CUT

At the same scale as *Exx*, the vertical strain, *Eyy*, for this case is given in Figure 27. It is important to note that compression is represented as having a negative value, in this case shown in blue, while tension is represented as having a positive value. In Figure 27, the bottom of the tire is undergoing significant compression in the vertical direction, reaching the greatest value present on the scale.

An interesting observation in Figure 27 is that while the strains near the rim and tread of the tire are compressive, the strain in the mid-sidewall is tensile. Upon first glance, this could seem counterintuitive, since it is known that the tire is being compressed. However, with the bulging of the sidewall, it is possible for the middle region of the sidewall to be in tension while it bulges out, while the tread and rim are in compression. Moser et al. (2010) obtain similar results from DIC measurements, showing compressive radial strain under load near the tire rim and tread, and tensile strain in the middle, which also agrees with their FE model predictions.

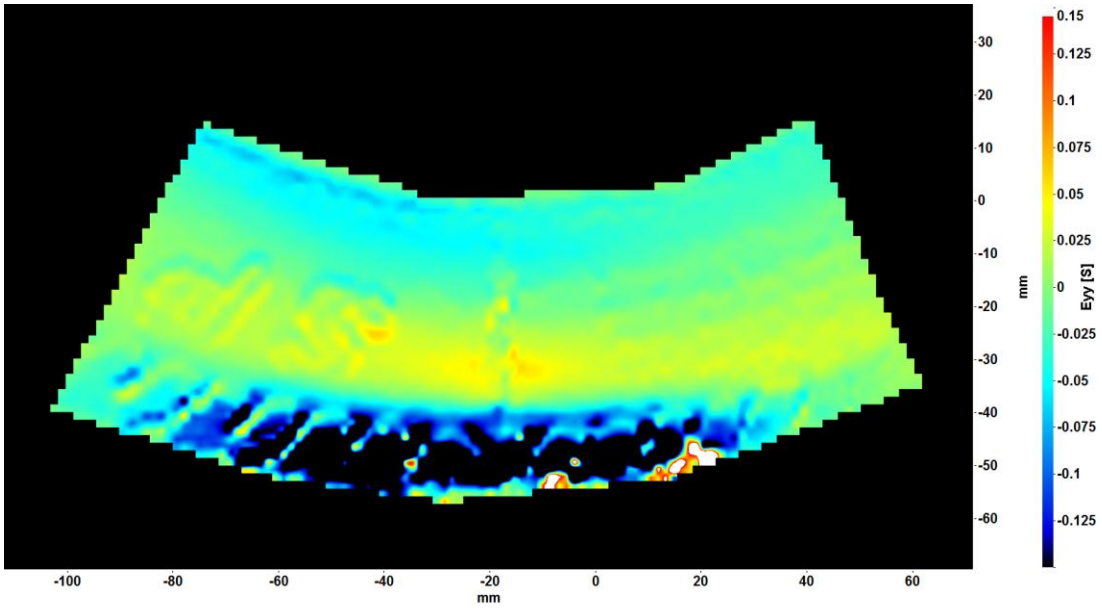

FIGURE 27: VERTICAL STRAIN EYY AT COMPARABLE SCALE TO EXX

When strain results are presented visually, scaling of the results is essential to avoid obscuring or misrepresenting data. In this case, it happens that the vertical strain due to the loading is much greater than the horizontal strain, which makes sense, since the load is applied vertically to the bottom of the tire.

When the same image from Figure 27 is re-scaled, the range now includes the absolute minimum and maximum calculated strain values, shown in Figure 28. Compared to the effects of the loading in the horizontal direction, the vertical compressive effect of the load is much greater, as would be anticipated, compressing the bottom of the tire to a strain of up to -0.4, or 40%. Noticeably, the tire damage cannot be distinguished from this image as well as it was in the horizontal direction. Most probably, the magnitude of the vertical strain due to the cut is much lower than the vertical strain due to the loading, obscuring the visibility of the cut. This is examined in the next trial, which compares the behaviour of a damaged region of the tire under loading to that of an undamaged region.

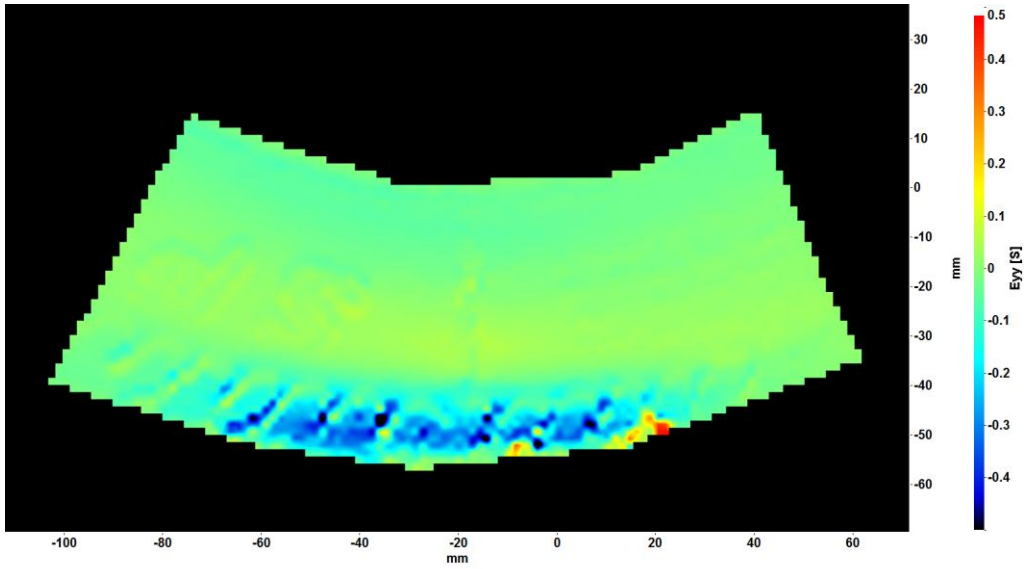

FIGURE 28: MIN/MAX SCALING OF EYY

What can be determined from this set of images is that strain provides a clearer view of tire damage for the external cut as opposed to the displacement field, in particular, the horizontal strain. The cut can be observed expanding horizontally, with a strain increase from -0.02, which is slightly compressive, to 0.17, which is tensile. In the vertical direction, the effect of the cut on the strain field is negligible, likely due to the thinness of the cut and the relative magnitude of the tire deformation due to loading. In both directions, the grooves surrounding the tire were visible due to changes in the calculated strain, which could correspond to actual physical behaviour of the tire, given the depth of the grooves, or could be due to processing artefacts. These areas will be excluded from future tests so that only the areas of the tire sidewall with a smooth surface and consistent thickness will be examined.

Given the position of the cut, perpendicular to the loading, it is unclear whether the displacement in the horizontal direction indicates any damage or is simply the tire spreading outwards in response to loading. A set of images of an undamaged tire region is used in the next trial to resolve this ambiguity. The effects of internal damage are also investigated, and the analysis is expanded to include out-of-plane deformation.

5.1.4 Internal Damage Under Stationary Loading

The deformation of the internal cut was calculated from images of the tire recorded as a 90 kg load was applied, for both a damaged and undamaged region of the tire. 3D displacement vectors were calculated over a region of interest, described in Section 5.1.4.1, using a reconstructed map of the tire surface. The results are presented in Section 5.1.4.2.

5.1.4.1 Area of Interest

It was predicted that a thinning of the tire wall would result in greater out-of-plane deformation in the vicinity of the damage than a narrow exterior cut. The experimental procedure was modified to obtain three-dimensional measurements by adding a camera to the system and calculating a reference surface in the software. While two-dimensional strain and displacement can be calculated from a single camera, two or more cameras are necessary to resolve strain and displacement information in three dimensions [52]. To obtain these measurements, the software must first create a 3D surface as a reference for subsequent deformations.

Re-building the entire surface of the tire with high spatial precision is a computationally expensive process, so a smaller region of interest was examined. The region of interest was chosen to explore the effects of the damage over a distance roughly twice the diameter of the cut. The area to the right of the cut, in this case, was not examined, as preliminary investigation showed a much greater deformation in that region that could obscure the changes in strain surrounding the cut. Figure 29 shows the area of interest that was examined as the tire was loaded, with respect to the applied load, as well as the co-ordinate system used in the analysis.

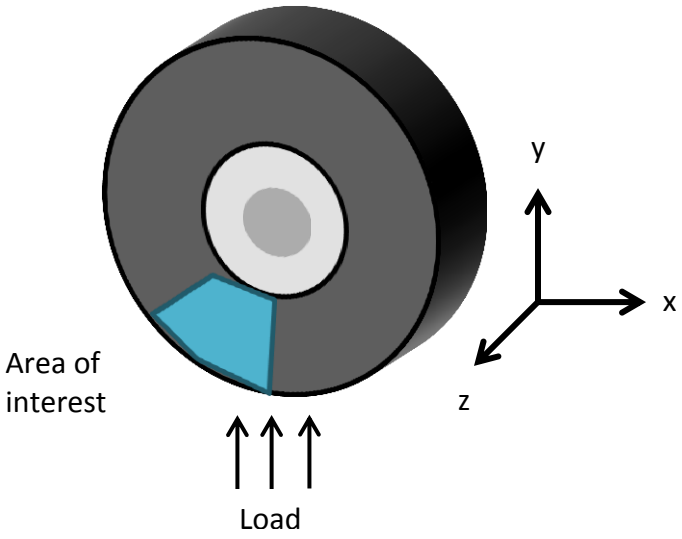

FIGURE 29: REGION OF INTEREST FOR 3D MEASUREMENTS

The area of interest examined in each case is in an identical position and orientation with respect to the load, in order to properly compare the undamaged and damaged tire sections.

5.1.4.2 Displacement and Strain Surrounding Internal Damage

A consistent scaling is used for each pair to visually highlight the changes arising from the internal damage. The images are scaled so that the lowest relative value is coloured in blue, progressing to red for the greatest relative value. Each 3D surface measures 10 by 5 cm.

Shown in Figure 30, the damaged tire exhibits a greater overall deformation of the surface, and some irregularity in the vicinity of the damage, when compared to the undamaged region. In the *x*-direction, roughly perpendicular to the direction of loading, the displacement is greater closer to the point of load application. Three sets of displacement images are presented, for the horizontal, vertical, and out-of-plane deformation of the undamaged tire area, on the left, and the damaged area, on the right. In each image, the internal cut is positioned slightly to the right of center, and stretches all the way from the top to the bottom of the region of interest.

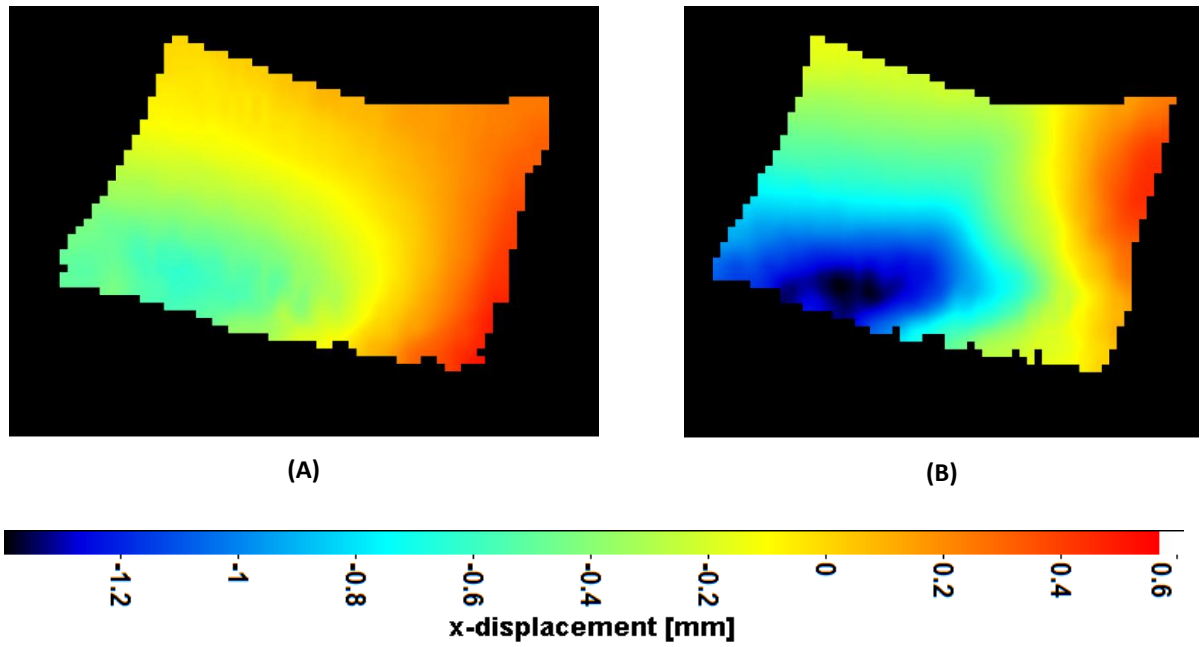

FIGURE 30: X-DISPLACEMENT IN UNDAMAGED (A) AND DAMAGED (B) TIRE AREAS

The loading was expected to cause increased radial strain near the treads, decreasing with proximity to the hub [5]. This agrees with the displacement shown in Figure 31A, with the *y*-direction corresponding roughly to the radial co-ordinates of the tire. As with the external cut, there is a discontinuity in the displacement field near the internal cut, shown in Figure 31B.

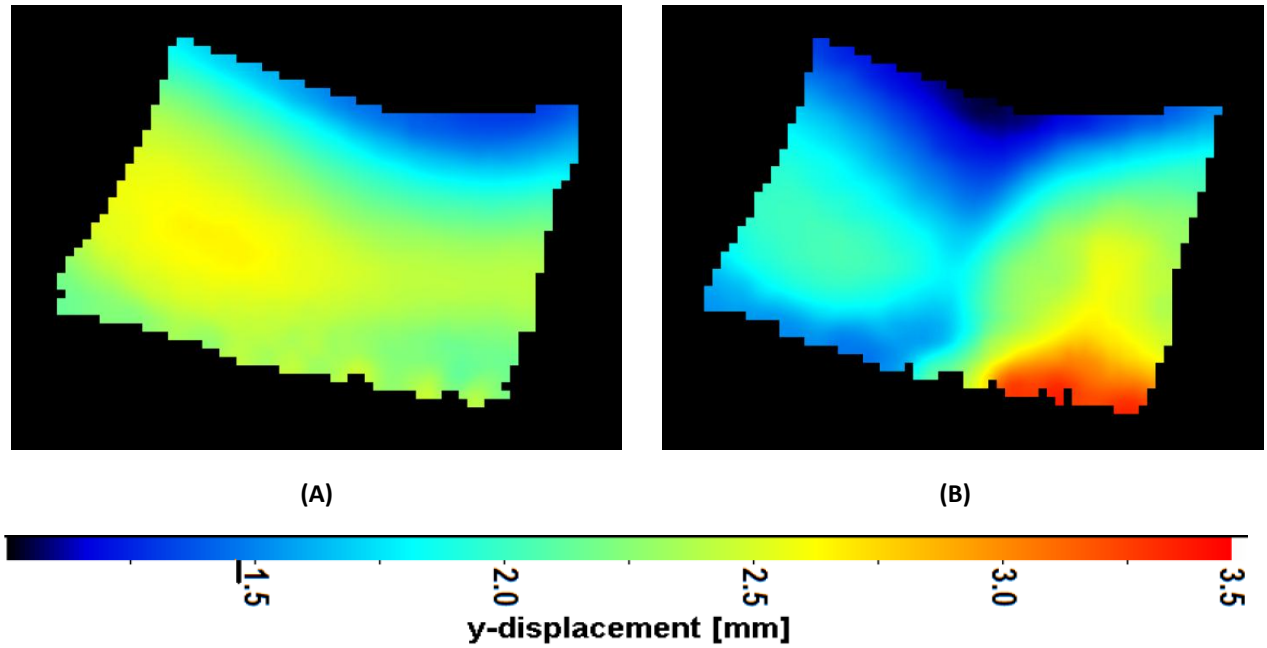

FIGURE 31: Y-DISPLACEMENT IN UNDAMAGED (A) AND DAMAGED (B) TIRE AREAS

It was anticipated that increased out-of-plane deformation, shown in Figure 32, would be visible near the internal cut because of its reduced ability to withstand the pressure pushing from within the tire. However, as seen in the right side of Figure 32B, the out-of-plane displacement is only slightly increased, by a factor of 1.2, over the internal cut. A possible explanation for this is the tire pressure, which was underinflated at 45 kPa to exaggerate the deformation, compared to a suggested inflation pressure of 200 kPa. Some striations are also visible in the image, which could be due to the loading distribution in the tire between the cords and the rubber.

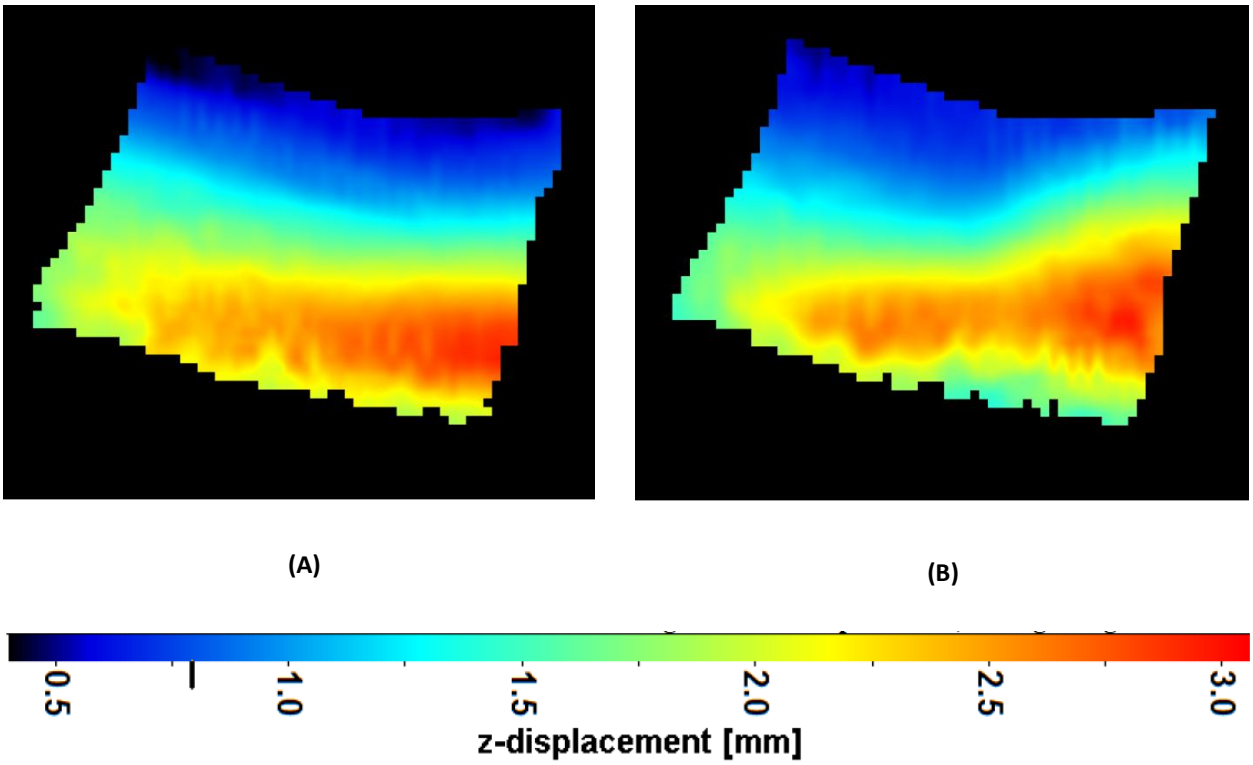

FIGURE 32: Z-DISPLACEMENT IN UNDAMAGED (A) AND DAMAGED (B) TIRE AREA

The strain in the *x*-direction was calculated and is shown in Figure 33. Similarly to the external cut, the internal cut is sharply highlighted in image B, with an increase from -0.01 strain (compressive) in the undamaged area, to 0.06, or 6%, over the internal damage. There is a change from slight compression of the surface in the horizontal direction, to expansion in the area of the cut.

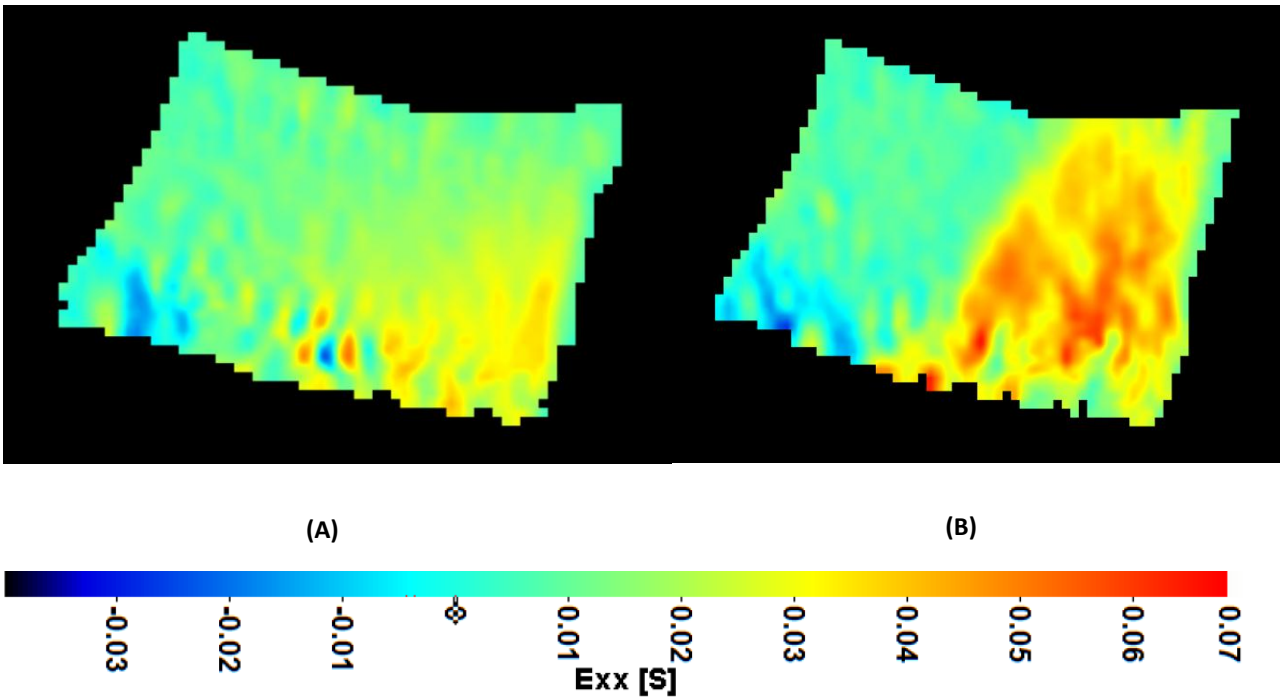

FIGURE 33: HORIZONTAL STRAIN, EXX, IN UNDAMAGED (A) AND DAMAGED (B) TIRE REGION

Vertical strain, *Eyy*, was calculated and is presented in Figure 34. As opposed to the strain in the horizontal direction, the internal damage is causing compression in the vertical direction, instead of expansion. This can be seen in Figure 34B, where the dark blue region over the damaged area indicates compression of up to 0.1, or 10%, in the vertical direction. It can also be observed that while the horizontal strain did not vary significantly with vertical position on the tire, the vertical strain varies with distance from the hub even in the undamaged tire. This suggests, along with the results from the external cut, that typical radial strain in the tire varies with radial position, while circumferential strains are more uniform.

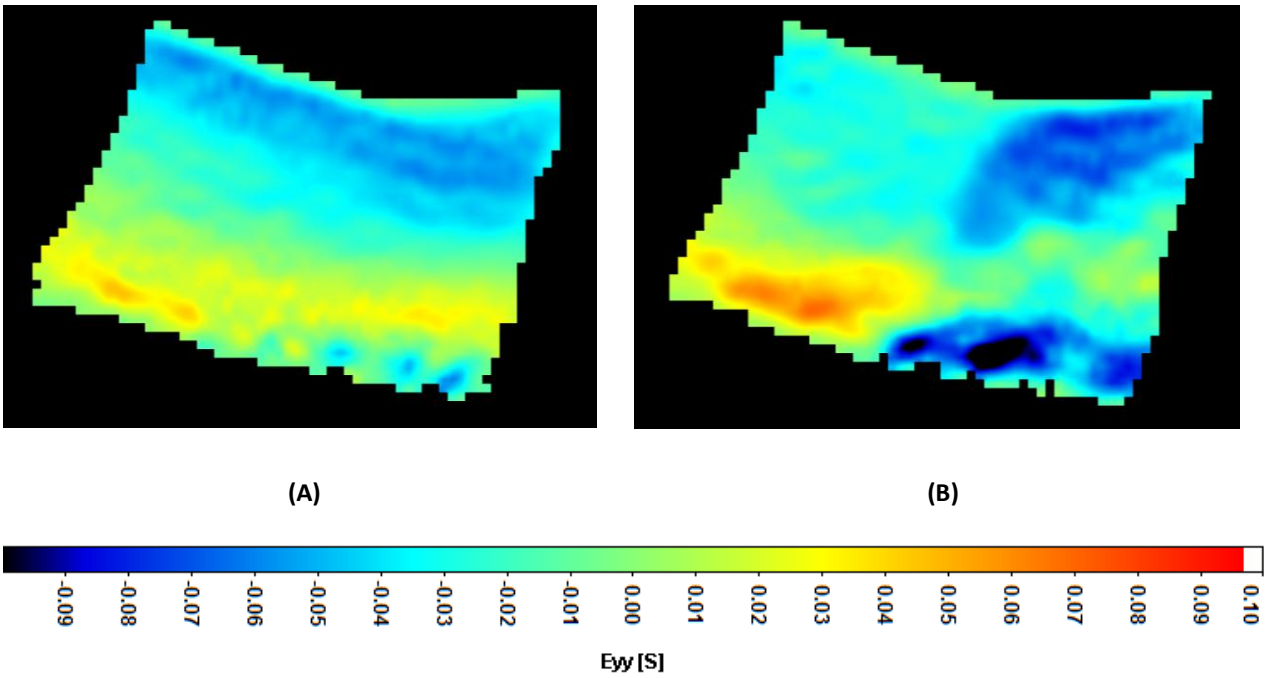

FIGURE 34: VERTICAL STRAIN, EYY, IN UNDAMAGED (A) AND DAMAGED (B) TIRE REGIONS

It was not possible to calculate Ezz, the out of plane strain, in the sofware, which will be explored in future work. Generally, the strain fields visually indicate damage more clearly than the displacements. Overall, the images show that the internal damage has a clear effect on the surface strain field of the tire, causing sharp changes in both strain direction and magnitude. This is encouraging for future studies using this method, since it can be used to detect damage that is invisible to the unaided eye and does not affect pressure readings.

Compared to the external cut, the internal damage resulted in greater compression in the vertical direction, similar to the magnitude of the tensile strain in the horizontal direction. The dominant strain for the external cut was tensile, while the magnitude of the compressive horizontal strain and tensile vertical strain for the internal damage was roughly equal. Describing the strain in terms of horizontal and vertical components was sufficient for this analysis, but is less meaningful as the position and orientation of damage is altered. This is investigated further in the next section, Area of Damage Visibility, which will analyze the condition of the tire using the maximum and minimum principal strains.

5.2 Area of Damage Visibility

According to Chow (1981), sidewall damage may affect surface strain up to 90° from the contact patch, or point of load application, on the tire [28]. Damage visibility is an important concern for both laboratory and site operations, affecting the frequency at which images must be recorded to detect damage. Depending on the visibility of the damage, it could be necessary to capture images after every degree of rotation in the tire, or it could be sufficient to capture images after every 30°. Visibility suggests which regions of the tire surface should be analyzed from each image for reducing the amount of processing required to capture the damage.

This section investigates the visibility of internal and external cuts at multiple orientations from the point of loading as a stationary load is applied. A set of criteria is developed for defining visibility and classifying regions and conditions with good damage visibility. Due to the rotation of the tire, the *x* and *y* strains are not sufficient to describe the behaviour surrounding the cuts, and new measures, the maximum and minimum principal strains, are introduced.

5.2.1 Maximum and Minimum Principal Strains

In previous experiments, with the fault in alignment with the load applied to the tire, an *xy* co-ordinate system was sufficient to analyze the tire strain. With a change in orientation, however, this co-ordinate system becomes less meaningful, since the stress in the tire is affected both by the location at which load is applied, and the orientation of the cut. The same can be said for using a polar co-ordinate system. Instead, the principal strains at each point are used to describe the strain field on the surface of the tire.

The principal strains, *Emax* and *Emin*, are simply the *Exx* and *Eyy* strains rotated to an orientation which produces the greatest and least strain, respectively, to describe the strain on the tire surface. *Emax* and *Emin* can be calculated from the formulas [44]:

$$Emax = \frac{Exx + Eyy}{2} + \sqrt{\left|\frac{(Exx - Eyy)^2}{4} + E'xy\right|} \qquad [5]$$

$$Emin = \frac{Exx + Eyy}{2} - \sqrt{\left|\frac{(Exx - Eyy)^2}{4} + E'xy\right|} \qquad [6]$$

where *E'xy* is the average shear strain, defined by:

$$E'xy = \frac{Exy + Eyx}{2} \qquad [7]$$

with *Exy* and *Eyx* representing the shear strain in the *xy* co-ordinate system.

A general comparison of the maximum and minimum strains for both the internal and external tire showed that overall, the internal damage was more evident when viewing the maximum strain, while the external damage was more evident when viewing the minimum surface strain. An explanation is that the external cut is more often in compression, which is conventionally given a negative value, whereas the internal damage causes bulging or expansion on the surface. Although it was earlier observed that the external cut was in tension, that was only in the horizontal direction at a single orientation, while this section observes the cut at multiple orientations. It is important to remember that a region can simultaneously be in compression in one direction and tension in another due to Poisson's effect. Figure 35 and Figure 36 show, circled, the resultant strain from both damage types rotated approximately 30° clockwise from the point of loading. A displacement of 12.7 mm, causing a change in radius of 15%, was applied to the bottom of the tire.

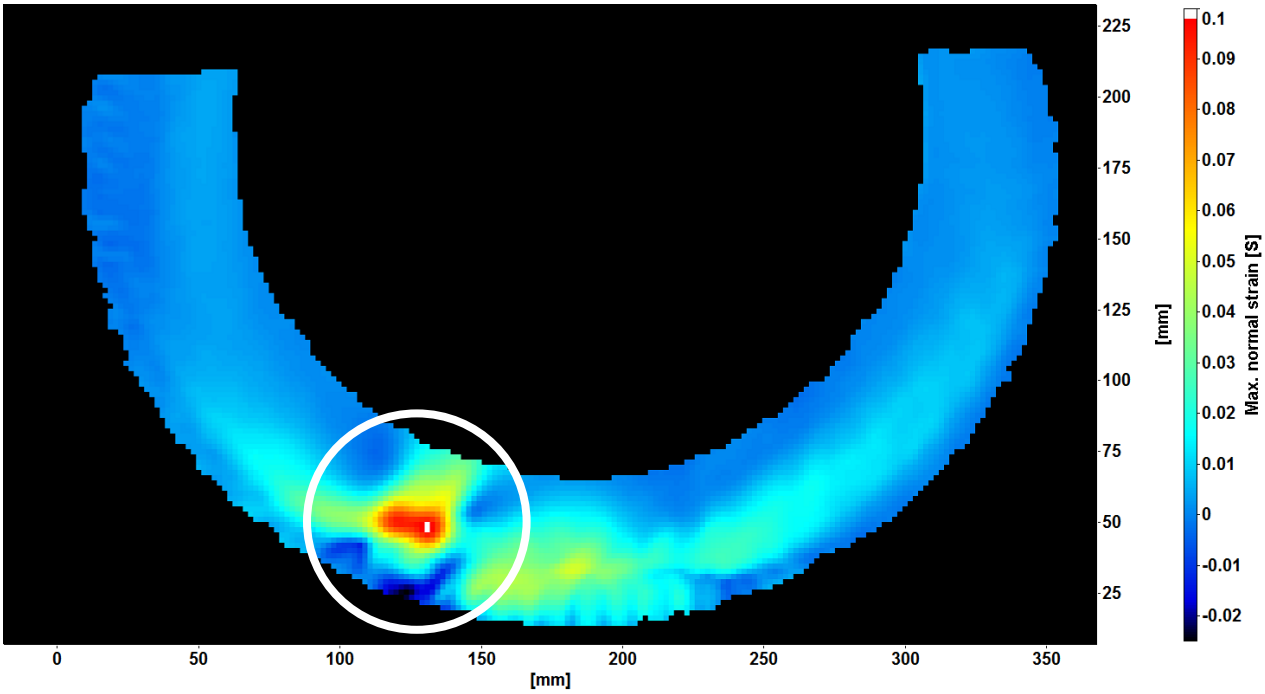

FIGURE 35: MAXIMUM TIRE SURFACE STRAIN WITH INTERNAL CUT ROTATED 30 DEGREES CLOCKWISE FROM POINT OF LOADING

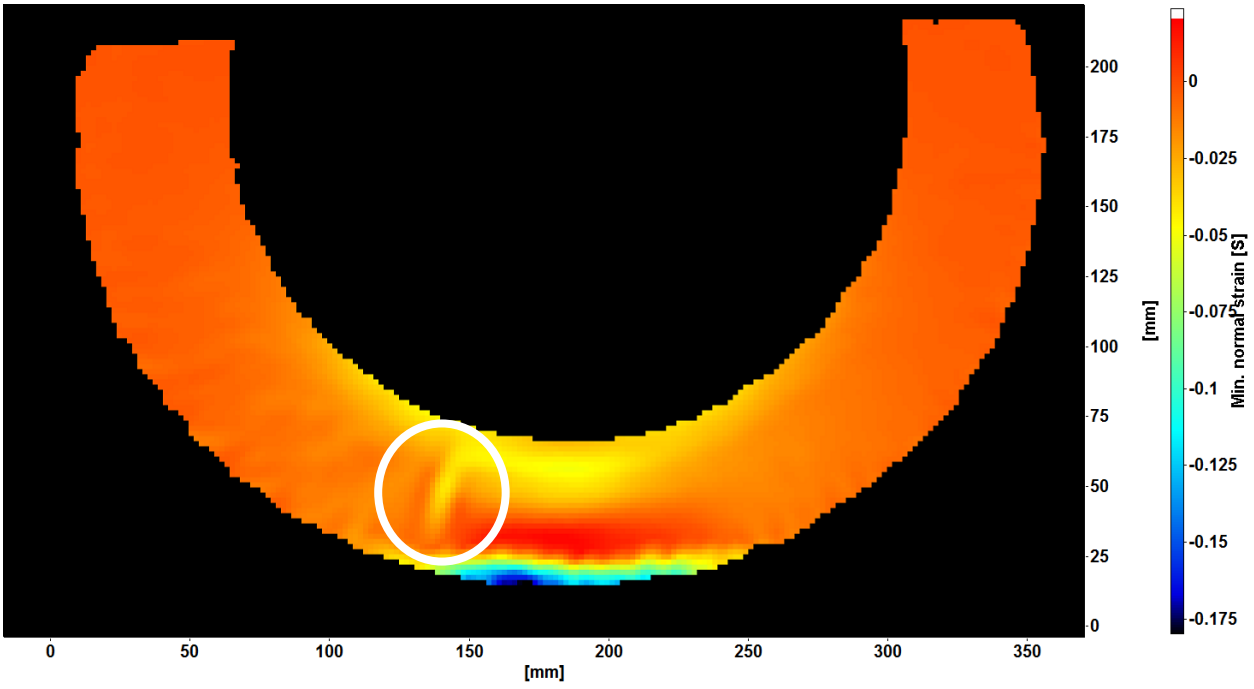

FIGURE 36: MINIMUM TIRE SURFACE STRAIN WITH EXTERNAL CUT ROTATED 30 DEGREES CLOCKWISE FROM POINT OF LOADING

5.2.2 Defining Damage Visibility

A metric is required to quantify the visibility of the tire damage. A noticeable effect of tire damage is that it can change both the direction and the magnitude of strain on the tire surface. Since an undamaged reference field is not always available, a simple way to search for tire damage is to compare the magnitude of strain in one region of the tire to its immediate neighbours. Both the relative magnitude of the damaged area compared to adjacent regions as well as the absolute change in strain influence visibility. Since there is a limit to the resolution of strain measurements, the absolute change in strain between the damaged and undamaged regions must exceed this threshold, even when the strain ratio is sufficiently large.

To determine the visibility of both the internal and external cut at various angles, the strain field was calculated with an applied displacement of 15%. Using *a priori* knowledge of the damaged location, two masks were applied to the strain fields, one containing the damaged region, and a second containing two similarly sized regions adjacent to the damaged sector, on either side. For the external cut, the average maximum strain, *Emax*, was calculated over these areas, while the minimum strain was calculated for the internal damage.

An example of masking is given in Figure 37 and Figure 38. Regions highlighted in blue are included in the mask, while regions outlined in blue are explicitly excluded. This is done to ensure that pixels counted as belonging to the damaged area are not also counted as belonging to the undamaged area. The first image shows the maximum principal strain for the internal cut prior to masking, and the second image shows the resulting areas that the strain is averaged over after masking. In this case, the mask is applied to the regions adjacent to the damage to determine the change in strain due to the damage.

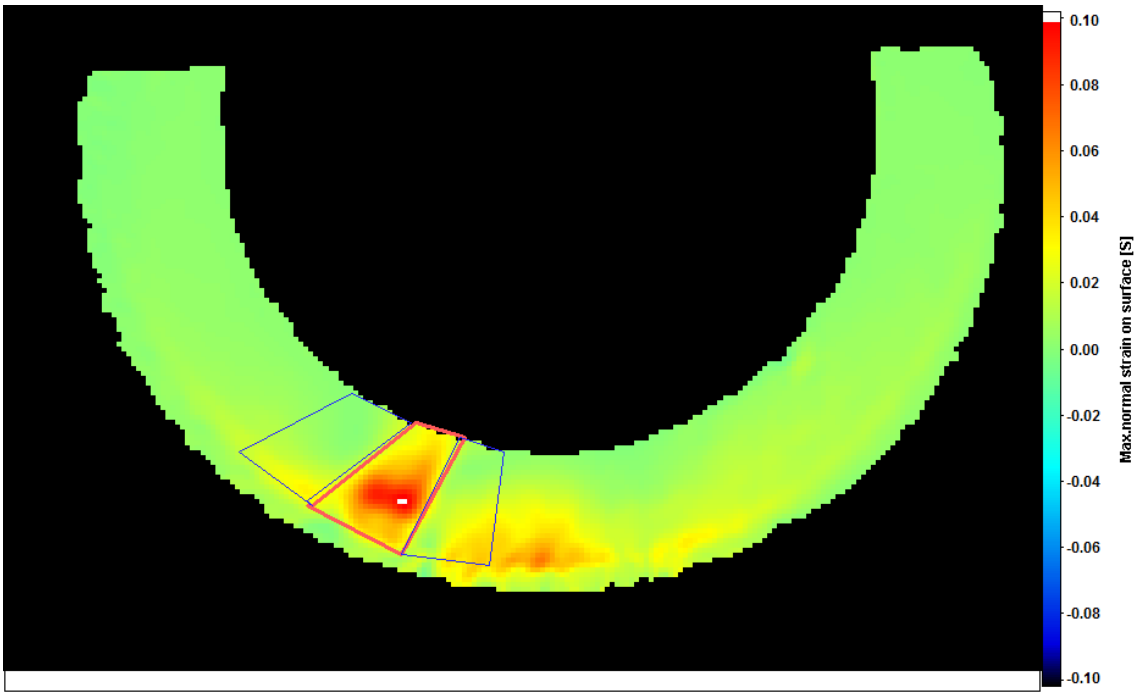

FIGURE 37: DEFINING A GEOMETRIC MASK ON TIRE SURFACE

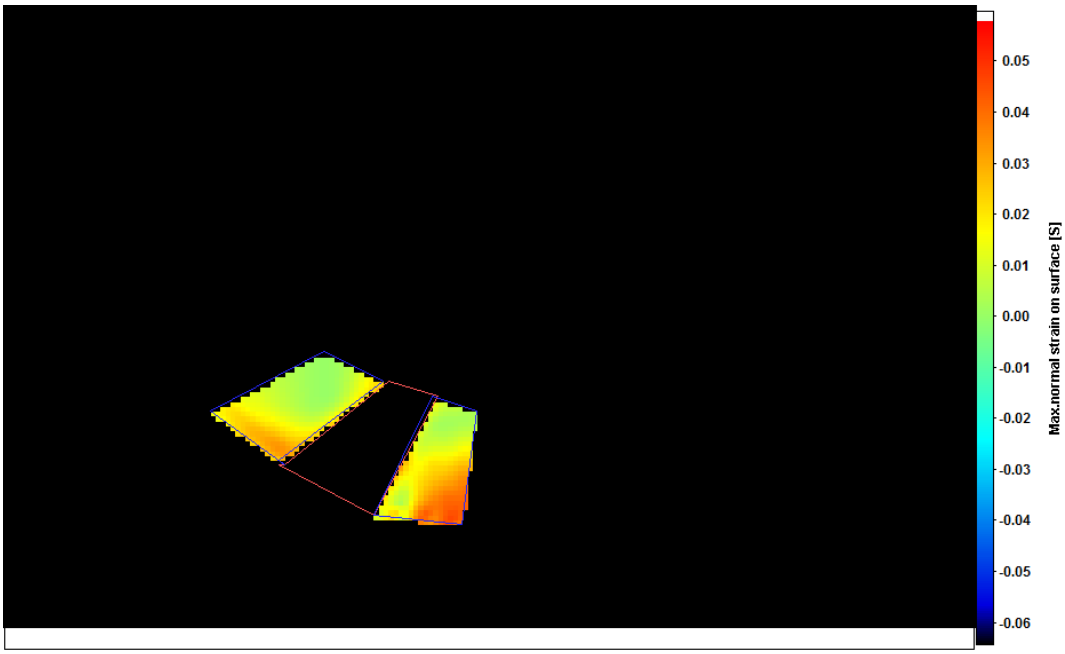

FIGURE 38: RESULTS OF GEOMETRIC MASK APPLICATION TO IMAGE

Masks adjacent to the damage were chosen to cover an equally sized area to the mask superimposed on the cut for similarity. They are also defined to start and end at equal radial distances from the center of the tire as the cut mask, since strain can vary with radial distance from the hub.

With the processing parameters and camera calibration used for this data set, the uncertainty for each maximum or minimum principal strain is 1.8%, or 0.018. Detailed calculations are provided in Appendix C: Uncertainty in Strain. This is similar to work by Moser et al. (2007) that compares DIC measurements on a rectangular rubber coupon to strain gauge measurements and finds a discrepancy of 0.01-0.02 strain, and similar work by Matsuzaki et al. (2010) that finds an average discrepancy of 0.02 strain between DIC and strain gauge measurements on a steel sample.

When these numbers are averaged over a large area, the uncertainty is reduced. In this case, averaging 50 or more vectors in each region, the uncertainty decreases to 0.26%, or 0.0026. This value is used as the threshold for absolute change in strain. In areas exhibiting higher strain, for example, 10%, an absolute change in strain of 0.26% between neighbouring vectors is less significant than the same absolute change in a region of lesser strain. For this reason, another visibility criteria was added, requiring that the ratio of strain in a damaged area be at least twice that of neighbouring regions for the fault to be classified as visible at that orientation.

The strain ratio between damaged areas and neighbouring regions is henceforth referred to as *C1*, and the absolute change in strain is referred to as *C2*. Together, both *C1* and *C2* are used to determine if damage is visible or not in a particular region as it is loaded. Defining S_c as the average strain over the damaged region, and S_n as the average strain in the neighbouring regions, *C1* and *C2* can be written mathematically as:

$$C1 = \frac{S_c}{S_n} \qquad [8]$$

$$C2 = |S_c - S_n n| \qquad [9]$$

5.2.3 Procedure: Orienting Damage, Controlling Displacement, and 3D Processing

Defining 0° as the point of load application to the tire, images were recorded in 10° increments as the external cut was rotated up to 90° from the point of load application. Cameras were installed at a 20° angle. The tire was depressurized for these experiments, for safety.

Instead of manipulating tire load, as in previous experiments, tire deformation, as measured by the displacement applied to the bottom of the tire, was manipulated. This allows for a more meaningful comparison with data gathered from pressurized tires. Furthermore, the applied displacement of 12.7 mm, or 15 %, more adequately represents site conditions. Appendix B: Tire Deformation describes the procedure used to estimate deformation in haulage tires from site images, and calculate the appropriate displacement to apply in the laboratory.

For each set of images, a 3D reconstruction of the tire was created from the stereo camera images. In DaVis, surface height is calculated over a grid, which for this experiment was given a spacing of 32 pixels horizontally and vertically, corresponding to the size of interrogation windows used to calculate strain. Seen in Figure 39, this reconstruction is typically sufficiently detailed to show the tire profile, the change in surface height at the external cut, as well as a faint outline of the lettering on the surface and other topography changes. The surface height in this case is given with reference to the surface of the calibration plate photographed prior to the tests.

The surface height is calculated with respect to the co-ordinate system of a particular camera, not from an object-based co-ordinate system. In the case of Figure 39, the camera from which the co-ordinate system originates is looking at the tire surface from an angle.

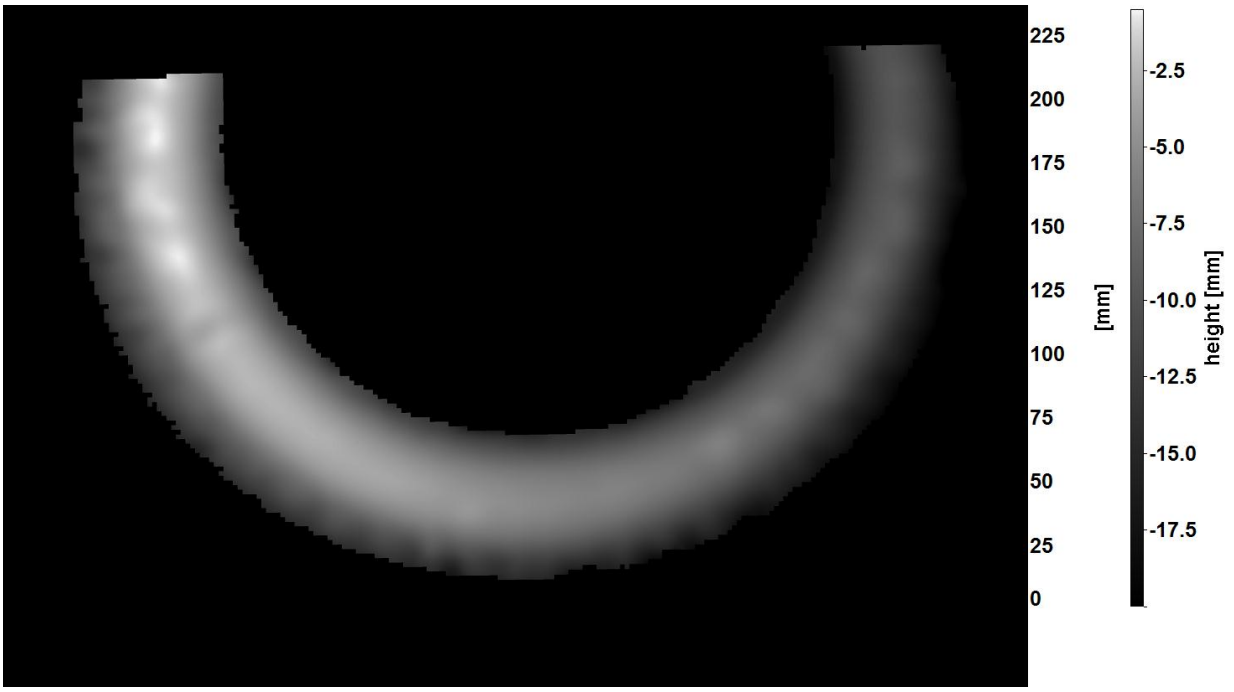

FIGURE 39: SOFTWARE RECONSTRUCTION OF 3D TIRE SURFACE

5.2.4 Strain in Damaged Regions by Orientation

3D strain was calculated over the tire surface from 0° to 100° away from the point of load application for each angle of rotation. The damage is expected to become less visible as it progresses away from the point of loading, as the global deformation and strain in the tire should decrease. However, as previously seen in experiments with damage positioned directly above the point of loading, the vertical displacement may be so great as to obscure damage visibility near the region of loading due to the relatively large deformations in that area.

5.2.4.1 Strain at External Damage by Orientation

Table 4 presents the findings of this investigation, listing the average minimum principle strain, absolute ratio of strain in the damaged area to undamaged adjacent regions, as well as the absolute change in strain magnitude between areas for the external tire cut at multiple orientations. The damaged region was rotated from 0° to 90° from the point of load application in 10° increments.

Table 4: Visibility of External Cut at Multiple Orientations Relative to Load

Angle (degrees)	Average minimum strain over cut	Ratio of minimum strain in damaged area compared to adjoining regions (*C1*)	Absolute change in magnitude of minimum principal strain (*C2*)
0	0.0249	4.14	0.0189
10	0.0023	0.395	0.0080
20	-0.0325	2.00	0.0164
30	-0.0341	2.02	0.0172
40	-0.0381	2.07	0.0197
50	-0.0315	2.17	0.0170
60	-0.0244	2.21	0.0134
70	-0.0178	2.15	0.0010
80	-0.0083	2.07	0.0043
90	-0.0040	2.41	0.0023

The data from Table 4 is plotted in Figure 40. From Figure 40, it can be observed that when the external damage is aligned with the loading, the minimum principal strain is still tensile, as the load causes the cut to split open further. As the cut is rotated away from the loading, the minimum principal strain changes to compression. During this transition, it becomes difficult to distinguish the damaged area from its surroundings, which manifests in the magnitude of the strain over the cut, as well as its relationship to neighbouring regions.

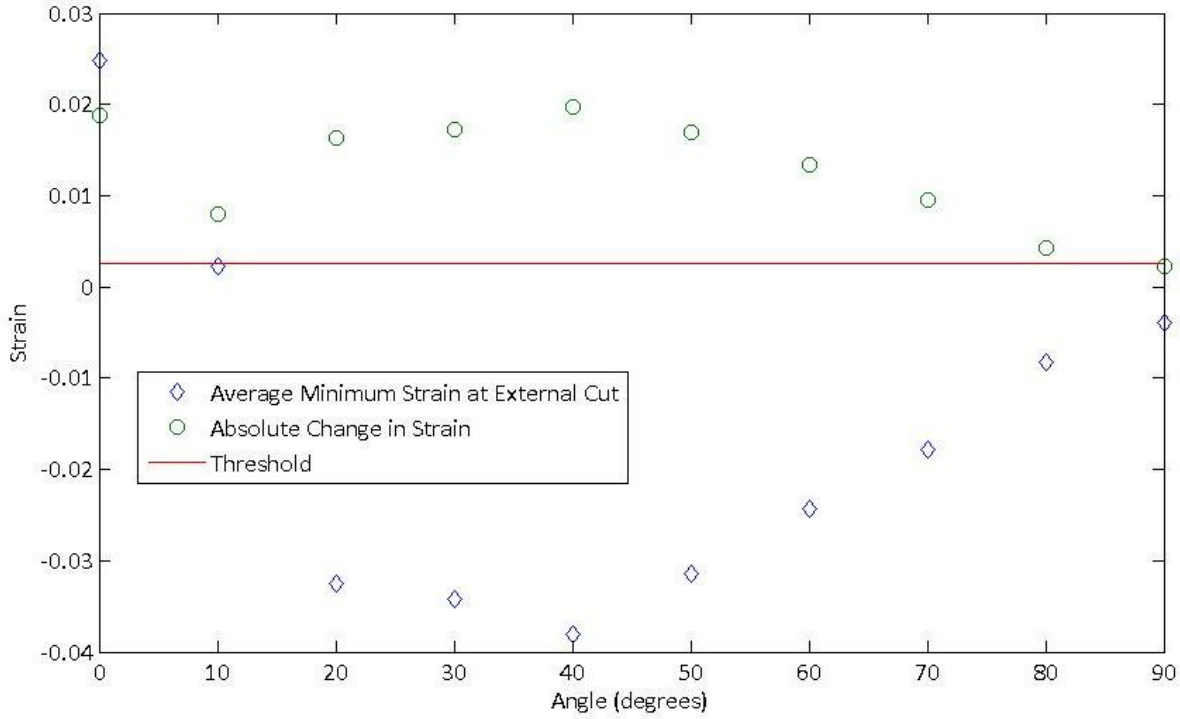

FIGURE 40: AVERAGE MINIMUM STRAIN AND ABSOLUTE CHANGE IN STRAIN OF EXTERNAL CUT

Between the region of 10° to 80° from the point of loading, the absolute difference in strain *C2* between the external cut and neighbouring undamaged areas exceeds the threshold of 0.0026. The ratio, *C1*, between these strains is greater than 2 within this region from 20° to 80°. For this type of damage, it appears that the strain ratio, as well as the absolute change in strain, are good indicators of visibility once the cut has moved out of the region of greatest deformation.

5.2.4.2 Strain at Internal Cut by Orientation

The analysis was repeated for the internal cut, with the results shown in Table 5. For this case, the maximum principal strain was calculated instead of the minimum principal strain, since the internal damage tended towards exhibiting tensile strain as opposed to compressive under these loading conditions. Unlike the minimum principal strain in the external cut, the maximum strain of the external cut remains tensile regardless of orientation.

Table 5: Visibility of Internal Cut at Various Positions Relative to Loading

Angle (degrees)	Average maximum strain over cut	*C1*	*C2*
0	0.0415	1.61	0.0157
10	0.0433	1.84	0.0197
20	0.0501	2.32	0.0285
30	0.0483	2.84	0.0313
40	0.0418	2.98	0.0278
50	0.0187	2.66	0.0117
60	0.0118	2.46	0.0070
70	0.0076	2.19	0.0041
80	0.0048	1.88	0.0023
90	0.0025	1.26	0.0005

The data from Table 5 is plotted in Figure 41. Using the visibility criteria of *C2* = 0.0026 and *C1* = 2, the internal damage meets visibility criteria over an area ranging from 20° to 70° from the point of load application. Contrary to the external cut, the change in strain between the internally damaged region and its neighbours is sufficient to exceed the detectibility threshold even in regions with high tire deformations, such as the area from 0° to 20° from the point of loading. As with the external cut, both the ratio and absolute value of the difference in strain due to the internal damage increase as the damage moves out of the areas of greatest tire deformation, then decrease as it continues to move away from the area of loading.

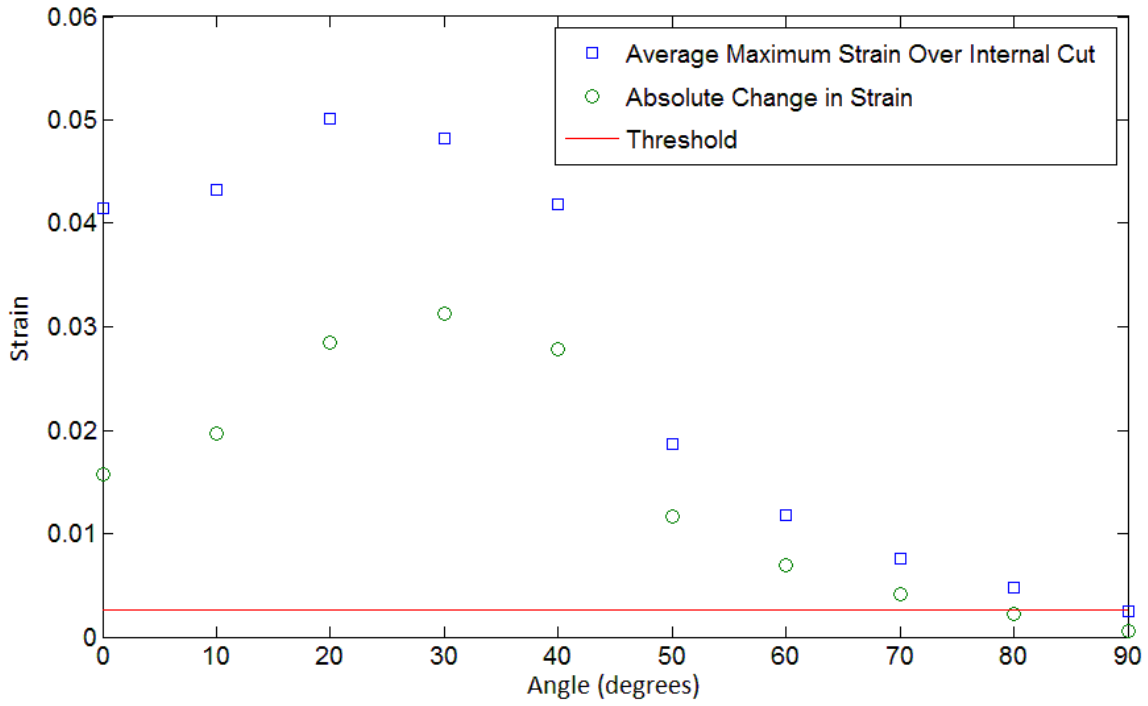

FIGURE 41: AVERAGE MAXIMUM STRAIN AT INTERNAL CUT AND ABSOLUTE CHANGE IN STRAIN

5.2.4.3 Comparison to Undamaged Regions

An assumption made up to this point is that these changes in strain do not occur when a similar technique is applied to undamaged regions, that is, when strain is calculated over an undamaged area and compared to neighbouring regions. Table 6 shows the results of a similar analysis applied to an undamaged section of the tire. None of the sampled undamaged areas met the criteria for visible damage, namely, there were no cases where the absolute change in strain exceeded 0.26% and the ratio of strain between the control area and its neighbours met or exceeded a factor of 2.

Table 6: Strain in Control Region at Various Orientations Relative to Load

Angle (degrees)	Average maximum strain over control area	*C1*	*C2*
0	0.0270	1.26	0.0056
10	0.0254	1.06	0.0015
20	0.0257	1.04	0.0011
30	0.0170	0.953	0.0008
40	0.0104	0.825	0.0022
50	0.0087	1.04	0.0004
60	0.0064	1.02	0.0001
70	0.0043	0.950	0.0002
80	0.0032	0.870	0.0005
90	0.0017	0.822	0.0004

5.2.5 Repeatability of Results

Up to this point, most of the experimental results have come from single tests, as opposed to averages over a large number of experiments. It is important to check that the strain measurements obtained from the camera system are repeatable and not singularities. The previous visibility tests were repeated for both the external and internal cut within the region of best visibility. A second test tire was obtained and its external surface was damaged. An analysis of the visibility of the external cut on test tire #2 under stationary loading was conducted under the same experimental conditions used to analyze test tire #1.

5.2.5.1 Multiple Loadings of Test Tire #1

The external damage was oriented at 35° from the point of load application, and the internal damage at 43°. Both were initially oriented at 40° but shifted as load was applied. The applied load caused a deformation of 15% in the tire. The load was applied then removed six times for each cut, with images being recorded progressively as the load was applied. However, only five sets of loading/unloading images were recorded for each cut, with the first load application being used to reduce hysteresis. As in previous experiments, the minimum strain of the external cut and the maximum strain of the internal cut were calculated and compared to neighbouring regions. Table 4 summarizes the average strains, standard deviations, and visibility criteria.

Table 7: Repeatability of Tire Visibility Results at a Specific Orientation

Type	**Average Strain**	**Standard Deviation**	***C1***	***C2***
External (min)	-0.0327	0.000988	2.30	0.0184
Internal (max)	0.0192	0.000542	2.56	0.0117

In both cases, the standard deviation of the strain measurements was less than the uncertainty of 0.0026. The damage met the visibility criteria for each set of strain measurements. Compared to previous measurements in the vicinity of these sets, the magnitude of these values is lower, for example, a strain of -0.0329 for the external cut at 35° orientation, compared to the previously measured -0.0341 at a 30° orientation and -0.0381 at 40°. The discrepancy is likely due to the change in operating procedure, which added a pre-loading step to reduce hysteresis in the deformation due to loading and unloading the tire.

For the external cut data, the 95% confidence interval for the mean strain ranges from -0.0339 to -0.0314. In neighbouring regions, it is -0.0154 to 0.0133. The visibility criteria for the cut are met over the whole confidence interval. The same holds true for the internal cut, with a 95% confidence interval for the mean strain of 0.0185 to 0.0198 over the cut and 0.00725 to 0.00775 in neighbouring regions.

5.2.5.2 Visibility of External Damage in Test Tire #2

A second test tire, of the same model as the tire used for the stationary loading tests, was prepared for experiments with a randomized speckle pattern. An external cut measuring 35 mm long, 7 mm across, and 2 mm deep was applied to the tire surface, similar in width, length, and orientation to the external cut on Tire #1, but somewhat shallower. The tire was depressurized, and a displacement of 15% of the tire radius was applied to the bottom of the tire. Images of the tire were recorded as the load was applied. This procedure was repeated with the external cut oriented from 0° to 90°, in increments of 10°. Surface strain was calculated and used to obtain visibility criteria *C1* and *C2*. Results are presented in Table 8.

TABLE 8: VISIBILITY OF EXTERNAL DAMAGE TO TIRE #2 BY ORIENTATION

Angle (deg)	**Average minimum strain over cut (Tire 1)**	**Average minimum strain over cut (Tire 2)**	***C1*, Ratio of minimum strain in damaged area compared to adjoining regions (Tire 2)**	***C2*,Absolute change in value of minimum principal strain (Tire 2*)**
0	0.0249	-0.0027	0.28	0.0069
10	0.0023	0.0019	0.20	0.0113
20	-0.0325	-0.0372	1.55	0.0132
30	-0.0341	-0.0378	1.73	0.0160
40	-0.0381	-0.0223	1.50	0.0075
50	-0.0315	-0.0153	1.73	0.0065
60	-0.0244	-0.0088	1.40	0.0025
70	-0.0178	-0.0037	1.52	0.0012
80	-0.0083	-0.0022	1.49	0.0007
90	-0.0040	-0.0012	0.71	0.0004

Using a threshold of 2 for *C1*, and 0.0026 for *C2*, the damage to Tire 2 would not meet the visibility criteria used previously. A possible explanation is that the external damage is less severe or otherwise different in nature from Tire #1. A parametric study of multiple tire faults under varying loading conditions could determine the influence of damage severity on visibility. Although the damage on Tire #2 does not meet the previously used visibility criteria, it still has a higher value of *C2* than the undamaged test region in many cases.

By changing the threshold for *C2* from 2.0 to 1.5, the damage to Tire #2 can be classified as visible, while still rejecting values obtained from undamaged tire areas. Using a threshold of 1.5 for *C1*, and 0.0026 for *C2*, the damage to Tire #2 is classified as visible from 20°-50°. A plot provided in Figure 42 shows the visibility criteria C2 for the external cut on Tire #1 compared to Tire #2. In both cases, the trends are similar, with visibility increasing until a peak between 30° and 40°, after which visibility decreases. Overall, the external damage to Tire #2 is less visible than the damage to Tire #1. The difference may be due to the depth or severity of the cuts, which can be investigated as part of a parametric study of tire damage as future work.

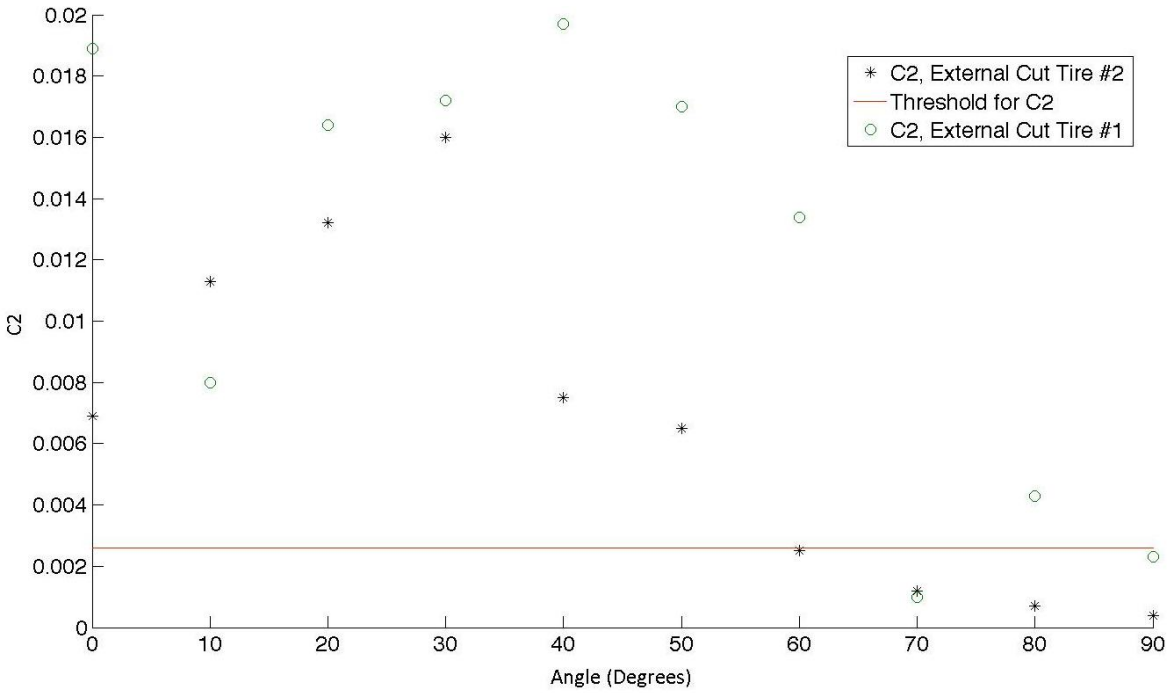

FIGURE 42: COMPARISON OF VISIBILITY CRITERIA C2 BETWEEN EXTERNAL CUTS ON TIRE #1 AND TIRE #2

5.2.6 Discussion and Applications

The results from the visibility analysis of the external and internal damage suggest that damage is most visible when it has exited the region of greatest deformation near the area of load application, and before the surface strain due to the applied loading has decreased below an acceptable threshold. While a simple definition of visible/not visible has been used, it fails to indicate when the damage is most detectible. Hence, a second threshold was added to the absolute change in strain, *C2*, of 0.013, or 5 times the minimum change to reach the definition of "visible", which now defines the damage as having "good" visibility in that region.

A plot summarizing the visibility, based on absolute change in strain, is presented in Figure 43. Using solely the absolute change in strain as an indicator, the region of "good" visibility for both faults is from 0°-40°. Including the strain ratio, *C1*, the area of best visibility reduces to 20°-40° for both faults.

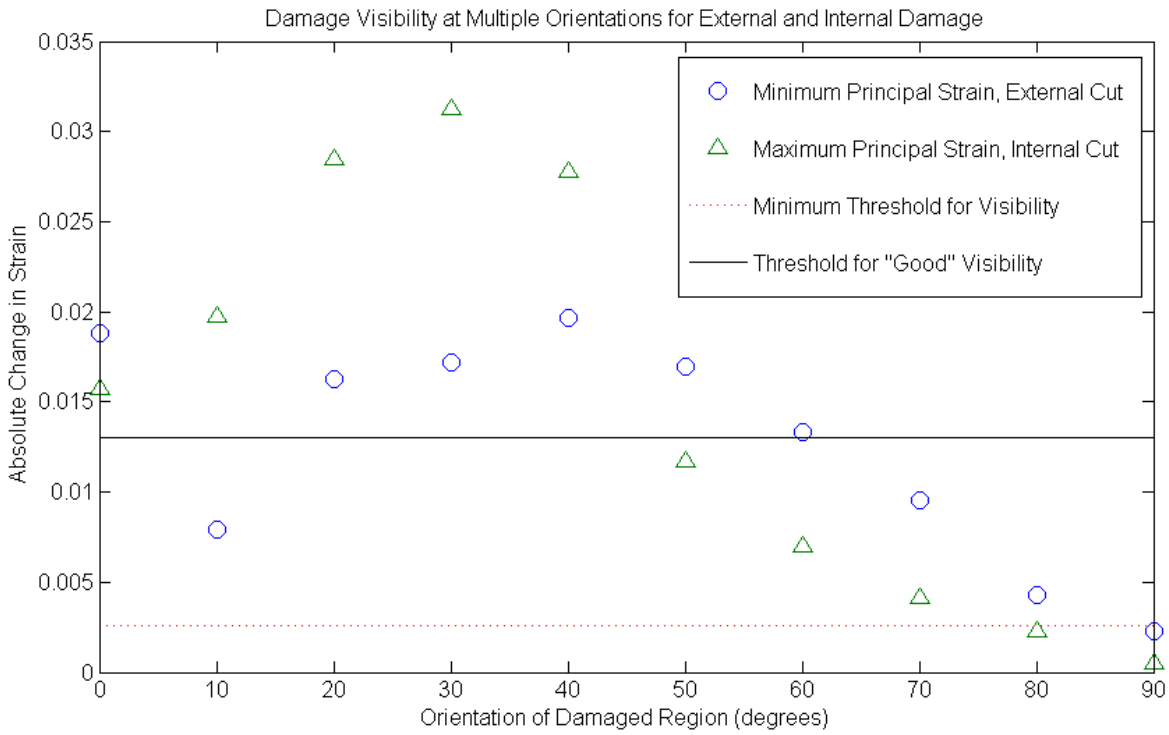

FIGURE 43: REGION OF BEST VISIBILITY FOR INTERNAL AND EXTERNAL CUT

Values used for visibility thresholds for damage on the first test tire were not adequate to detect damage in a second test tire. For that reason, the strain ratio, *C1*, was lowered to 1.5 for the second tire, which still rejected undamaged areas. Applying the process used to detect damage under stationary loading to the second test tire, an external cut was successfully detected from 20° to 50°. Overall, the values of C1 and C2 were lower, which could be due to the properties of the cut, for example, having a shallower depth than the damage to the first test tire.

What are practical applications of these results? Knowledge of the areas of high damage visibility in this method of processing, and criteria for defining visibility can be implemented in future development of an on-site automated tire inspection system. Restricting the processing to high-visibility areas reduces the processing load, and consequently processing time when analyzing images. The visibility criteria could be incorporated into a search algorithm to automatically detect areas of potential damage on the tire. These results will be considered in future work involving the design and development of an automated tire inspection system.

5.3 Damage Visibility from Rotating Trials

The investigation of damage visibility in tires has focused on data from tires that were held stationary as load was applied. In a field application, however, the tire will be continuously loaded and the tire will rotate between frames. This section examines the necessary pre-processing to extract fault information from a tire, its implementation in the laboratory, and the visibility of different tire cuts from images of a rotating tire.

5.3.1 Preprocessing: Rotating and Aligning Tire Images

Pre-processing is required for these image sets to remove displacement vectors obtained due to the bulk translation and/or rotation of the tire. An individual region of the tire is loaded as it approaches the ground, and relatively unloaded as it leaves that orientation. To determine the strain field, it is necessary to identify the tire in each photograph as the vehicle is moving past, determine the rotation of the tire, and find the region of interest in each shot. With the tire rotated back to its initial orientation in the first frame, the strain field can be calculated from the change in loading over the region of interest.

The process of re-alignment, re-rotation, and superposition is illustrated in Figure 44. Re-rotating and aligning the two images allows for a comparison of small-scale deformation of the tire surface as opposed to large-scale calculations of the displacement of the tire region.

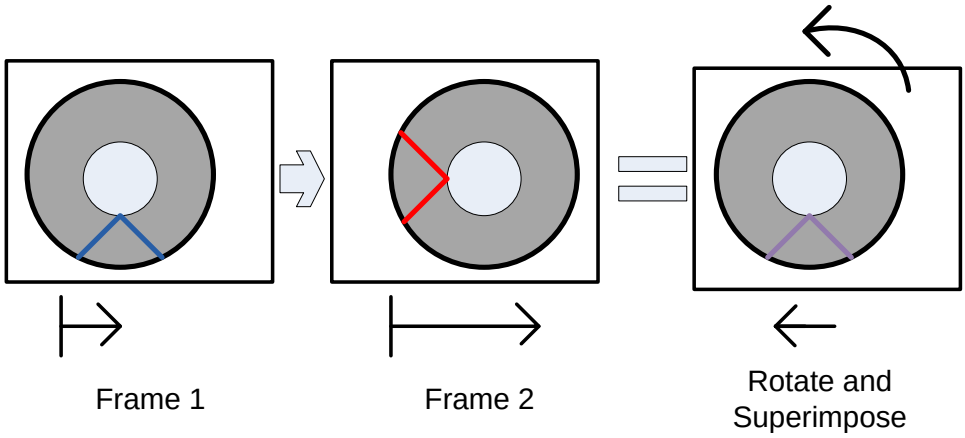

FIGURE 44: ELIMINATING TRANSLATION AND ROTATION OF TIRE BETWEEN FRAMES

Figure 45 shows two successive images of a tire as it rotated approximately 30°. Using custom MATLAB software, Frame 1 was re-centered and aligned with the orientation of Frame 2. Comparing the rotated Frame 1 with Frame 2, the region at the bottom of the tire is relatively unloaded in Frame 1, and is loaded and deformed in Frame 2.

Frame 1 Frame 1 Rotated to Position 2 Frame 2

FIGURE 45: EXAMPLE OF RE-ROTATION APPLIED TO TIRE IMAGES

Rotation of the tire alters the loading state of a given region. The change in loading results in strain on the tire surface. There are multiple options for re-rotating tire images to determine surface strain. For example, taking an image and finding its counterpart after a rotation of approximately 180° would allow for calculation of the strain in a given region between its fully unloaded and fully loaded state. A disadvantage of this option is that progressing from unloaded to fully loaded in only a single step results in significant distortion of the tire surface that could result in failure of the strain calculation algorithms. In stationary experiments, multiple images were taken as the loading was applied, and the total change in strain was calculated from the sum of the strain in consecutive pairs of images.

An alternative to pre-processing is to process the images as they are recorded and to subtract the bulk rotation and displacement of the tire to obtain the surface deformation. However, measurable displacement is related to processing window size, and subsequently spatial resolution. The displacement due to rotation of the tire is potentially much greater than the deformation from a change in loading. As a result, interrogation windows would need to be larger to calculate displacement vectors, reducing spatial resolution. Instead, images are pre-processed and re-rotated to reduce the magnitude of the calculated displacement vectors. Multiple pass processing with grid refinement could also address these issues, but is not currently possible for 3D measurements using the experimental software (DaVis 8.1).

An example of a displacement and strain field calculated without re-rotation is presented in Figure 46. These results were calculated using the same window size and processing used in the stationary loading cases, that is also used to analyze pre-processed images from rotating tire tests. The displacement vectors, in black, show a bulk rotation of the tire. However, in the upper left corner of the tire, there is irregularity in the vector field that does not agree with observed motion of the tire. This is likely because the interrogation windows were too small to calculate the actual displacement of the tire surface in this region. Pre-processing the images used to analyze the visibility of tire damage from rotating tests reduces the magnitude of the displacement vectors by reducing the bulk rotation of the tire.

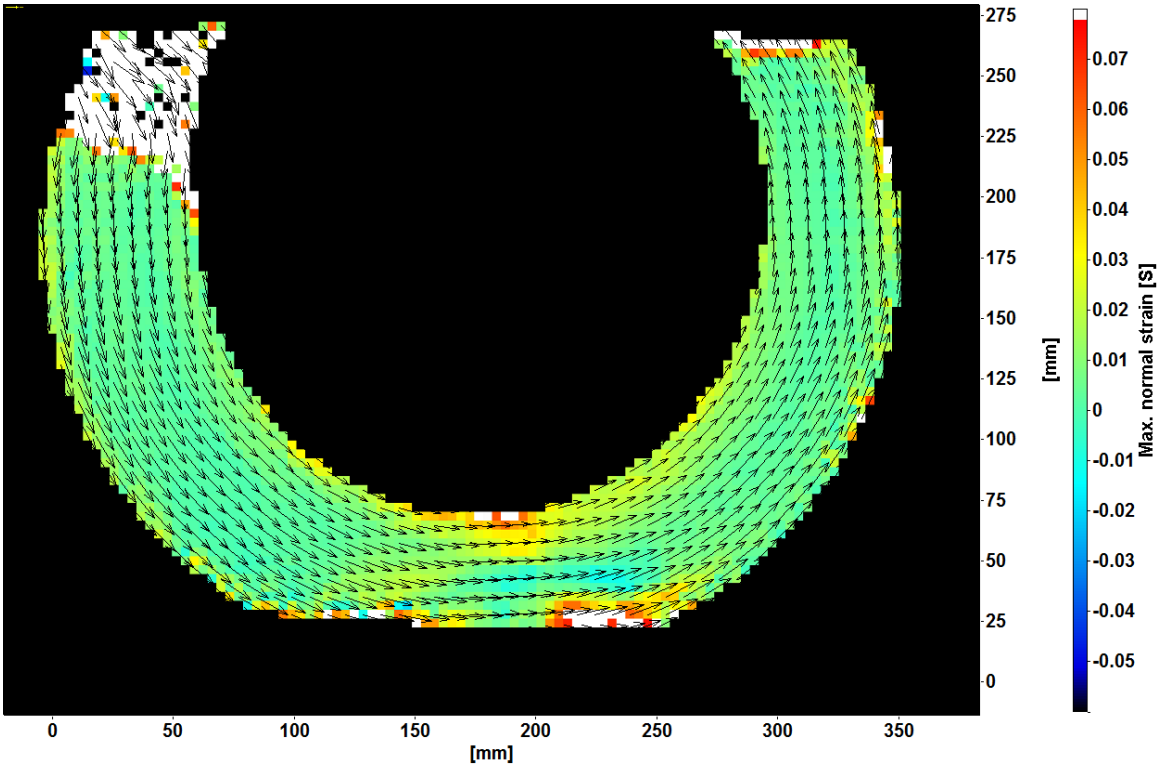

FIGURE 46: TIRE DISPLACEMENT CALCULATED FROM ROTATING IMAGE SET WITHOUT RE-ROTATION

5.3.2 Asymmetry due to Processing

For rotating tests, strain is calculated from two consecutive images to reduce the distortion of the tire surface. It is expected antisymmetry will arise due to the directionality of processing the images. In stationary loading, it was assumed that the observed changes due to the cuts would be the same whether the cut was oriented at 10° or B-10° from the point of loading. In this case, the same cannot be assumed, since the cut appears to be loaded through consecutive images as it approaches the point of loading, and unloaded as it rotates away from that point.

Consider Figure 47 as an example of asymmetry in strain due to rotation. Points 1, 2, and 3 represent the orientation of the damage, in red, in three consecutive frames. If the tire is rotated counterclockwise, the cut appears to compress from image 1-2. From image 2-3, however, the damage expands. Using an unloaded tire as a reference, the strain calculated at the cut could be the same for images 1 and 3. With point 2 as a reference, however, a change in sign is expected.

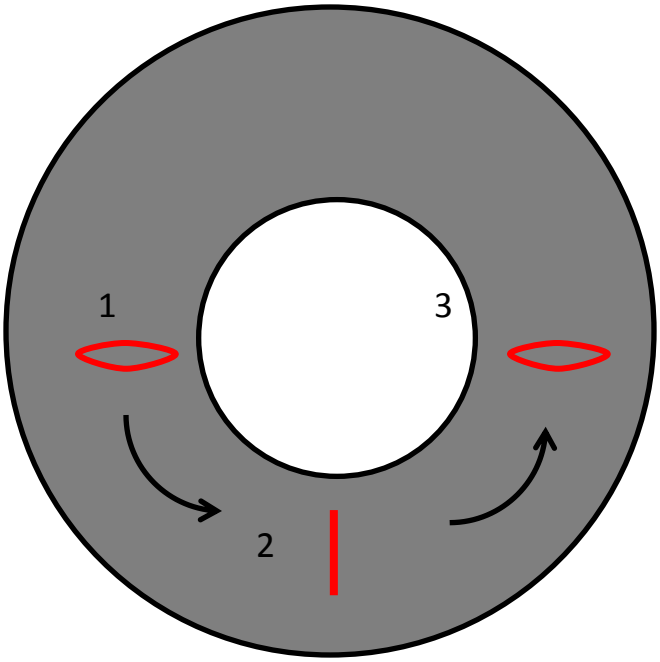

FIGURE 47: COMPRESSION AND EXPANSION OF DAMAGE FROM SUCCESSIVE ROTATING IMAGES

5.3.3 Procedure: Preprocessing & Tire Rotation

Using the tire testing apparatus, the motion of the tire was restricted to permit rotation but not translation of the tire between frames, simplifying image pre-processing. By displacing the mill table, the tire was deformed by 15%, as defined in earlier experiments. Instead of re-applying the loading at each orientation of the tire, the mill table was kept in a constant position as the tire was rotated counterclockwise. Images were recorded at 10° +/-5° increments of rotation for a total of 36 images as the tire made a full rotation.

Before calculating surface strain, tire images were re-rotated manually in DaVis using surface landmarks for reference, selecting a center of rotation and specifying the angle of rotation. For an image, *i*, the next consecutive image, *i+1*, was rotated back, clockwise, to the position of the previous image, *i*. The 3D reference surface and strains were calculated from these sets using 32 pixel interrogation windows with 50% overlap.

The tire used in the experiment had three damaged areas, specifically, the internal and external cuts examined earlier, plus an external cut in the tangential direction. Using a tire with multiple damaged regions ensures that the pressure and loading are consistent in the analysis. Sharp

discontinuities were previously observed in the strain surrounding the damaged areas. The damage was spaced accordingly so the effects of the cuts do not overlap. Figure 48 shows the location of each damaged region, with 1 indicating the tangential cut, 2 indicating the radial cut, and 3 indicating the internal damage.

FIGURE 48: LOCATION OF DAMAGE ON TEST TIRE, WITH 1 INDICATING THE TANGENTIAL CUT, 2 INDICATING THE RADIAL CUT, AND 3 INDICATING THE INTERNAL DAMAGE

5.3.4 Visibility of Damage by Orientation from Rotating Tests

Surface strain was calculated from a set of 36 images of the tire as it completed a 360° rotation. The maximum principal strain was used to determine damage visibility, since both internal and external cuts were observed to be in tension at some orientations during stationary tests. A co-ordinate system, shown in Figure 49, was defined with 0° at the point of loading on the bottom of the tire. Strain was calculated over the region highlighted in red to provide sufficient information to establish the strain surrounding the cut.

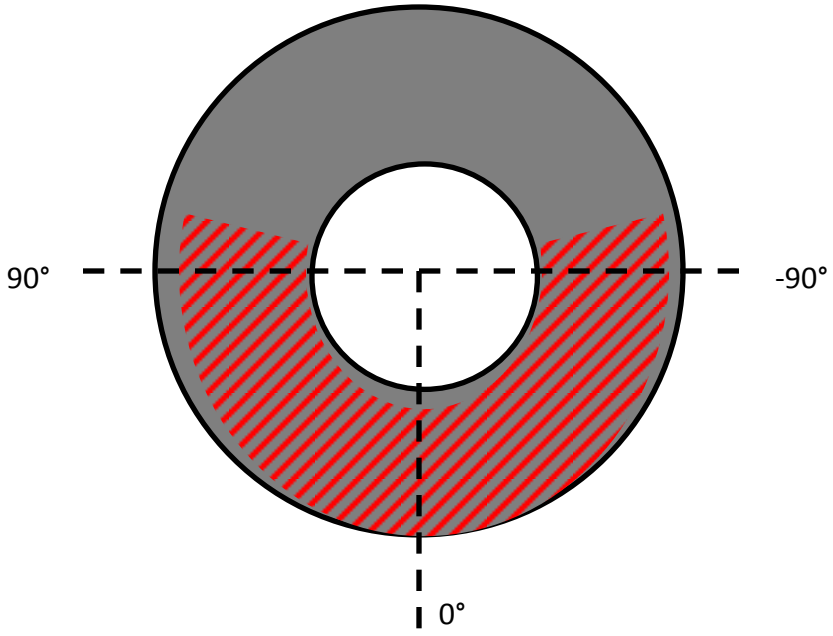

FIGURE 49: CO-ORDINATE SYSTEM FOR TIRE RE-ROTATION

Similar to the stationary loading tests, the magnitude of strain in damaged regions was calculated at multiple orientations. The strain in damaged areas was compared to neighbouring regions to determine the two visibility criteria, namely, the ratio of strains between areas and the absolute change in strain. These results, for two external cuts at different orientations, and the internal cut, are presented in Figure 50, which plots the strain ratio, *C2*, against the orientation of the damage. Points which met both damage criteria of having a strain ratio greater than 2, and an absolute change in strain magnitude greater than 0.0026, are shaded in the figure.

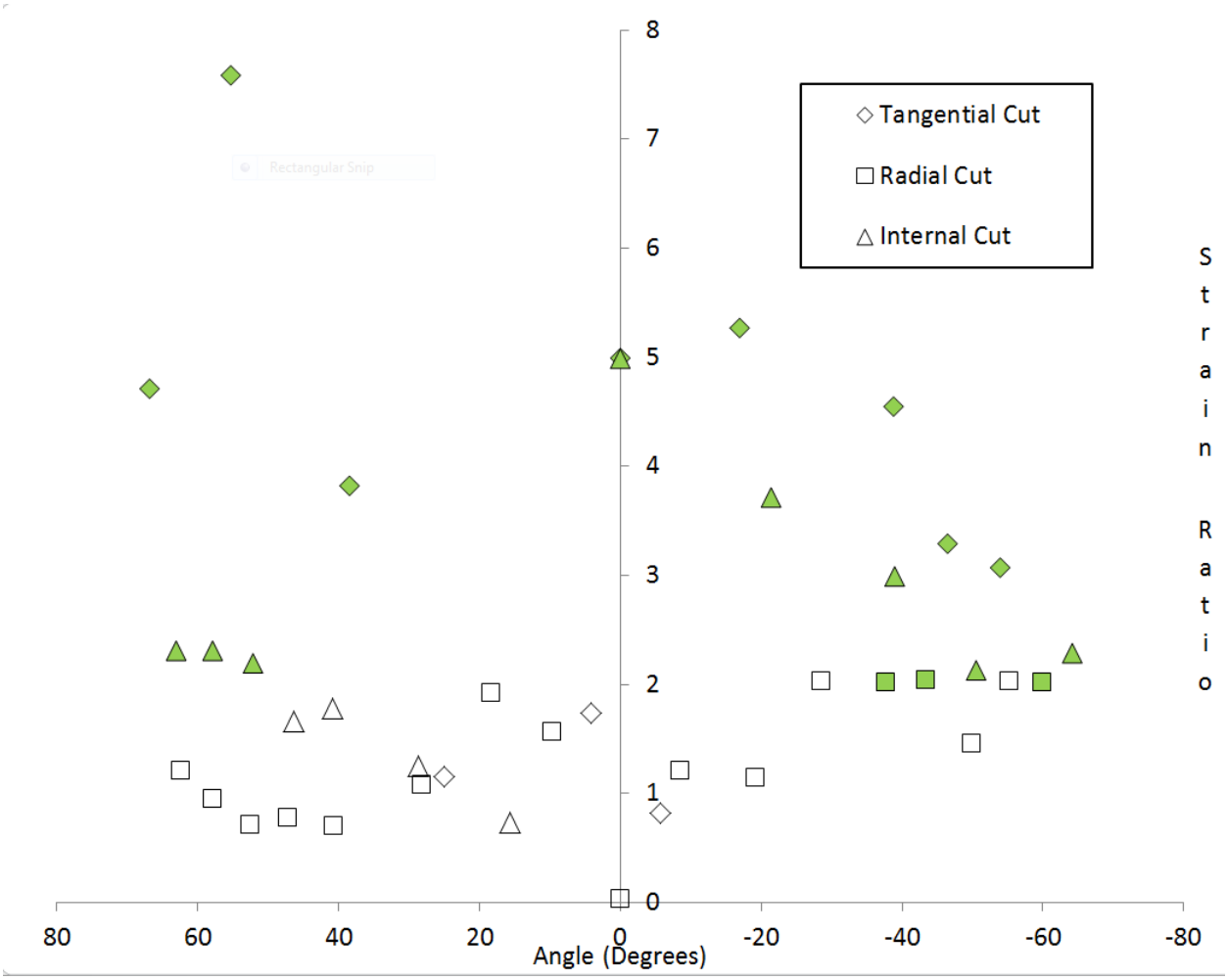

FIGURE 50: DAMAGE VISIBILITY BY TYPE AND POSITION FROM RE-ROTATED TIRE IMAGES

The value used to evaluate the damage visibility in this case was the maximum principal strain, which is typically tensile. From 0° to -80°, where the tire is expanding between images, the maximum strain is greater. Similarly to the results from the stationary loading tests, the region of best visibility for the tire damage falls roughly between -20° to -60° from the point of loading. It is likely that the damage is more visible in this region since it appears to be in tension, having a greater effect on the maximum strain than when it is under compression.

There is asymmetry in the results shown in Figure 50, with more damage successfully detected from 0° to -80° than from 0° to +80°. The asymmetry is likely due to the procedure used to analyze the images, where an image *i* is compared to its neighbour, *i+1* that has been rotated counterclockwise by 5°-15°. As a result, from 80° to 0°, the damage is subjected to increasing amounts of load as it approaches the point of loading at 0°, which compresses the tire. From 0° to -80°, it is subject to progressively decreasing load, and the tire expands.

Another observation from Figure 50 is that the tangential cut meets visibility criteria at nearly every orientation, followed closely by the internal damage, while the radial cut is successfully detected in only 3 images. This is likely due to the severity of the damage, with the internal damage being the largest, measuring 2.5 by 7.5 mm. The tangential cut measures 45 mm long by 1.5 mm wide and 3.5 mm deep, penetrating further than the radial cut, which measures 6.5 mm wide by 35 mm long and 2.5 mm deep. An acknowledged limitation of this work is that the influence of the severity of the damage is not investigated, which likely influences its visibility.

Figure 51 shows the resulting strain field and displacement arrows from two consecutive images. A change from the stationary loading studies is that the regions to either side of the point of loading appear to undergo the most significant deformation, instead of the area directly above the point of loading. This is due to the rotation of the tire between images, which also causes the bottom surface to appear to be at an angle.

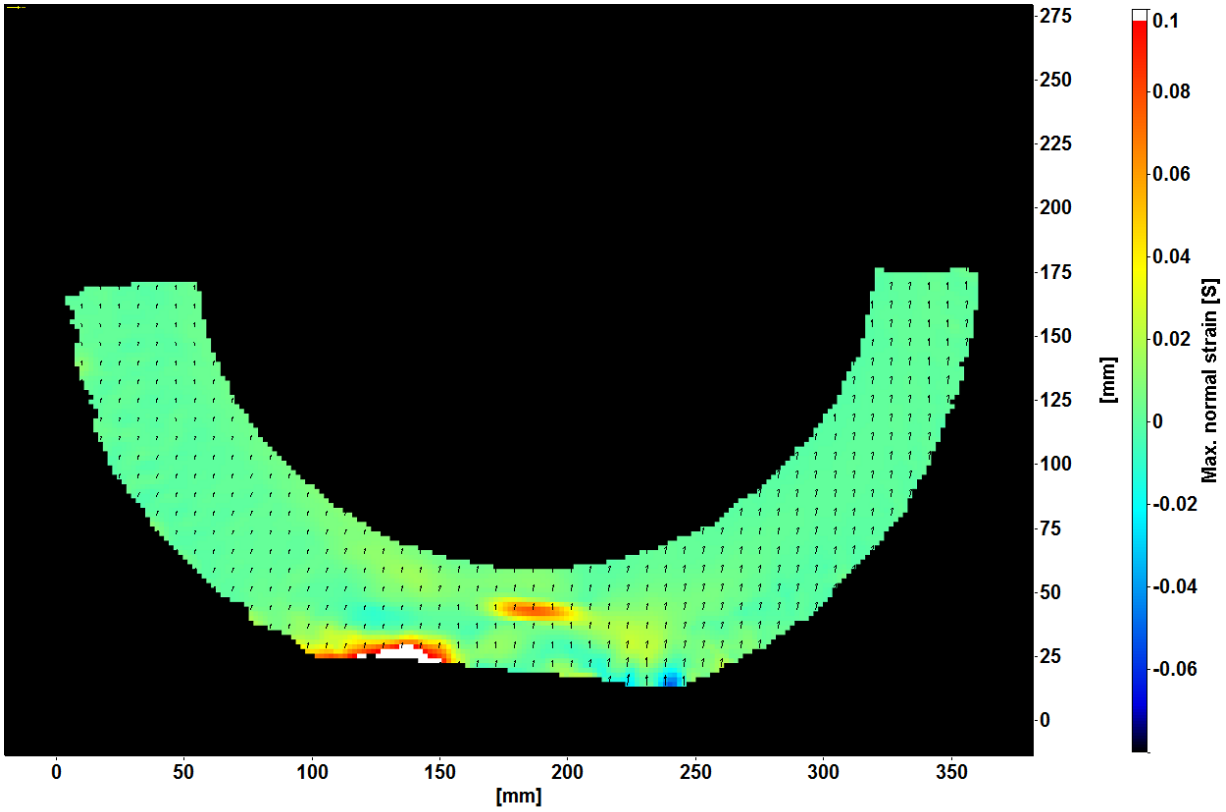

FIGURE 51: SAMPLE STRAIN AND DISPLACEMENT FROM RE-ROTATED IMAGES, SHOWING TANGENTIAL CUT

Error is introduced during the manual re-rotation process. Misalignment between the estimated and actual center of rotation can result in residual motion vectors. Misalignment between the tire and the calibration plane also results in residual rotation vectors since the rotation process is 2D but the actual uncorrected rotation of the tire is 3D.

5.3.5 Summary

Surface strain measurements were obtained from images of a rotating tire, expanding on previous work investigating damage visibility in the tire under stationary loading conditions. In total, the strain in damaged tire areas, calculated from re-oriented consecutive images of a rotating tire, met the visibility criteria in 19 out of 40, or 47.5% of the image pairs. The tangential cut was detected the most frequently, followed by the internal cut and radial cut.

There was a directional effect on the results of this experiment due to the rotation of the tire. This causes a given region of the tire to appear to compress as it approaches the loading area, and decompress as it leaves. As a result, when the maximum principal strain is used to determine visibility, the damage has greater visibility on the decompressing side of the tire compared to the compressing side. Similar to other tests, the damage was most visible in an area 20°-60° from the point of loading.

This work is a step in moving from laboratory experiments to analyzing tires at an industrial site, showing that it is feasible to detect damage using strain calculated from images of a rotating tire, and describing a procedure to process the images to obtain these measurements. In this case, an average rotation of 10° between images was sufficient to successfully detect the damage. A region of damage visibility was obtained, which could be used to reduce the amount of processing required for a field application.

Chapter 6: Conclusions and Future Work

This section presents the conclusions from the analysis of displacement and strain in a tire using DIC algorithms, from both stationary and rotating images. These results open up possibilities for future work in both laboratory and industrial settings. Finally, the objectives, recommendations, and applications for this work are summarized at the end of the section.

6.1 Conclusions

A preliminary investigation was conducted to observe the effect of simple tire damage on the displacement of the tire surface under idealized conditions, using images of the tire before and after the damage was incurred. This work focused on establishing the procedure and requirements for obtaining tire information. Controlled loading was applied to the bottom of the tire using the test apparatus. Observations were used to improve DIC performance by reducing pattern size and increasing the density of the dots in the speckle pattern applied to the tire for DIC processing.

The displacement and strain in damaged tire regions under loading was then investigated. The damage was held stationary with respect to the load to eliminate vectors arising due to bulk movement of the tire. Different indicators, such as horizontal, vertical, and out-of-plane displacement, as well as horizontal and vertical strain, were calculated over the tire surface to determine which measurements were better for displaying and understanding the behaviour of damaged regions. It was found that visually, strain gave a clearer indication of tire damage than displacement.

Both internal and external damage was photographed under load, applied directly beneath the cut. At this particular orientation, the region surrounding both cuts expanded under loading while undamaged areas were compressed. Although the internal damage could not be seen from the exterior of the tire, its effects on the strain field were clear, suggesting that strain is a feasible damage indicator.

Using maximum and minimum principal strain as a damage indicator, two metrics were devised to quantify damage visibility. The absolute change in strain between the damaged region and neighbouring areas was referred to as *C2*, with a minimum change of 0.0026 required to define the damage as visible. The threshold of 0.0026 is related to the uncertainty in the strain measurements over an area. It was also required that the ratio of strain in the cut to strain in surrounding areas, referred to as *C1*, be equal to or greater than 2.

After viewing both damage types at a single orientation, the experiment was repeated, moving the cuts to multiple orientations with respect to the loading. The aim was to determine where, with respect to the loading, the cuts were most and least visible, as it had earlier been observed that the severe compression at the bottom of the tire could obscure smaller changes in strain due to damage. It was found that the damage met visibility criteria at orientations within 20° to 70° away from the point of loading at the bottom of the tire. Notably, undamaged regions of the tire met the visibility criteria in none of the 10 orientations tested. Defining good visibility as regions where *C1* exceeded 2 and *C2* was greater than 0.013, the area of good visibility for both internal and external damage was between 20° and 40°.

Stationary loading tests were repeated in the area of good visibility to ensure that the results were reproducible. Creating a 95% confidence interval from 5 sets of loading data from both cuts, the visibility criteria were met at both extremes of the interval for both internal and external damage for a single tire. A second test tire was also prepared, and external damage to the second test tire was detected. The behaviour of the fault visibility in the second tire followed the visibility trends for the first test tire, with best visibility between 30° and 40° from the point of loading.

After establishing the visibility of tire damage under stationary conditions, the investigation was expanded to include rotating sets of tire images, similar to what would be obtained from an industrial application. Two external cuts and one internal cut were present on the tire. Images were recorded of a rotating tire and used to calculate tire strain from consecutive image pairs. Pre-processing of the images was implemented to reduce the effects of the bulk rotation of the tire on the calculated vector fields.

Unlike previous tests, there was a directional effect on the results of this experiment due to the rotation of the tire, causing a given region of the tire to appear to compress as it approaches the loading area, and decompress as it leaves. Since the maximum principal strain was used to determine the visibility criteria, the damage was more visible on one side of the tire than the other. Similar to other tests, the damage was most visible in an area 20°-60° from the point of loading.

This work is a step in moving from laboratory experiments to analyzing tires at an industrial site, showing that it is feasible to detect damage using strain calculated from images of a rotating tire, and describing a procedure to process the images to obtain these measurements. A region of damage visibility was obtained, which could reduce the amount of processing required in a field application if vectors are calculated over a smaller area.

6.2 Future Work and Industrial Applications

Having observed damage in a single tire in a laboratory setting, there are numerous applications for the development of camera-based systems for tire condition monitoring, in both research and industry. This section discusses future possibilities for laboratory investigations into strain measurements using digital image correlation (DIC) in tires, as well as industrial applications for image-based monitoring systems. Particular focus is given to strategies for adapting the methods used for damage detection in this work for field applications.

6.2.1 Laboratory

There are several possibilities raised by this study for future analysis of tire strain in a laboratory setting using DIC. For example, expanding on the observation of simple tire damage under stress, complicated forms of tire damage such as fatigue or belt separation could also be investigated. Furthermore, the severity of tire damage, which was controlled for this work, could be manipulated in future experiments. Another controlled parameter, the pattern on the tire, could also be manipulated to determine the requirements for visual texture in a field application. There is also the potential to use the system to measure properties of specific tire models, where desired, and combine and compare these results to FEA models to better understand the behaviour of a particular tire and drive improvements.

6.2.1.1 Experimental Studies and FE

Generally, tires can be described as having a complex geometry and consisting of multiple layers of composite materials. As a result, tire studies tend to focus on empirically obtained properties of specific models and types of tire, or on predicting the response to various conditions using finite element (FE) models. The same optical techniques used to obtain strain values to detect damage could also be implemented in these research areas. For example, full-field strain information could be used to describe tire behaviour in empirical studies, while other tire properties such as elasticity could be derived from displacement fields.

Empirically obtained tire properties can be incorporated into finite element models. Deformation and strain predicted by finite element models could be compared to displacement and strain obtained using DIC in experiments and used to improve or validate FE models. One area of particular interest is crack propagation in rubber composites, where DIC measurements could be compared to FE models to gain a better understanding of damage mechanisms in rubber. An advantage of using an optical method over a traditional approach is that it does not require alteration of or contact with the surface under examination.

6.2.1.2 Damage Type and Severity

This work examined simple, straight cuts to the tire. In a field application, tire damage can be more complex than a sidewall cut or puncture. Future work could examine larger samples of failed industrial tires with belt separation, tread separation, or fatigue damage in the laboratory. Fatigue damage could also be replicated using test equipment to repeatedly load and unload a tire, and calculating the strain on the tire surface multiple times after a given number of loading cycles were applied.

To determine the sensitivity of a strain-based approach for damage detection in tires, the severity of induced damage in the laboratory could be manipulated. This could include varying the dimensions of the cut, such as depth, as well as the proximity of the damage to the tire rim or tread.

6.2.1.3 Pattern

Another parameter that was controlled in this work was the pattern applied to the tire. For field and maintenance use, it may not be possible to apply an optimally sized dot pattern, or even apply a pattern at all. Environmental conditions, such as water exposure and dirt could smudge or obscure the pattern in field use. However, there could still potentially be sufficient surface texture to obtain some information from the tire. Future work could investigate the sensitivity of the resolution and fault visibility of the damage detection procedure to environmental effects and pattern properties such as dot size and density.

6.2.2 Industrial Applications

Mining operations were observed with the aim of developing recommendations to guide the future development of an optical tire inspection system that could be used in the field. This section discusses possible implementations of such a system, describe site operations and potential challenges at a field location, and provide suggestions for developing an optical tire monitoring or inspection system. Complementary applications for a camera system not involving DIC are also discussed, namely, optical pressure and temperature measurements.

Site visits and meetings were arranged with representatives of Syncrude Canada Ltd. to discuss opportunities for implementing an optical tire inspection system at a mine site. Potential installation locations for such a system were inspected and evaluated. Constraints pertinent to system installation were discussed with multiple levels of field workers and management, as well as topics of interest pertaining to the site commissioning of a tire inspection system.

6.2.2.1 Operations and Observations

A mine site was observed to gather information for developing an optical inspection system. The site explored by the research team uses truck and shovel mining, instead of a drag line, to transport ore from the oilsand-rich pit to a dumping site, where it is broken down into smaller pieces and fed into a piping system to be further aerated and upgraded. A typical front shovel and truck are pictured in Figure 52.

FIGURE 52: TRUCK AND SHOVEL AT PIT

Trucks travel at speeds of up to 60 km/h along haul roads from the pit to the crusher dump, carrying loads of up to 400 tonnes. On average, this trip takes from 15 to 40 minutes depending on the distance and road conditions. Unloading the ore, shown in Figure 53, puts extreme stress on the vehicle frame as well as the rear tires as the load is shifted.

FIGURE 53: OFFLOADING ORE AT CRUSHER DUMP

With an 8-hour or less frequency, trucks stop at a rest area between the pit and crusher for shift changes and/or brief visual inspections. Figure 54 was taken from a safe viewing location at the rest stop, showing viewing conditions for condition monitoring at the rest area.

FIGURE 54: SIDE VIEW OF HAULAGE TIRE AT REST STOP

6.2.2.2 System Description

Multiple factors influence the optimum choice of equipment, set-up, and location for an optical inspection or monitoring system. Similar to the laboratory set-up, a calibrated multi-camera system could be installed on tripods at a fixed distance from the trucks. Consumer-grade SLRs would provide sufficiently detailed images, using high-powered lighting to illuminate the tires. A full revolution of each tire would be captured by the imaging system without having to re-position the cameras. Images could be analyzed immediately on site, using specialized software, if a computer was included with the cameras, or they could be processed remotely.

A possible location for the cameras would be in a maintenance bay or at a rest stop. Trucks routinely stop at rest stops to change operators, and also undergo scheduled maintenance in repair bays, so both locations are heavily frequented. In both cases, the trucks could be driven past the cameras at reduced speed to prevent image blur. An inspection system in the maintenance bay could be used to assist with diagnostics of damaged tires, or as part of routine truck maintenance. In the field, at a rest stop, for example, the system could be used to flag damaged tires for further inspection. As shown previously, it is possible to safely approach the tires at a rest stop to produce a detailed image for analysis.

6.2.2.3 Practical Considerations

Multiple factors influenced the choice of location and equipment for the camera system. Constraints observed on site, related concerns, and the recommended course of action are summarized in Table 8: Design Considerations. Most concerns can be addressed with equipment and procedure changes, although there is room for additional study of the effects of dirt, dust, and other environmental conditions on the accuracy of the DIC algorithms. The main conclusions drawn from the site visits were that the cameras should be installed in a sheltered, bright location where the truck speed can be controlled safely, namely, a maintenance bay or shed at a rest stop.

TABLE 9: DESIGN CONSIDERATIONS FOR OPTICAL INSPECTION SYSTEM

Factor	Concerns	Recommendation
Inadequate Lighting	Poor image quality	Install additional lighting on location
Weather	Damage to equipment	Indoor or sheltered installation
Tire Size	Poor image resolution	Add cameras to the system to reach desired spatial resolution.
Driving Speed	Motion blur in images	Choose a location where tire speed can be safely reduced while images are recorded
Tire Pattern	Required for accurate measurement	Process images of uncoated tires to test if existing surface data is sufficient for correlation. Test different coating strategies on industrial tires.
Dirt/Dust	Obscured tire pattern	Conduct additional studies to determine if dirt is detrimental or can be considered a unique surface pattern in image processing
Rotation and Translation of Tires	Can cause processing artefacts/inaccurate results	Develop procedure for registering tire images and determine severity of registration errors on quality of results
Power Accessibility	Required to run cameras/computer	Install system close to available outlets, or determine generator requirements.
Occlusion of Damage	No fault data in image	Choose a location with unimpeded or minimally impeded view of sidewall

6.2.2.4 Temperature and Pressure Monitoring

Aside from displacement and strain, other practical tire information can be obtained from camera systems, such as temperature and pressure estimations. There is a known relationship between tire pressure, load, and deformation. For a given model of truck and tire, it could be possible to construct, empirically, a relationship between the tire pressure and deformation for an empty truck. Knowing this relationship, it could be possible to measure the deformation of a tire from images and estimate tire pressure, which is an important factor in extending tire life.

Tire pressure is also temperature dependent. Temperature measurements could be obtained by incorporating a camera with thermal imaging into the proposed monitoring systems. In addition to improving pressure estimation in tires, it is possible that thermal imaging could be used to detect localized tire damage that generates heat, such as friction from belt separation.

Thermal imaging was tested during a site visit, providing detailed measurements showing the differences in temperature in the tire. Figure 55 is an example collected at the rest stop, showing the highest temperatures around the body of the truck and the engine, even at rest. Although the outdoor temperature was below 0°, the tire surface was approximately 30°, and the rim 50°, highlighting the environmental stress on the tires.

FIGURE 55: THERMAL IMAGE OF TRUCK AT REST STOP

Thermal cameras could be implemented in a laboratory setting to examine heat generation in the tire at multiple speeds and under different loads. The effects of tire damage on heat generation could also be investigated in the laboratory with a thermal camera.

6.3 Summary

The objective of this work was to determine if an optical system using DIC could detect damage in tires. To test this hypothesis, an apparatus was commissioned to orient and load tires while digital cameras recorded images. A commercial software package was used to calculate displacement and strain measurements on the tire surface from calibrated digital images. Internal and external damage was investigated at multiple orientations under stationary and rotating loading conditions. Metrics were created to define visibility using the strain measurements in damaged areas. Damage visibility at different orientations was used to recommend procedures for potential field applications of this work.

Recommendations for future development of an industrial camera-based monitoring system were also determined from on-site observations as well as laboratory experience. The primary suggestions are to install cameras in a sheltered, bright location where trucks travel at a reduced, controlled speed. In addition to strain and displacement measurements for damage detection, other possible field applications of camera systems include temperature and pressure monitoring in tires.

Future laboratory work could address potential challenges with a field implementation of this inspection technique, such as the effects of dirt, dust, and other environmental factors on the visibility of the tire pattern, and its consequences. Furthermore, future work could address areas such as the sensitivity of the damage visibility to the severity and type of tire damage, as well as observe strain changes caused by more complex damage types such as fatigue. The camera and software system could also be used to measure properties of specific tires to analyze their performance, and integrate those properties with finite element (FE) models. These results could be used to improve understanding of damage mechanisms in tires and suggest improvements in tire design and construction.

The current work is a valuable step in moving from laboratory experiments to analyzing tires at an industrial site. Methods described in this work can be used to gather displacement and strain information from a tire, under both stationary and rotating loading conditions. It has been shown that it is possible to detect damage in a tire from image-based strain measurements. Metrics were defined to quantify damage visibility, and from this, recommendations were developed for processing data for industrial applications. Altogether, the procedures and techniques developed in this work can be used to gain a better understanding of changes in tire behaviour due to damage, and potentially extend tire life.

References

[1] Mukhopadhyay, A. (1989) "Selection, maintenance, and relations of various parameters for off-highway hauling tires". *Off-highway Haulage in Surface Mines*: 153-59

[2] Tupper, R. Personal communication. 6 Oct. 2011.

[3] Orlemann, E. C. (2000). *Building Giant Earthmovers* (pp. 12-19). Orescola, WI: MBI Publishing Company.

[4] Daws, J. W. (2003). Failure Analysis of Tire Tread Separations. *Practical Failure Analysis*, *3*(5), 73-80.

[5] Anzabi, R. Vaghar, D. S. Nobes, and M. G. Lipsett (2012). "Haul truck tire dynamics due to tire condition." *Journal of Physics: Conference Series*. Vol. 364. No. 1. IOP Publishing

[6] Sokolov, S. L., & Ushakov, B. N. (2009). Research Methods of Deformed-Stressed State for Rubber-Cord Machine Elements. *Vestn. Mashinostr.*, *5*, 29-33.

[7] Lipsett, M., Vaghar Anzabi, R., Kotchon, A., & Nobes, D. (2011). Condition monitoring for mining haul truck tires. *Proceedings of the Eighth International Conference on Condition Monitoring and Machinery Failure Prevention Technologies (CM 2011 and MFPT 2011)*, Cardiff, UK 20-22 June 2011, 12 pp.

[8] Chu, T. C., Ranson, W. F., & Sutton, M. A. (1985). Applications of digital-image-correlation techniques to experimental mechanics. *Experimental Mechanics*, *25*(3), 232-244. doi: 10.1007/BF02325092.

[9] Tailie, J., Goo, N.S., Woo,S.,& Park, H.C. (2009), Use of a Digital Image Correlation Technique for Measuring the Material Properties of Beetle Wing, *Journal of Bionic Engineering*, Volume 6, Issue 3, September 2009, Pages 224-231,

[10] Anzabi, R., Nobes, D.S., & Lipsett, M.G. (2012) Haul truck tire dynamics due to tire condition. *25th International Congress on Condition Monitoring and Diagnostic Engineering (COMADEM 2012*) 18–20 June 2012, Huddersfield, UK

[11] Clark, S. (1981) *Mechanics of Pneumatic Tires*. US Department of Transportation

[12] Kaliske, M. (2010). Numerical Modeling in Tire Mechanics. *LS-DYNA Forum, Bamburg*, 27-35.

[13] Braun, M. (1997) "Configurational Forces Induced by Finite-Element Discretization." *Proceedings of the Estonian Academy of Sciences, Physics and Mathematics* 46 Mar

[14] Rice, J. R. (1967) *A path independent integral and the approximate analysis of strain concentration by notches and cracks*. BROWN UNIV PROVIDENCE RI DIV OF ENGINEERING

[15] Serafinska, A., Wolfgang, G., & Kaliske, M. (2012) "A Multi-objective Optimization Approach with a View to Robustness Improvement."

[16] Sokolov, S. (2010). Prediction of Fatigue Life of Pneumatic Tires. *Journal of Machinery Manufacture and Reliability*, *39*(5), 459-465.

[17] Chevalier, L., Calloch, S., Hild, F., & Marco, Y. (2001), Digital image correlation used to analyze the multiaxial behavior of rubber-like materials*, European Journal of Mechanics* - A/Solids, Volume 20, Issue 2, March 2001, Pages 169-187, DOI: 10.1016/S0997-7538(00)01135-9.

[18] Moser, R., & Lightner, J. (2007). Using 3D Digital Image Correlation Techniques to Validate Tire FEM. *Experimental Techniques*, *31*(4), 29-36.

[19] Moser, R., Sube, J., Turner, J., & Zakelj, P. (2010) 3D Digital Image Correlation: Applications to Tire Testing. *Tire Science and Technology*, *38*(2), 100-118.

[20] Brossard, C., Monnier, J. C., Barricau, P., & Vandernoot, F. X. (2009) "Principles and Applications of Particle Image Velocimetry." *Optical Diagnostics of Flows* 1 Dec

[21] Cabrera, J. A., Ortiz, A., Simon, A., Garcia, F., & La Blanca, A. P. (2003). A versatile flat track tire testing machine. Vehicle System Dynamics, 40(4), 271-284.

[22] Castillo, J., De La Blanca, A., Cabrera, J., & Simon, A. (2006). An optical tire contact pressure test bench. *Vehicle System Dynamics*, *44*(3), 207-221.

[23] Giapponi, T. (2008). *Tire forensic investigation : analyzing tire failure*. SAE International.

[24] Vaghar Anzabi, R., Lipsett, M.G. (2011). Reliability analysis & condition monitoring methods for off-road haul truck tires, COMADEM 2011

[25] Lipsett, M., Vaghar Anzabi, R., Kotchon, A., and Nobes, D. (2011). Condition monitoring for mining haul truck tires. *Proceedings of the Eighth International Conference on Condition Monitoring and Machinery Failure Prevention Technologies (CM 2011 and MFPT 2011)*, Cardiff, UK 20-22 June 2011, 12 pp.

[26] Hiraoka, N., R. Matsuzaki, and A. Todoroki. (2009) "Concurrent monitoring of in-plane strain and out-of-plane displacement of tire using digital image correlation method." *Journal of Solid Mechanics and Materials Engineering* 3.11: 1148-1159.

[27] Matsuzaki, R., Hiraoka, N., Todoroki, A., & Mizutani, Y. (2010). Optical 3D Deformation Measurement Utilizing Non-planar Surface for the Development of an "Intelligent Tire". *Journal of Solid Mechanics and Materials Engineering*, 4(4), 520-532.

[28] Chow, C. L., & Woo, C. W. (1981) The Effect of Inflation Pressure and Vehicle Loading on the Sidewall of a Radial Tire. *Experimental Mechanics*, *21*, 379-385.

[29] Barson, C.W., and Gough, V. (1962) "Measurement of strain of materials of large extensibility" *Br. J. Appl. Phys.* 13 168

[30] Chen, P., Shubinsky, G., Jan, K., and Chen, C. (1993) Inspection of Tire Tread Defects Using Image Processing and Pattern Recognition Techniques. *SPIE Vol. 2063* pp. 14-21

[31] Wiseman, Y. (2010) "Take a picture of your tire!." *Vehicular Electronics and Safety (ICVES), 2010 IEEE International Conference on*. IEEE, 2010.

[32] Gros X. E. (1997), "Detection of delamination in tires using eddy currents." *Journal of Automotive Engineering*, Vol. 211, No. D1.

[33] Zhou, J., Hall, R. A., Fowler, G., & Huntingford, K. (2008). Evaluation of the effect of off-the-road tire air pressure setting on tire performance. International Journal of Mining, Reclamation and Environment, 22(3), 237-244. Lovejoy, C. "Getting a grip." *Mining Magazine* July 2012

[34] Carter, R. (2011) "OTR Tire Supply Comes Under Pressure." *Coal age* 116.9: 34-37

[35] Developments in Tyres for Quarrying." Otraco (1993) Web. 3 Sept. 2012. <http://www.otraco.com.au/en-AU/Technical_Papers.aspx>.

[36] Brothen, C., Lee, T. (2008) "An ounce of prevention." *Canadian Institute of Mining Magazine*, Vol.3 No. 1.

[37] Orrell, J.R. (2008) "Tire failure detection." US Patent Publ. 2008/0018441, Jan. 24, 2008.

[38] Dos Reyes, H., and Warmann, K. (1996) "Acousto-Ultrasonic Damage Evaluation of Steel-Belted Radial Tires." *Materials Science* 210: 671-78

[39] Hugo, D., Heyns, S. P., Thompson, R. J., & Visser, A. T. (2007). Condition-triggered maintenance for mine haul roads with reconstructed-vehicle response to haul road defects. Transportation Research Record: Journal of the Transportation Research Board, 1989(-1), 254-260.

[40] Meyer, A, and D Adams. (2012) "Damage Identification of Ground Vehicle Through Passive Probing of Suspension Damping." *Experimental Mechanics*. Web. 6 Sept. 2012.

[41] Lacoursiere, R. A., Nobes, D. S., Homeniuk, D. L., Carey, J. P., Badawi, H. H., & Major, P. W. (2010). Measurement of orthodontic bracket tie wing elastic and plastic deformation by arch wire torque expression utilizing an optical image correlation technique. Journal of dental biomechanics, 1(1).

[42] Sztefek P., Vanleene, M., Olsson, R., Collinson, R., Pitsillides, A., S., Shefelbine (2010), Using digital image correlation to determine bone surface strains during loading and after adaptation of the mouse tibia*, Journal of Biomechanics*, Volume 43, Issue 4, 3 March 2010, Pages 599-605, ISSN 0021-9290, DOI: 10.1016/j.jbiomech.2009.10.042.

[43] Orteu, J. (2009) "3-D computer vision in experimental mechanics." *Optics and Lasers in Engineering* 47.3.

[44] StrainMaster. Product Manual. LaVision GmbH 16 Mar. 2007: 107-30. Flowmaster

[45] Westerweel J (1993), “Digital particle image velocimetry – Theory and application”,Ph.D. Dissertation, Delft University Press, Delft.

[46] Keane, R. D., & Adrian, R. J. (1992). Theory of cross-correlation analysis of PIV images. *Applied Scientific Research*, 191-215.

[47] Ronneberger, O., M. Raffel, and J. Kompenhans. (1998) "Advanced Evaluation Algorithms for Standard and Dual Plane Particle Image Velocimetry." *Proceedings 9th International Symposium on Application of Laser Techniques to Fluid Mechanics*. Web. 18 Mar. 2011.

[48] Stanislas, M., K. Okamoto, and C. Kähler. (2003) "Main results of the first international PIV challenge." *Measurement Science and Technology* 14.10: R63.

[49] Stanislas, M., et al. (2005) "Main results of the second international PIV challenge." *Experiments in fluids* 39.2: 170-191.

[50] Stanislas, M., et al. (2008)"Main results of the third international PIV challenge." *Experiments in fluids* 45.1: 27-71.

[51] Hart, D. P. (1998). PIV Error Correction. *9th International Symposium on Applications of Laser Techniques to Fluid Mechanics*.

[52] Hartley, R., & Zisserman, A. (2010). *Multiple View Geometry* (2nd ed.).

[53] Wieneke, B. (2005). Stereo-PIV Using Self-Calibration on Particle Images. *Experiments in Fluids*, *39*, 267-280.

[54] Rhyne, T. B. (2005) "Development of a vertical stiffness relationship for belted radial tires." *Tire Science and Technology* 33.3:136-155.

[55] Clark, S. (1981) *Mechanics of Pneumatic Tires*. N.p.: US Department of Transportation

[56] Lawson, N., & Wu, J. (1997). Three-dimensional particle image velocimetry: experimental error analysis of a digital angular stereoscopic system. *Measurement Science and Technology*, *8*(12).

[57] "16.5 x 6.50-8 Trailer Tire Assembly." *Princess Auto*. N.p., n.d. Web. 6 Nov. 2012. <http://www.princessauto.com/pal/product/8227175/>.

Appendix A: Load Cell Calibration

An Instron testing machine was used to apply known loads to the load cell, and the response from the strain gauges, with fixed amplification values, was measured. The load cell was fully supported on one end, and the load applied to the other, in bending. The strain gauges were aligned to measure bending stress, and this alignment was also used in the laboratory. The results are given in Table A1 below.

TABLE A1: RESPONSE OF LOAD CELL TO APPLIED LOAD

Load (lbs)	Response (V)
0	-0.091
100	1.432
200	2.945
300	4.486
400	6.067
450	6.852

A linear regression was performed on the calibration data, yielding the equation:

$$L = 64.816V + 7.3458 \quad [A1]$$

Where L represents the bending load, in pounds, applied to the load cell, and V represents the output voltage from the strain gauges and conditioning unit.

Appendix B: Tire Deformation

Two photographs were used to represent the on-site condition of a tire ready for inspection. Figure B1, on the left, depicts the tire of an empty truck at a rest stop, while Figure B2 is a snapshot from a video of a truck heading to the crusher to unload ore.

FIGURE B1: HAULAGE TIRE AT REST STOP

FIGURE B2: HAULAGE TIRE AT CRUSHER DUMP

Several measurements were made from these images in an attempt to represent the deflection of the bottom of the tire due to the load. The end goal is to determine if the laboratory apparatus will be sufficient to replicate these conditions in experiment.

TABLE B10: GEOMETRIC TIRE MEASUREMENTS

Measurement (pixels)	Image 1	Image 2
Bottom Wall Height :	498	103
Top Wall Height :	582	122
Bottom Radius:	1104	232
Top Radius:	1185	250
Vertical Diameter:	2293	485
Horizontal Diameter:	n/a	500

From this table, it is possible to describe the deformation of the tire in multiple ways. For example, knowing that the majority of the visible deformation occurs in the rubber wall, as opposed to the hub, it is reasonable to describe the deformation of the tire as the percentage change in height of this section as it contacts the ground. In image 1, this deformation is (582-498)/582*100 = 14.4%, while it is 15.6% for the tire in image 2. By comparison, using 2 times the total radius of the upper portion of the tire as an estimate of undeformed diameter, the percentage change in diameter of the tire is only 3.3% and 3.6%, respectively. The change in the rubber section of the tire (14.4% and 15.6%) will be used as an indicator of deformation for experiments, and as a guideline in experimental design.

For similarity to site conditions, the experimental apparatus should be able to cause a 15% length change in rubber section of the laboratory tire. Using Rhyne's formula for tire stiffness:

$$K = 2.68\,P * (W * D)\text{^}0.5 + 33.1 \quad [B1]$$

D = 419 mm

W = 165 mm

P = 0.165 MPa

The calculated stiffness of the tire is *K* = 149 N/mm. Next, the formula *F = K*d* can be used to estimate the force required to cause the desired deformation in the tire. The displacement, *d*, in this case, is a change of 15% in length of the rubber tire sidewall from the outer tread to the outside edge of the hub, which in its unloaded state, measures 75 mm. Hence, the required force, *F*, is equal to 149 N/mm * 0.15 *75 mm = 1676 N, or 171 kg.

Appendix C: Uncertainty in Strain Values

The following procedure is taken from LaVision's StrainMaster D80 product manual.

The uncertainty in calculated strain is governed by two primary sources of error, error which results from the correlation process, and measurement error due to camera calibration. Since both of these errors are Gaussian, the following formula can be used to define the strain error, σ_ε:

$$\sigma_\varepsilon = \sqrt{\sigma_a^2 + \sigma_b^2}$$

EQUATION C1: SUM OF ERROR DUE TO CORRELATION PROCESS AND CAMERA CALIBRATION

where σ_a represents the correlation error, and σ_b represents the calibration error.

Depending on processing parameters such as window size and overlap, there is an uncertainty σ_v associated with each calculated displacement vector. Since strain is calculated from two neighbouring vectors, this multiplies the uncertainty by a factor of $\sqrt{2}$, leading to the expression:

$$\sigma_a = \sigma_{v1-v2} = \sqrt{2} \cdot \sigma_a$$

EQUATION C2: CORRELATION UNCERTAINTY IN STRAIN DERIVED FROM DISPLACEMENT VECTORS

Two neighbouring vectors differ by a factor of *E*g*, where *E* is the local strain in the given direction, and *g* is the grid spacing in the same direction. This results in the following equation for the relative strain error due to correlation:

$$\sigma_a = \frac{\sqrt{2} \cdot \sigma_a}{E \cdot g}$$

EQUATION C3: RELATIVE CORRELATION UNCERTAINTY IN STRAIN

Similarly, the relative error due to calibration error can be defined as the RMS calibration error, σ_c, in pixels, divided by the grid spacing, g_c, of the calibration target, in pixels.

$$\sigma_b = \frac{\sigma_v}{g_c}$$

EQUATION C2:RELATIVE CALIBRATION UNCERTAINTY

This results in a total relative error of:

$$\sigma_\varepsilon = \sqrt{\left(\frac{\sqrt{2}\cdot\sigma_a}{E\cdot g}\right)^2 + \left(\frac{\sigma_v}{g_c}\right)^2}$$

EQUATION C2: TOTAL COMBINED RELATIVE ERROR IN STRAIN

From the Strainmaster manual, the uncertainty in a displacement vector, *σv*, obtained from correlation, for a 32x32 window, with 50% overlap, as used in the experiments, is 0.05. The largest calibration error, *σb*, allowed during experiments was 0.17 pixels, for a calibration grid spacing of 129 pixels. Using these two values in equation (number), the obtained uncertainty, for 15% strain, is:

$$\sigma_\varepsilon = \sqrt{\left(\frac{\sqrt{2}\cdot 0.05}{0.15\cdot 16}\right)^2 + \left(\frac{0.17}{129}\right)^2} = 900\ \mu\mathrm{S}$$

EQUATION C2: COMBINED UNCERTAINTY IN SINGLE STRAIN VALUE

Finally, since average maximum and minimum principal strains are a derived quantity, this leads to an additional increase in uncertainty by a factor of 2. This results in an uncertainty for principal strains of 1800 μS.

For the visibility analysis, maximum and minimum principal strains were averaged over an area containing at least *N*=50 independent measurements. The error in the averaged quantity is 1/sqrt(*N*) times the value of the error in each individual vector. Hence, the error associated with the averaged maximum and minimum principal strains for this experiment is 1800 μS/sqrt(50) = 260 μS, or 0.26%.